Compact design of a planar compliant XY precision positioning stage

for automated malaria diagnosis using a microscope

Tim Feddes

Report no	: MSD 2020.061
Coach	: Ir. J.W. Spronck
Professor	: Prof. dr. ir. J. L. Herder
Specialisation	: Mechatronic System Design
Type of report	: Master of Science Thesis
Date	: 15 December 2020

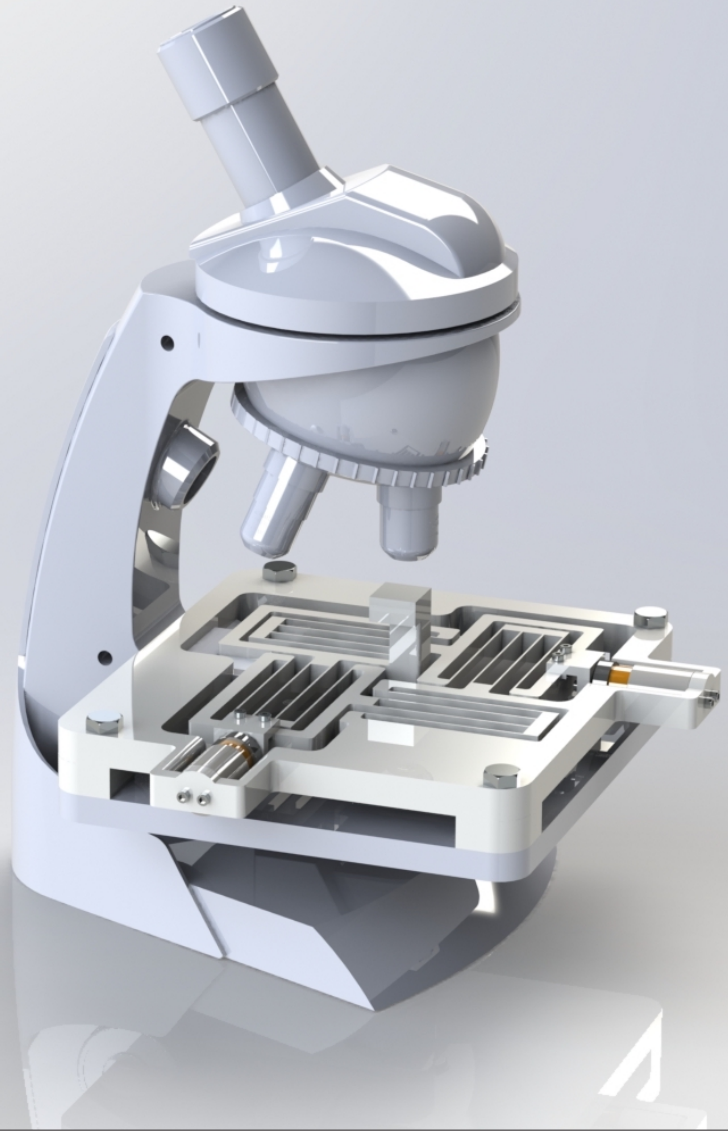

TU Delft Delft University of Technology

Challenge the future

Department of Precision and Microsystems Engineering

Compact design of a planar compliant XY precision positioning stage

for automated malaria diagnosis using a microscope

by

Tim Feddes

to obtain the degree of Master of Science
at the Delft University of Technology,
to be defended publicly on Tuesday December 15, 2020 at 13:30 PM.

Student number:	4450930	
Thesis committee:	Ir. J. W. Spronck,	TU Delft, supervisor
	Dr. A. Hunt,	TU Delft
	A. A. Dastjerdi, MSc.	TU Delft

TU Delft Delft University of Technology

Summary

Malaria remains a major burden on global health, with roughly 200 million reported cases worldwide and more than 400,000 deaths per year. According to the World Health Organization (WHO), ninety-three percent of all deaths due to the disease occurred in developing countries in sub-Saharan Africa. This large percentage is directly correlated to the lack of diagnostic tools in those developing countries. Early and accurate diagnosis of malaria is a critical aspect of efforts to control the disease. Thorough review of a well-prepared and well-stained peripheral blood smear by a skilled microscopist remains the clinical gold standard for malaria diagnosis. However, this microscopic examination is subjective and requires a highly experienced and skilled microscopist. Next to that, it is a labour-intensive procedure which is very time consuming. The blood smear should be scanned at sufficient resolution which is too large to be captured by a single image, thus creating the need to reposition the blood smear within the field of view of the microscope. The alternative of doing this manually is to use a planar positioning system that actively controls the position of the microscope stage such that the region of interest displayed can be changed allowing the entire blood smear to be scanned. This sequence of images can then be stitched together into one large image and diagnosed using a computer vision algorithm that detects and quantitates parasite-infected red blood cells. Automated hematology analyzers that are currently available are of high cost and therefore only suitable for laboratories and not for a local doctor's practice. The wish of this research is to provide the design of a compact and affordable positioning stage which can be used for automated malaria diagnosis in developing countries without the involvement of a laboratory. The conceptual system overview is shown in Figure 1.

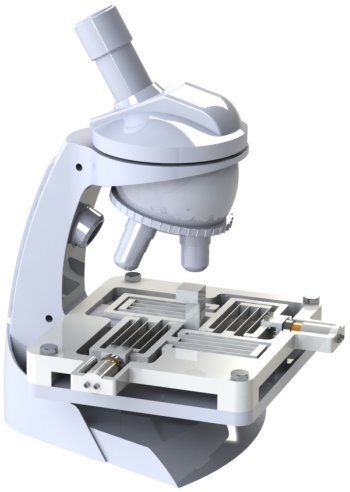

Figure 1: Conceptual system overview without power source, driver or laptop, merely to show how the positioning stage can be integrated into a microscope.

The objective of this study is to identify the design space of compliant XY precision positioning stages that can be used for automated malaria diagnosis using a microscope. The challenge imposed with this objective is that obtaining large deflections in flexure mechanisms can be hard to achieve due to the inherent imperfection of flexures and therefore the stage dimensions tend to become very large. Obtaining larger deflections in flexure mechanisms results in increased stresses that should not exceed the yield stress of the material to prevent permanent deformations. Larger deflections will also result in parasitic motion errors that are undesired since they decrease the positioning precision. Achieving large motion range ($\gg 1mm$) along with high motion quality ($< 10\mu m$) has been a key challenge in designing compliant positioning systems. The identified knowledge gap that has been researched is: how

to design a compact compliant XY precision positioning stage that can position precisely $(3\sigma < 10\mu m)$ within a workspace of $10mm$ by $10mm$.

In this research, the compact design of a planar compliant XY precision positioning stage with parallel kinematics, decoupled, and modular structure is presented. The design of the stage was a parallel process with various iterations between all different sub-systems, this is required to obtain a comprehensive system design where all sub-systems work in conformity. The stage mechanism is devised using flexural building blocks to achieve a decoupled and modular structure. In the early design phase, a Finite Element Analysis (FEA) using COMSOL was conducted to compare the performance of various flexural building blocks in terms of deformation stresses, parasitic rotation, and other parasitic motion errors. It is observed that the Double Parallelogram Flexure Module (DPFM) offers more suitable performance for the desired application. This building block is used as input, with the use of a constraint-based method, to come to the final mechanism design. Structural parameters of the DPFM were carefully designed to ensure that all requirements are met and that design challenges are overcome.

A demonstrator is 3D-printed out of Polylactic Acid (PLA) as proof of concept with the primary purpose of showcasing the performance. Therefore, the demonstrator that was built is an incomplete version of the conceivable product that can be used for automated malaria diagnosis. To reduce costs, this system will operate without an external feedback sensor. A compliant mechanism offers high repeatable motion due to the frictionless and backlash-free characteristics of flexure joints, which makes it possible to operate without position feedback from a sensor. However, due to the absence of position feedback of the motion stage, it necessitates an additional calibration step to determine the transformation matrix between the actuator input (voltage) and the motion stage output (displacement). Two voice coil actuators are used to control actuation in X- and Y-direction separately, while two laser triangulation sensors measure the corresponding displacements of the reference point, which is attached to the end effector of the positioning stage, to evaluate the performance and to conduct proper calibration. After calibration, the laser triangulation sensors can be removed from the system to yield a low-cost, standalone precision stage. The experimental setup is shown below in Figure 2.

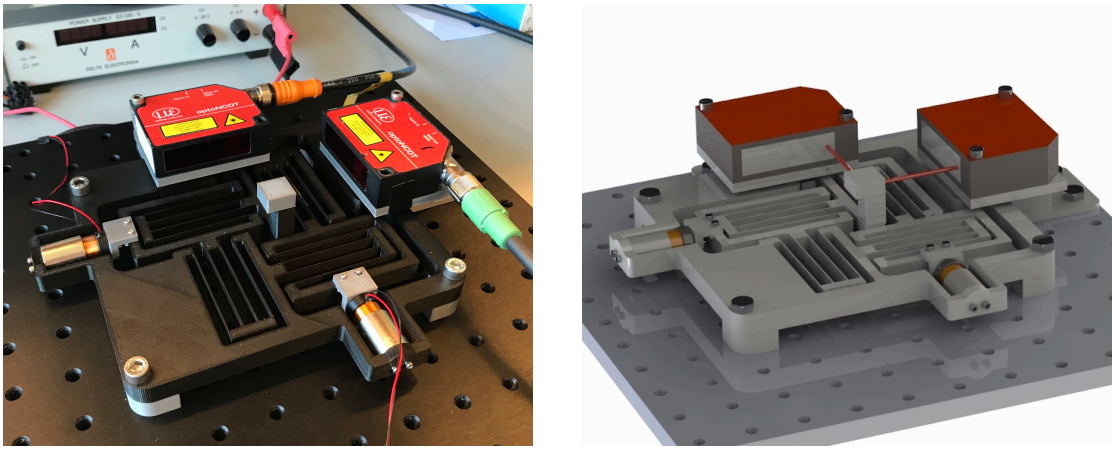

(a) (b)

Figure 2: **(a)** The experimental setup used for performance evaluation. **(b)** A CAD model of the experimental setup showing how the laser beams interact with the reference point.

The results show that a long-stroke compliant precision positioning stage was designed and built successfully. The demonstrator has shown to be simultaneously capable of positioning within a workspace of $10mm$ by $10mm$ while providing high precision motion. The performance is very consistent throughout this workspace and shows translational motion with high repeatability $(3\sigma \leq \pm 2.5\mu m)$ due to the highly reproducible behavior of flexures and due to a lack of friction and backlash. The out-of-plane deflection of the motion stage proved to be within $\pm 20\mu m$ which is well within the range of the autofocus.

System identification confirms that the demonstrator provides a reliable decoupled motion between the X- and Y-axes until a bandwidth of $60Hz$ meaning that the effects of cross-axis coupling are negligible, thus enabling fast and precise XY positioning.

Reflecting on the objective of this research, strategies to identify the design space of compliant positioning stages with long-stroke have been implemented successfully. This resulted in the compact design of a planar compliant XY precision positioning stage that can be used for automated malaria diagnosis using a microscope. The societal contribution of this research is to speed up the diagnosis of malaria in developing countries. The scanning procedure of the stage takes only 3.4 minutes, including time for the autofocus to stabilize and obtain sharp images this results in a total scanning time of approximately 17 minutes. This is faster than manual diagnosis $(60min)$ and comes close to the speed of a hematology analyzer $(2min)$ at a fraction of the cost. A standard hematology analyzer costs around $10.000\$$, while this system has a total cost of approximately $300\$$ including control hardware and excluding the cost of a laptop and microscope since it is assumed that those are already available in the local doctor's practice. The compliant stage itself can be 3D-printed for only $\approx 3.00\$$. The scientific contribution of this research lies in the design choices that were made which resulted in the design of a compact long-stroke compliant XY precision positioning stage with decoupled and modular structure. The design process can function as a guideline for others to design a compliant positioning stage. The performance evaluation with regard to this long-stroke compact design is compared to existing works by looking at an area ratio of workspace to planar dimension. It shows a higher ratio than almost all stages in literature and therefore it can be concluded that the scientific research gap has been investigated successfully.

In conclusion, the results obtained from FEA and experimental measurements are shown to be in good agreement with the analytical predictions for this stage. The demonstrator managed to achieve the set requirements for blood smear analysis. Therefore, it can be concluded that the stage was designed successfully and it can be implemented for automated malaria diagnosis to help Africa control the disease.

Preface

Here I am, writing the final words as a student at TU Delft before obtaining my Master's degree. After five years of studying in Delft, I feel more than ready to take on a new challenge and apply my knowledge in practice as a mechanical engineer. Over the past year, I was fortunate enough to be able to work on a project that I am deeply passionate about. Beforehand, I could not have imagined that so many different fields of engineering are involved in what looks like such a simple concept as positioning. I learned a lot during this year but one thing in particular: discipline is the bridge between goals and accomplishment. In a project like this, especially during these strange times where everyone works from home, discipline will help you to stay focused on reaching your goals. Of course, I did not achieve the results of this research all by myself. Therefore, I would like to express my gratitude to everyone who contributed directly or indirectly to this research.

First and foremost, I would like to express my gratitude to Jo Spronck for being the best supervisor I could have wished for. You provided me with guidance, endless positive energy, and the freedom to independently develop this research into my own project. I am extremely grateful for our interesting meetings and your support and interest in my academic and business endeavors. I would also like to thank Andres Hunt for his advice on the voice coil actuators I required for my project and for ordering them. I would like to thank Jos van Driel for his incredible assistance with LabView that enabled me to perform all the measurements I required. I would like to thank the technical support staff: Spiridon and Bradley for helping me with 3D-printing. Next to that, I would like to thank everyone for the interesting discussions during the Monday morning meetings. I would also like to thank Andres Hunt and Ali Ahmadi Dastjerdi from my exam committee for taking the time to review my thesis. Last but not least, I would like to thank my fellow students in particular: Mridul, Michiel, Melvin, Timothy, Rafael, Arnout, and Marcos for all the interesting discussions and for providing each other with feedback.

Tim Feddes
Delft, December 2020

Contents

1

Introduction

Malaria remains a major burden on global health, with roughly 200 million reported cases worldwide and more than 400,000 deaths per year [19]. According to the World Health Organization (WHO), ninety-three percent of all deaths due to the disease occurred in sub-Saharan Africa. This large percentage is directly correlated to the lack of diagnostic tools in developing countries. Figure 1.1 shows the distribution of malaria around the globe indicating that developing countries are affected the most. The diagnosis of malaria in developing countries is currently performed manually which is very time consuming and subjective. Early and accurate diagnosis of malaria is a critical aspect of efforts to control the disease.

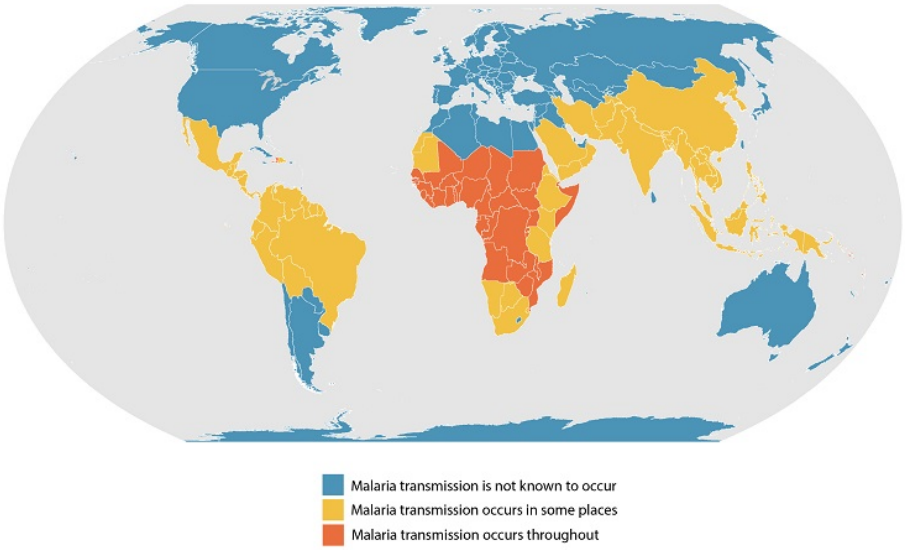

Figure 1.1: World map of malaria distribution [4].

1.1. Malaria diagnosis

Thorough review of a well-prepared and well-stained peripheral blood smear by a skilled microscopist remains the clinical gold standard for malaria diagnosis. However, this microscopic examination is subjective and requires a highly experienced and skilled microscopist. Next to that, it is a labour-intensive procedure which is very time consuming. In developing countries, there are simply not enough trained microscopists and there is not sufficient equipment available to perform this diagnosis. This creates the need to send blood samples all over the country to so called test laboratories. However, this is undesirable since this leads to slower test results.

The blood smear should be scanned at sufficient resolution which is too large to be captured by a single image, thus creating the need to reposition the blood smear within the field of view of the microscope. The alternative of doing this manually is to use a planar positioning system that actively controls the position of the microscope stage such that the region of interest displayed can be changed allowing the entire blood smear to be scanned. During scanning it is important that the blood smear stays within the autofocus range of the microscope such that only sharp images are obtained. This sequence of images can then be stitched together into one large image and diagnosed using a computer vision algorithm that detects and quantitates parasite-infected red blood cells.

The advantage of automating this process is that there will no longer be any manual work involved in the diagnosis except for preparing the blood smear on a glass slide and then placing and aligning it on the automated stage. This speeds up the diagnostic procedure and removes the need to send blood samples all over the country. When automated, more blood smears can be analyzed resulting in an earlier start of treatment and thus more effective treatment.

1.2. Literature study

There are various precision positioning stages available for microscopes that can achieve the requirements necessary for automated blood smear analysis. The problem with the available stages is that they are too expensive for use in developing countries. Appendix A shows an extensive literature study that was performed in order to classify state-of-the-art precision stages as found in literature and it divides them into different sub systems in order to propose the design of a XY precision positioning stage that is suitable for the application of blood smear analysis.

The results show that there is a knowledge gap in the area of compact long travel compliant precision positioning stages. If a flexure based compliant precision positioning stage could be designed that includes both compact size and the ability to reach long travel range, this would be a thorough improvement for not only the automation of blood smear analysis but also for the scientific community in general. Compliant stages are mainly used for nano-precision applications with small operating ranges. This method is not used yet for microscopy due to its short operating range (sub-micrometer).

1.3. Project objective

Given the current lack of large range ($\gg 1mm$) compliant XY precision positioning stages with compact design, an interesting research topic is to design such a compliant stage which can be used for the application of blood smear analysis to detect malaria. Therefore, the objective of this project is to design a compact long travel compliant XY precision positioning stage that can operate within a workspace of $10mm$ by $10mm$, which is sufficient for the analysis of a blood smear. This emerges as a promising yet challenging research topic.

1.4. Thesis overview

In Chapter 2, background information about blood smear analysis and the microscope will be given. This information will be used to develop a conceptual stage design which defines the requirements, specifications, and design goals of the stage as shown in Chapter 3. The procedure of how the detailed stage design is constructed is shown in Chapter 4. This includes explanation on the use of flexure modules, topology of the design, optimization methods through parametric design, use of symmetry, and validation through finite-element-analysis (FEA) in COMSOL. Chapter 5 describes the experimental setup that is used for performance evaluation. The results of this performance evaluation are shown in Chapter 6 and extensively discussed in Chapter 7. Finally, in Chapter 8 the conclusions are listed and Chapter 9 gives recommendations for future research or improvements. Multiple appendices are included for example regarding the prior literature study or a detailed specification sheet of the actuators and sensors that were used.

2

Microscopic analysis

To be able to design an automated positioning stage for the application of blood smear analysis, it is essential to first learn more about the examination process. This chapter will give some background information on why a microscopic examination is performed. It also includes boundary conditions with respect to the required workspace of the stage and the scanning path. The microscope that is used for this project will be evaluated on its autofocus system from which the maximum allowable deflection in out-of-plane direction of the stage can be derived.

2.1. Blood smear analysis

When a drop of blood is smeared on a microscope slide and analyzed using a microscope it is referred to as blood smear analysis. This type of analysis can detect diseases or abnormalities in the blood cells. To date, microscopic examination of blood smears is the easiest and most reliable test for malaria. These tests should be performed immediately since it is vital that health-care providers receive test results within hours in order to initiate treatment as soon as possible. The treatment that is needed depends on the species of malaria parasites that are present in the blood cells and the percentage of cells that are infected with malaria. In some clinical settings there will not be any high-quality equipment available to perform a microscopic examination and therefore there are other options such as Rapid Diagnostic Tests (RDT). A RDT is an alternate way of quickly establishing the diagnosis of malaria infection by detecting specific malaria antigens in a person's blood. The use of a RDT does not eliminate the need for microscopic examination since the RDT may not detect which common malaria species are present. Therefore, the results from a RDT should only be used as an indicator and a microscopic examination should always follow to confirm the results.

Blood smears are able to provide all of the vital pieces of information to the doctor to guide the initial treatment decisions that need to be made acutely. Preparation of a blood smear is done as following: first a blood specimen is collected from the patient and it is placed on a microscope slide. Then using the corner of another slide, the drop is spread in a circular pattern until it has a diameter of about 10 millimeters. The blood smear is depicted below in Figure 2.1.

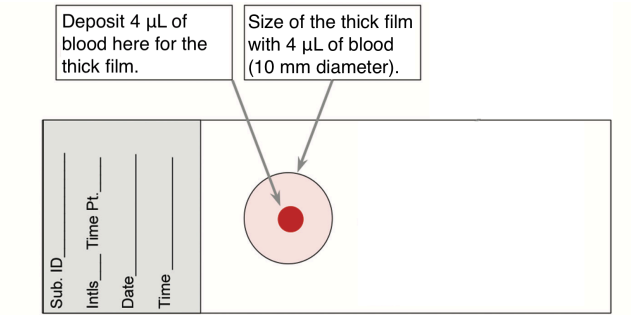

Figure 2.1: Thick blood smear with an outer diameter of 10 millimeter [16].

Prior to examination under the microscope, the specimen is stained (most often with the Giemsa stain) to give the parasites a distinctive appearance. The difference between healthy blood cells and parasite-infected blood cells becomes clearly visible as shown in Figure 2.2. On the left, an unstained blood smear is shown while the image on the right shows a blood smear which is stained using the Giemsa method where the appearance of parasite-infected blood cells is easy to distinguish. Examination is done with a $100X$ oil immersion objective combined with a $10X$ eyepiece resulting in $1000X$ magnification. A computer vision algorithm can be used to detect the presence of malaria and differentiate the various species by looking at visual criteria such as color and shape.

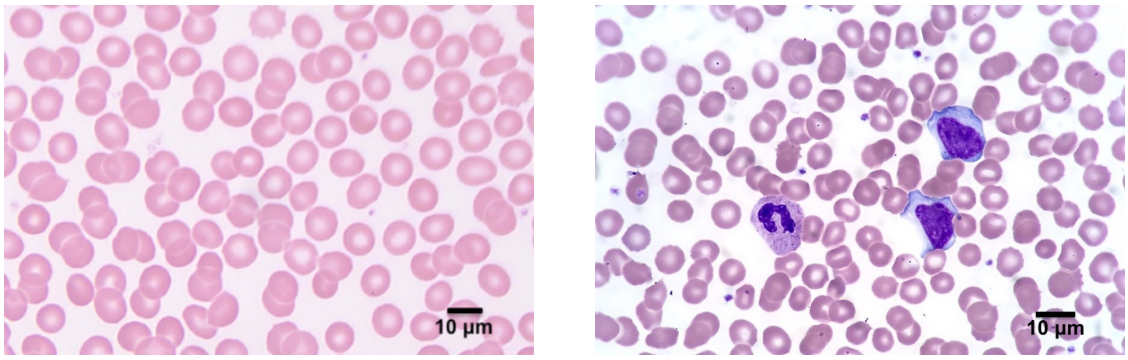

(a) (b)

Figure 2.2: **(a)** Unstained blood smear at 1000x magnification [24]. **(b)** Giemsa stained blood smear at 1000X magnification showing malaria parasites in purple [23].

2.2. Preferred scanning path

The stage can scan the entire blood smear while following multiple paths. During travelling of this path, multiple images, each with a unique field of view, can be acquainted which are stitched together into one large image. A computer vision algorithm can automatically detect the percentage of blood cells that are infected with malaria and it can identify which species are present.

A preferred path is one where only a single axis is actuated at a time and where the travelled path is kept at a minimum. This in order to achieve minimal cross-axis coupling and to decrease the total scanning time of the blood smear respectively. Cross-axis coupling refers to any motion along the Y-direction in response to an actuation along the X-direction, and vice versa. From these two conditions the following preferred path can be derived:

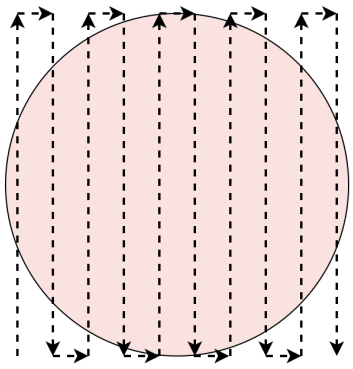

Figure 2.3: Preferred scanning path of the stage.

At $1000X$ magnification, the field of view of the microscope will have a diameter of 180 μm. This has an effective square field of view of 127 μm as shown in Figure 2.4. The square field of view is preferably used since it is easier to stitch square images together and it will also leave an overlap region which simplifies the stitching procedure. Therefore, step sizes of 127 μm will be taken and if this results in stitching errors due to a lack of overlap region at the corners of the field of view, this step size can easily be reduced to increase overlap region of consecutive fields of view. This means that a new image is generated every 127 μm. Whether this acquisition of images will be done with a continuous velocity or with a stop and scan method is to be determined later on. If the entire path is followed and a new image is established every 127 μm, this will result in a total of 6044 images that are needed to scan the entire blood smear. Notice that the scanning path is bigger than the blood smear itself, this is to ensure that the entire blood smear will still be scanned even though the alignment is poor or if the blood smear is not perfectly round.

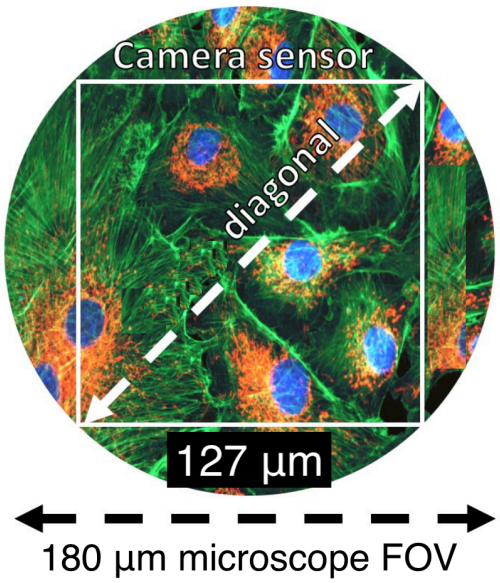

Figure 2.4: Field of view of the microscope at 1000X magnification [18].

2.3. Auto-calibration of the stage

Most of the precision positioning stages have feedback sensors to correct for disturbances in the system. To reduce costs, this stage will operate without an external feedback sensor. A compliant mechanism offers high repeatable motion due to the frictionless characteristics of flexure joints, which makes it possible to operate without position feedback from a sensor. However, due to the absence of position feedback of the end-effector of the motion stage, it necessitates an additional calibration step to determine the transformation matrix between the actuator input (voltage) and the motion stage output (displacement).

Therefore, the stage will be controlled using feedforward control which means that the control variable adjustment is not based on real-time position errors but rather on knowledge about the relation between the motion of the end-effector and the input of the actuators. This adjustment can either be based on a mathematical model of the stage or on measurements of the disturbances. Due to the highly reproducible behavior of flexure joints, this position error will re-occur at multiple consecutive measurements. This disturbance can then be compensated for by alternating the voltage in the voice coil motor in order to get the desired position of the end-effector and thus follow the preferred path precisely.

2.4. Autofocus

In digital microscopy, maintaining a sample in focus remains a challenge, especially at high magnifications. For the examination of test results it is essential to obtain sharp images from the scan. Acquisition of sharp images requires rapid and precise stabilization of the microscope focus. Therefore, an autofocus microscope is used which has a maximum range in axial direction of $\pm 100\mu m$ from its zero position to find the best focus value. The hardware autofocus system (NTSC/RS170 camera) used in this project can generate a new focus value within this range for every $16ms$ [6]. The maximum scan speed of the autofocus in axial direction is limited to $0.6\frac{mm}{s}$. This acquisition rate of focus values, along with the maximum scan speed, determines the axial resolution that can be obtained with this auto-focus system.

This information can be used to calculate the resolution of the autofocus range. However, there is a trade-off between high resolution and fast operation. Picking the maximum speed of the autofocus in axial direction that gives you the resolution you require and choosing a small travel range to scan in axial direction will result in the fastest operation. Therefore, the following steps are performed to calculate the stabilization time of the autofocus which can be translated to a required velocity of the stage actuation.

The first step is to determine the desired scanning range of the autofocus in axial direction to obtain the best focus value. A smaller range results in a faster scanning operation since less focus values have to be generated. Scanning of the range is shown in Figure 2.5. The scanning is performed by moving the controller down half the length of the travel range from the zero position, then scan up the full travel range, and return to the position that had the peak focus value. A sharp image can be taken at this peak focus value of which the position in axial direction will then become the new zero position of the scanning range. By having an adaptive autofocus scanning range, long scanning ranges can be avoided since only a small distance upwards and downwards from the previous focus value have to be scanned. This results in a faster scanning procedure.

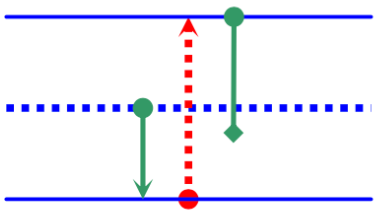

Figure 2.5: Shows how the autofocus range will be scanned. The green arrows just indicate a motion while the red arrow indicates a motion while scanning. The zero position is shown as a dashed blue line [6].

The full scanning range in axial direction is set to $\pm 3\mu m$ from the zero position. This means that for every new field of view of the microscope, the best focus value within a range of $\pm 3\mu m$ from the previous best focus value will be found. The desired resolution is set to $1\mu m/frame$ which is approximately the depth of field of a microscope at 1000x magnification. The total scanning distance will then be $6\mu m$ for which a total of 7 focus values have to be generated. Once the focus value is at its peak, the autofocus is considered to be stabilized and a sharp image can be obtained.

The stabilization time of the autofocus for each new field of view can be calculated as following: With an axial speed of $0.6\frac{mm}{s}$, it takes $5ms$ to move down from the zero position to reach the lower limit of the scanning range. Then it takes $10ms$ to move up the entire range and while doing so the controller has to stop 7 times to generate a focus value which takes a total of $112ms$. Then the controller has arrived at the top of the scanning range and it has to return to the highest focus value which takes a maximum of $10ms$. This adds up to a total stabilization time of $137ms$ per unique field of view to establish a sharp image.

3

Conceptual stage design

To design this positioning stage, requirements are formulated for the application of blood smear analysis. These requirements can be translated to specifications of the stage. Next to that, the stage should suffice some other design goals which allow the stage to be fabricated within the Precision and Microsystems Engineering Department of TU Delft. All of the previous determined information is used to define a conceptual system overview and some challenges that have to be overcome during this project are listed.

3.1. Requirements

The goal of this thesis is to design and build a demonstrator of a planar compliant XY precision positioning stage that can be used for the application of blood smear analysis. The stage has to be able to scan the entire blood smear while following a defined path. During this scanning the stage has to stay within autofocus range of the microscope such that only sharp images are obtained.

In order to scan the entire blood smear there have to be two degrees of freedom of the stage which are in X- and Y-direction. In both directions a translational displacement of 10 mm should be achieved. A three-sigma positioning repeatability of 10 μm at most is desired for proper calibration of the system. To ensure rapid stabilization after moving to a new field of view of the microscope, a settling time of 0.1 seconds is desired to stabilize within a 5% settling band. A deflection in the out-of-plane direction of $\pm$100 μm is allowed in order to stay within the autofocus range of the microscope. However, a smaller deflection is desired because this requires a smaller scanning range of the autofocus which results in a faster scanning time. The design requirements are shown in Table 3.1.

Requirements	
Degrees of freedom	2 (X and Y)
Range	10 mm x 10 mm
Repeatability (3σ)	$\leq$ 10 μm
Settling time	$\leq$ 0.1 s (127 μm step)
Out-of-plane deflection	$\leq \pm$100 μm

Table 3.1: General stage requirements

3.2. Specifications

The current automated systems for analyzing blood smears are very expensive and big such as the hematology analyzer. This makes them only suitable for laboratories and not for a doctor's practice. There are not as much laboratories and trained microscopists in developing countries as there are in wealthy countries. Initiating treatment as soon as possible is desired to have the most effective treatment for malaria. Therefore, there is no time to send the microscope slides to a test lab all over the country and having to wait multiple days for the results.

The aim of this thesis is to provide the design of a compact and affordable precision stage which can be used for automated blood smear analysis in developing countries without the involvement of a laboratory. Therefore, the stage has to be of low cost such that it is affordable for local doctors. Next to that, a compact design is required such that the stage can easily be integrated into a microscope platform. Also, the stage should have a robust design that is resistant to falling damage and can be used outside of clean room environments.

3.3. Design goals

During the design of the demonstrator positioning stage two design goals are constantly taken into account:

- **Manufacturability:** The entire stage must be able to be manufactured within one month, preferably in-house. This enables quick iterations between design and production.
- **Design for assembly (DFA):** This method seeks to simplify the stage by using a low number of parts which reduces the labour and time involved in assembly and decreases cost of the stage. Applications of DFA principles to stage design usually result in improved quality and reliability [13].

3.4. Conceptual system overview

A conceptual overview of the system is shown in Figure 3.1, which does not include the hardware required for actuation, control and image processing. This thesis will only focus on the design and building of a demonstrator of the precision stage as proof of concept with the primary purpose of showcasing the possible applications. Therefore, the demonstrator that is to be built is an incomplete version of the conceivable product that can be used for the application of automated blood smear analysis. This thesis does not focus on the integration into the microscope and the corresponding computer vision algorithm for the detection of malaria parasites.

The proposed demonstrator includes a planar compliant XY precision positioning stage with monolithic structure that allows precise guided linear motion of the end-effector by transmitting force from an actuator. Two ground-mounted voice coil actuators are used to control the actuation in X- and Y-direction separately. The blood specimen can be placed on top of the end-effector of the motion stage such that it is within the field of view of the microscope. Feedforward control can then be used to control the actuation of the system and thus scan the entire blood smear.

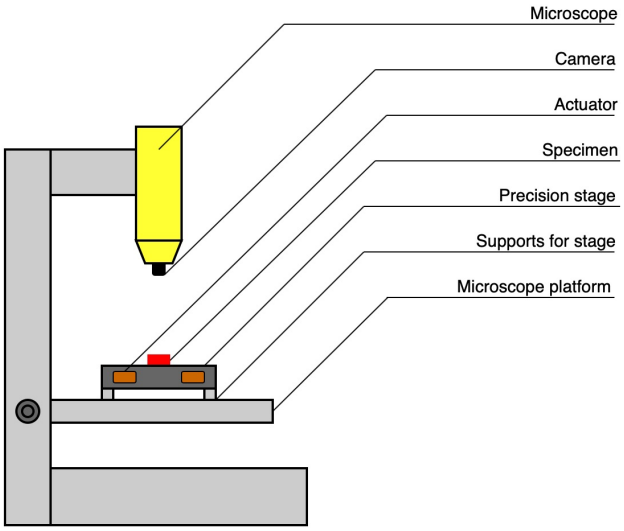

Figure 3.1: Conceptual system overview showing how the positioning stage can be integrated into a microscope.

3.5. Design challenges

There are several challenges that come into play while designing a positioning stage that meets all the previous mentioned requirements. The following challenges were identified and will be kept in mind during the design phase.

A. Large motion range while minimizing internal stresses

The design has the aim to achieve a large range of motion along the X- and Y-direction in order to obtain a workspace that is sufficient for the analysis of a blood smear. This poses a problem since there is a maximum allowable stress until material failure such as plastic deformation occurs. To prevent this from happening it is desired to have high compliance in the directions of motion such that the maximum stress level of the material is not reached while achieving the desired range of motion. However, maintaining high compliance in in-plane direction contradicts with the requirement of minimizing out-of-plane deflections. This is a trade-off that has to be considered during the design phase.

B. Avoiding yaw rotation

Another challenge is that during scanning of the workspace there will be yaw rotation of the motion stage which is considered to be a parasitic rotation [2]. This parasitic rotation reaches a maximum when the motion stage approaches the boundaries of the workspace. It is desired to minimize this parasitic rotation by inherently constraining this motion. This motion can be minimized with the use of parametric design and it can be constrained with the use of symmetric design which cancels out the parasitic rotation. However, using symmetric design would most likely increase the total size of the stage which would result in a trade-off between the allowable parasitic rotation and the compactness requirement of the stage.

C. Minimal cross-axis coupling

In compliant XY mechanisms it remains a challenge to achieve minimal cross-axis coupling between the actuation in X- and Y-directions. This means that there should not be any motion along the X-direction due to an actuation in the Y-direction or the other way around. To prevent this from happening it is necessary to sufficiently decouple the motion axes in X- and Y-direction which can be done with the use of a constraint-based method [1]. If there still remains significant cross-axis coupling which has a negative effect on the motion precision of the stage, this unwanted motion can be compensated for with the use of feed forward control. This is only the case if the stage has a high repeatability. Therefore, the stage should be evaluated on its repeatability.

D. Dealing with heat from the actuators

There are also challenges that have to be taken into account concerning the actuators. First of all, the voice coil motor is going to produce a lot of heat due to Joule heating that will transfer to colder objects that it is attached to through heat dissipation. Therefore, to maintain a high precision motion of the stage it is desired to have low thermal sensitivity or to have heat dissipation occur through the ground such that it will not affect the flexure mechanism. This can be done by mounting the actuators on the ground and only having a contact point between the flexure mechanism and the end-effector of the actuator.

E. Actuator mounting and alignment

It is also important to mount the actuators in such a way that there will not be any transverse loads and displacements on the end-effector of the actuator. This could drastically decrease the performance of the stage since the actuator is not built to tolerate transverse loads. Therefore, the point of actuation on the flexure mechanism should only move along the direction of actuation and should not be affected by actuation in a transverse direction. The elimination of transverse motion at the point of actuation is referred to as actuator isolation and can be very difficult to achieve due to parasitic rotation. One solution could be to include a decoupler between the actuation point on the flexure mechanism and the end-effector of the actuator. This is not desired because this would result in more motion freedom and less stiffness in transverse direction. This leads to a lower precision and it affects the dynamic performance of the motion stage due to a change in stiffness.

4

Detailed stage design

In this chapter, the compact design of a planar compliant XY precision positioning stage with parallel-kinematics, decoupled, and modular structure is presented. The design of the stage was a parallel process with various iterations between all the different sub-systems, this is required to obtain a comprehensive system design where all sub-systems work in conformity. For readability, the design is presented per sub-system. The detailed design process includes: the analysis of different flexural building blocks, an assembly of multiple building blocks resulting in a mechanism design, suitable material and manufacturing choices, optimization of this mechanism design in order to increase its performance, actuator selection and integration. This chapter will be concluded with an overview of the final design, bulk cost estimations for mass production and last but not least, an evaluation of the compactness ratio.

4.1. Flexural building blocks

Three different flexural building blocks were designed and will be evaluated on their performance. Evaluation is done using analytical analysis and through finite element analysis in COMSOL. These two methods work complementary to validate the performance of the building blocks.

For the design of the building blocks, the handbook of compliant mechanisms by Larry Howell will be used. This handbook states that devices with intermediate deflections, which are in the range of 10% of the flexure beam length, are considered ideal for precision devices and are common in positioning and measurement systems [5]. To obtain a desired travel range of $10mm$ in X-direction, a stroke in positive and negative X-direction of $5mm$ is required. Of course, these building blocks can also be used for the displacement in Y-direction. Following the advice given in the handbook, a flexure beam length of $50mm$ is required to obtain a deflection of $5mm$ while remaining within the intermediate deflection range.

For now this flexure beam length will be chosen and used to compare different building blocks to determine the most suitable building block for this application. Later on, this parameter can be optimized in the detailed design using finite element analysis. The building blocks will be evaluated on their maximum stress, parasitic displacement, and parasitic rotation while achieving the maximum required range of motion of $\pm 5mm$. Evaluation of the building blocks is done with Polylactic Acid (PLA) as the flexure material. This was chosen because of its ease of manufacturability and because it has good material properties for a compliant mechanism. The best material and manufacturing method can only be chosen once a concept is generated and therefore this choice will be re-evaluated once a concept is generated. All of the building blocks are modelled with an in-plane flexure thickness of $0.7mm$, which is a value at which 3D-printed PLA flexures using a Prusa printer are of the highest quality. The out-of-plane flexure thickness is chosen to be $10mm$ for all building blocks. This value can also be optimized in a later phase after a concept is generated.

4.1.1. Simple beam flexure module

The first flexure module that is analyzed is a simple beam flexure. Extensive research has already been done into the deformation of a beam flexure that is subject to a load (F) as shown in Figure 4.1.

From this research it is known that there is a deflection of beam tip (δ) in the direction of force. Also the tip rotates with an angle (θ) which is an undesired rotation and therefore a parasitic rotation. The end-effector will also move in X-direction which is called a parasitic motion (ϵ) because this motion is not desired.

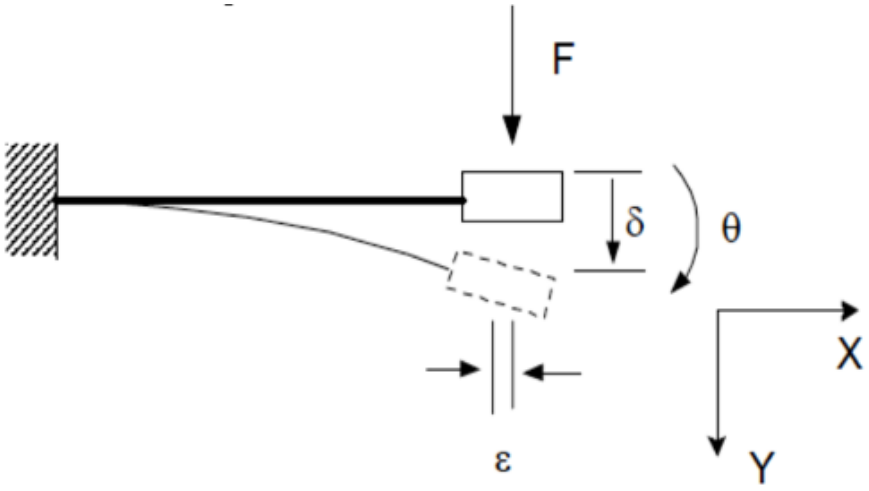

Figure 4.1: Deformation of a simple beam flexure module after applying a load (*F*) [2].

The deflection, parasitic rotation, and parasitic motion as shown in Figure 4.1 can be calculated using the following formulae respectively [17]:

$$\delta = \frac{FL^3}{3EI} \qquad \theta \approx \frac{FL^2}{2EI} \qquad \epsilon \approx \frac{\delta^2}{L} \tag{4.1}$$

For the deflection, a value of $5mm$ is chosen which can be used to make an approximate estimation of the required force to obtain this deflection. The following values were found:

$$F = 0.12N \qquad \theta = 8.59° \qquad \epsilon = 5 \cdot 10^{-4}m \tag{4.2}$$

The simple flexure beam is modelled in SolidWorks and then analyzed using COMSOL. The left block is fixed and a load of 0.12 Newton is applied in negative Z-direction on the mover block. The deformation and its corresponding maximum stress can be seen in Figure 4.2.

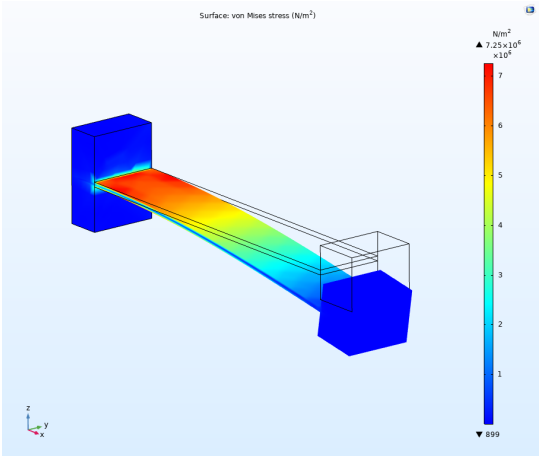

Figure 4.2: Analysis of a simple beam flexure module.

Using point evaluation in COMSOL a deflection of $5.38mm$ in negative Z-direction is measured with a corresponding parasitic rotation of $9.65°$. The parasitic motion in X-direction is $5.87 \cdot 10^{-5}$ m. The corresponding stress in the material reaches a maximum of 7.25 MPa which is below the yield stress of the material ($\sigma_y = 26MPa$ [21]). This means that deformation will stay within the elastic domain and the material will go back to its initial state once the load is released. The building block can therefore be used for the application but will result in large parasitic rotation and motion errors.

4.1.2. Parallelogram flexure module

The second flexure module that is analyzed is a parallelogram flexure. From earlier research it is known that when this flexure is subjected to a load (F) as shown in Figure 4.3, the beam tip will have a deflection (δ) in positive Y-direction. The tip will also rotate with an angle (θ) which is considered a parasitic rotation. Next to that, the end-effector will move in the X-direction which is an undesired motion and therefore referred to as a parasitic motion (ϵ).

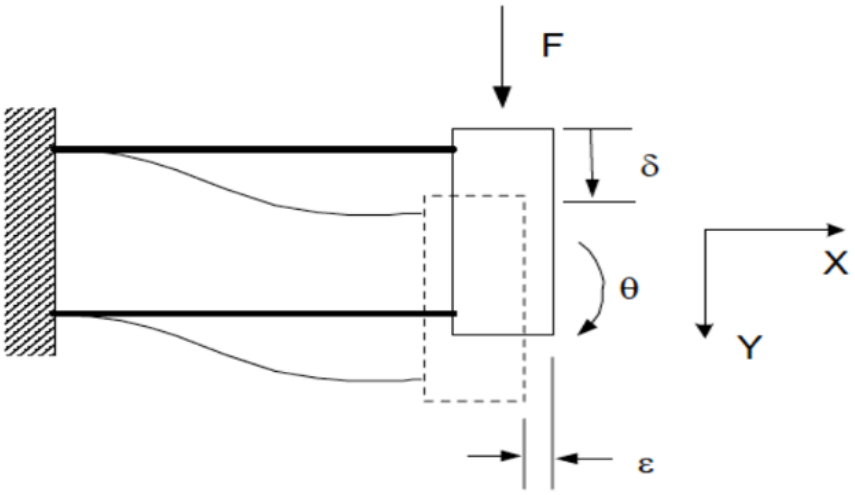

Figure 4.3: Deformation of a parallelogram flexure module after applying a load (*F*) [2].

The deflection, parasitic rotation, and parasitic motion as shown in Figure 4.3 can be calculated using the following formulae respectively [17]:

$$\delta = \frac{FL^3}{24EI} \qquad \theta \approx 2\left(\frac{h}{b}\right)^2 \frac{\delta}{L} \qquad \epsilon \approx \frac{3\delta^2}{5L} \tag{4.3}$$

For the deflection, a value of $5mm$ is taken which can be used to make an approximate estimation of the required force to obtain this deflection. The following values were found:

$$F = 0.96N \qquad \theta = 0.056° \qquad \epsilon = 3 \cdot 10^{-4}m \tag{4.4}$$

The parallelogram flexure module is modelled in SolidWorks and then analyzed through COMSOL. The left block is fixed and a load of 0.96 Newton is applied in negative Z-direction on the mover block. The deformation and its corresponding maximum stress can be seen in Figure 4.4.

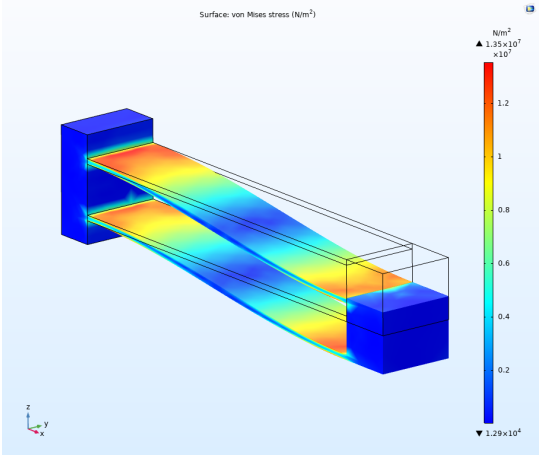

Figure 4.4: Analysis of a parallelogram flexure module.

Using point evaluation in COMSOL a deflection of $4.84mm$ in negative Z-direction is measured with a corresponding parasitic rotation of $0.123°$. The parasitic motion in X-direction is $8.75 \cdot 10^{-6}$ m. The corresponding stress in the material reaches a maximum of 13.5 MPa which is below the yield stress of the material. This means that deformation will stay within the elastic domain and the material will go back to its initial state once the load is released. The building block can therefore be used for the application. It has a significant smaller parasitic- rotation and motion error than the simple flexure beam.

4.1.3. Double parallelogram flexure module

The final flexure module that is analyzed is a double parallelogram flexure. This module has also been extensively researched in the past and therefore it is known that when the mover block is subjected to a load (F) as shown in Figure 4.5, the beam tip will have a deflection (δ) in positive Y-direction. The tip will also rotate with an angle (θ) which is considered a parasitic rotation. Next to that, the end-effector will move in the X-direction which is an undesired motion and therefore referred to as a parasitic motion (ϵ).

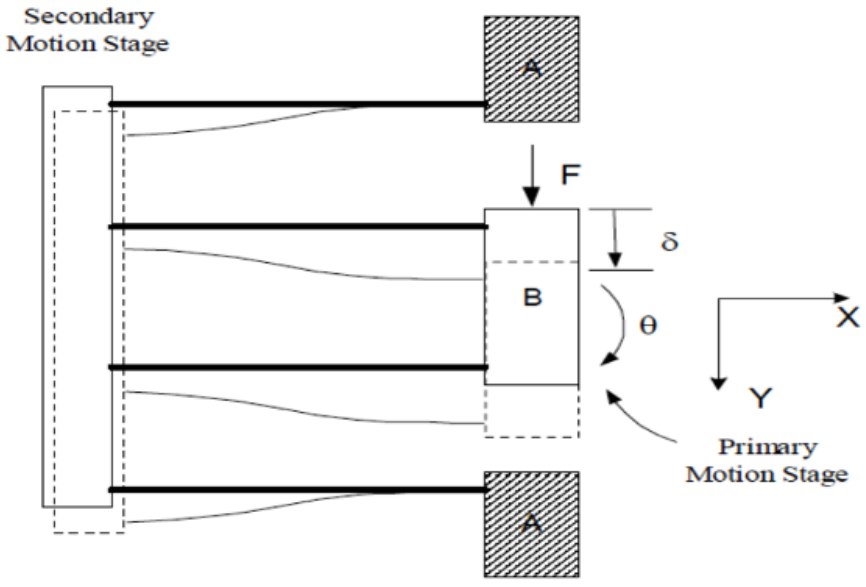

Figure 4.5: Deformation of a double parallelogram flexure module after applying a load (*F*) [2].

The deflection, parasitic rotation, and parasitic motion as shown in Figure 4.5 can be calculated using the following formulae respectively [17]:

$$\delta = \frac{FL^3}{12EI} \qquad \theta \approx t^2\left(\frac{1}{2b^2}\right)\frac{\delta}{L} \qquad \epsilon \approx 0 \tag{4.5}$$

For the deflection, a value of $5mm$ is chosen which can be used to make an approximate estimation of the required force to obtain this deflection. The following values were found:

$$F = 0.48N \qquad \theta = 0.014° \qquad \epsilon \approx 0m \tag{4.6}$$

The double parallelogram flexure module is modelled in SolidWorks and then analyzed through COMSOL. The two outer blocks on the right side are fixed and a load of 0.48 Newton is applied in negative Z-direction on the middle mover block on the right. The deformation and its corresponding maximum stress can be seen in Figure 4.6.

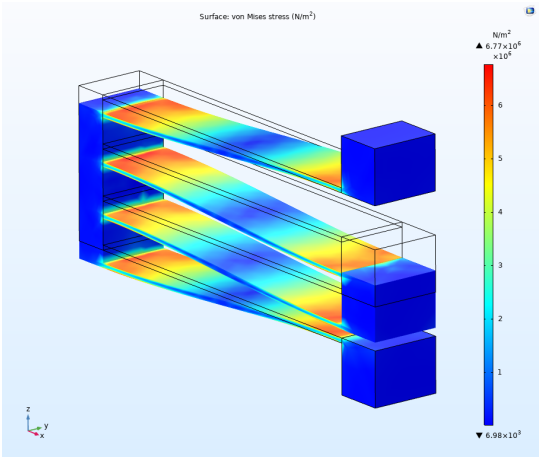

Figure 4.6: Analysis of a double parallelogram flexure module.

Using point evaluation in COMSOL a deflection of $4.84mm$ in negative Z-direction is measured with a corresponding parasitic rotation of $0.00054°$. The parasitic motion in X-direction is $5.48 \cdot 10^{-6}$ m. The corresponding stress in the material reaches a maximum of 6.77 MPa which is below the yield stress of the material. This means that deformation will stay within the elastic domain and the material will go back to its initial state once the load is released. The building block can therefore be used for the application. It has an even smaller parasitic- rotation and motion error than the parallelogram flexure module.

4.1.4. Comparison of these flexure modules

The three building blocks have been evaluated on their motion performance. The primary objective of the building blocks is to provide guided linear motion along one axis and constrain all other degrees of freedom. This means that parasitic rotation and parasitic motion errors should be as small as possible. During this motion it is essential that the stress in the material does not exceed the yield stress of the material such that the deformations remain within the elastic domain. In Figure 4.7 the three building blocks and corresponding deformations can be seen.

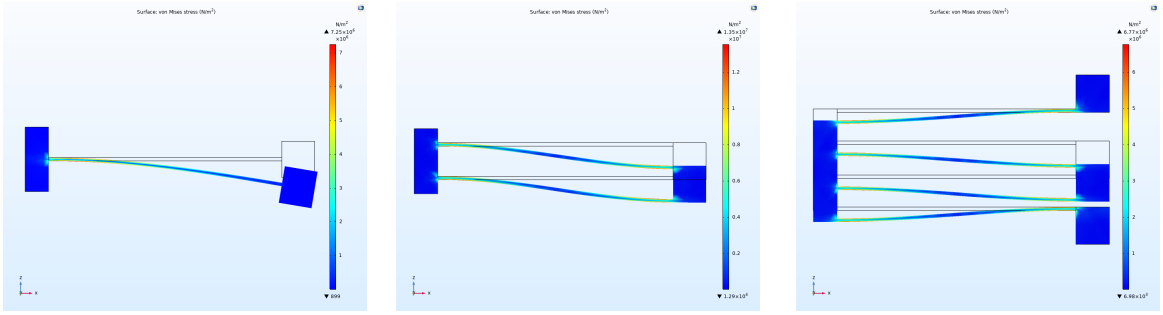

(a) (b) (c)

Figure 4.7: Analyses of the different flexure modules used for comparison.

The results from the analytical calculations and finite element analysis are compared to decide which building block should be used for the XY mechanism that is to be designed. In Table 4.1 the results with respect to stress levels, parasitic rotation, and parasitic motion are shown for a flexure length of $50mm$, width of $0.7mm$, and out-of-plane material thickness of $10mm$.

	von Mises stress σ in $[MPa]$	**Parasitic rotation** θ in $[°]$	**Parasitic motion** ϵ in $[\mu m]$
Simple beam flexure	7.25	9.65	58.7
Parallelogram flexure	13.5	$5.60 \cdot 10^{-2}$	8.75
Double parallelogram flexure	6.77	$5.40 \cdot 10^{-4}$	5.48

Table 4.1: Comparison of the results of different building blocks.

It is observed that the double parallelogram flexure module gives minimum parasitic error and negligible angular rotation as compared to the other two flexure modules and thus can be successfully used to form a XY mechanism.

Enhanced performance of the double parallelogram flexure module can be achieved through exploitation of the center of stiffness of the flexure module. If the force that acts on the flexure module has a point of application such that the center of stiffness is subjected to lateral loading, only a translational displacement can be expected. Therefore, actuation forces applied in the middle of the flexures (center of stiffness) result in the smallest coupling between the two motion axes and thus parasitic rotation of the flexure module will be minimized.

4.2. Mechanism design

The primary objective of the design is to achieve large travel ranges of the motion stage along the X- and Y-direction and constrain all other degrees of freedom (DOF). In order to achieve this it is necessary to have high compliance in the directions of motion such that the maximum stress stays below the yield stress while obtaining the desired travel range. It is also necessary to maintain high stiffness in the degrees of constraint (DOC) and allow only small parasitic errors such that the stage will have a high precision. To achieve this, the mechanism is designed such that the yaw rotation of the motion stage, which is a parasitic rotation, is inherently constrained. The flexure modules as described before can be used as building blocks to produce a two DOF planar mechanism. The topology of the mechanism has to sufficiently decouple the motion axes in X- and Y-direction such that there is minimal cross-axis coupling. This can be done using the constraint-based method shown in Figure 4.8.

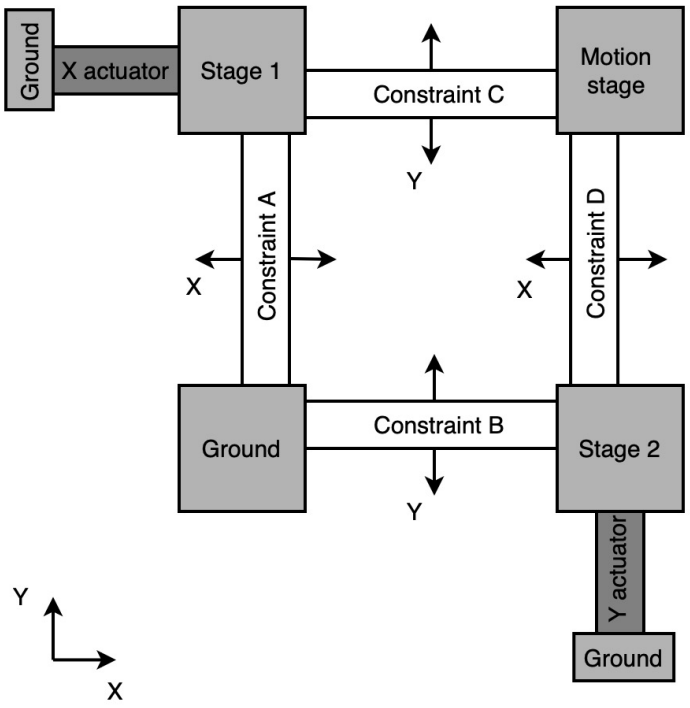

Figure 4.8: Constraint-based method that is used to create the mechanism design [1].

The topology shown in the constraint-based method [1] is designed to minimize cross-axis coupling and parasitic rotation of the motion stage. The topology exists out of four basic rigid stages: Ground, intermediate Stages 1 and 2, and the Motion Stage. Each rigid stage is connected to its adjacent stages by means of flexure modules. Stage 1 is connected to ground via flexure module A, which only allows relative X-translation between the two. The Motion Stage is connected to Stage 1 via flexure module C, which only allows relative Y-translation. The Motion Stage is also connected to Stage 2 by means of flexure module D, which only allows relative X-translation. Stage 2 is then connected to Ground via flexure module B, which only allows relative Y-translation.

Thus, Stage 1 will always have only an X-displacement relative to the Ground while Stage 2 will only have a Y-displacement. The Motion Stage is connected with Stages 1 and 2 through flexure modules C and D respectively which means that it will inherit the X-displacement of Stage 1 and the Y-displacement of Stage 2. This results in two degrees of freedom of the Motion Stage while intermediate Stage 1 will not have any motion along the Y-direction due to an actuation of Stage 2, and also intermediate Stage 2 will not have any motion along the X-direction due to an actuation of Stage 1. Therefore, the motion axes are sufficiently decoupled and minimal cross-axis coupling is obtained. Since the X- and Y-displacements of the Motion Stage do not result in displacement of Stage 2 and Stage 1 respectively, these intermediate stages will only have one degree of freedom which is in the direction of actuation

and are therefore ideal locations to apply the actuation loads such that there is actuator isolation.

The flexure modules shown in Figure 4.8 are replaced with the double parallelogram flexure module as described in the previous chapter. The double parallelogram flexure module offers large range, good rotational stiffness, and no purely kinematic parasitic errors. This results in the following mechanism design:

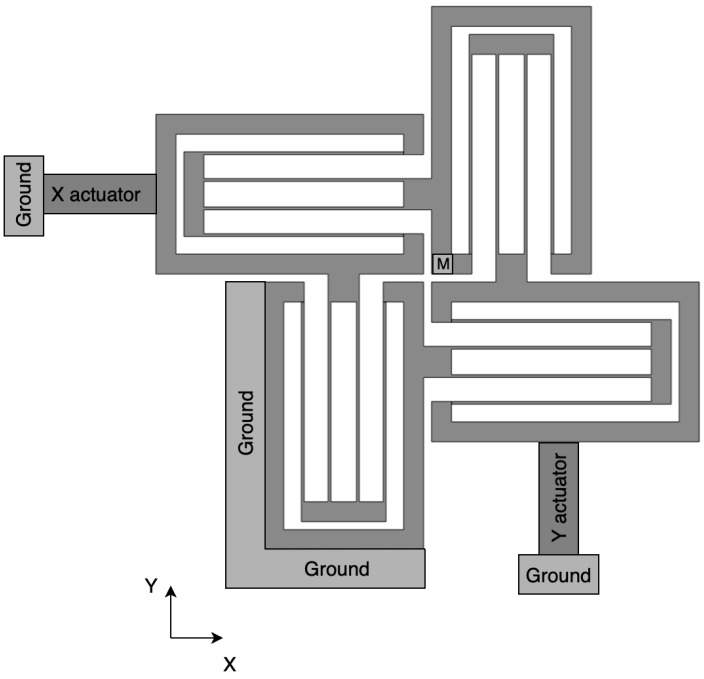

Figure 4.9: A mechanism design where M indicates the end-effector of the motion stage.

In an ideal scenario where the double parallelogram flexure modules behave as perfect constraints, this topology would yield a flawless design. However, due to the inherent imperfection in flexures, the actual resulting design is expected to deviate slightly from ideal behaviour. This deviation will occur through both, parasitic rotation and parasitic motion of the motion stage. This parasitic behaviour can be minimized by optimizing the dimensions of the double parallelogram flexure modules and by using symmetry to cancel out parasitic errors.

4.3. Material and manufacturing

The manufacturing method and material choice of the mechanism can be finalized now that a concept of the mechanism design was chosen. For the design of this demonstrator there was looked into four different manufacturing methods which will be described below.

- **Wire EDM:** The design can easily be fabricated out of aluminum using wire electrical discharge machining (EDM) which will result in a high performance demonstrator. However, this will be very expensive and since the demonstrator is only made as proof of concept this might not be the best option. A cost indication of this would be around 600 euros.
- **Milling:** The design can be fabricated using a milling machine. This would involve a lot of manual labor which is not desired for an efficient and accurate manufacturing process.
- **Laser cutting:** The design can be laser cut out of a thin sheet of material. This would be an inexpensive design method that does not involve a lot of manual labor. The downside of laser

cutting is that this method is still not capable of cutting thick metals which would result in a low out-of-plane stiffness of the design.

- **3D-printing:** The final option that was looked into is 3D-printing. Nowadays, 3D-printers are more accessible than they used to be and flexures can easily be printed. Printing is an inexpensive fabrication method and there are a lot of materials that can be used. Therefore, this would be an ideal manufacturing method for a proof of concept.

The fabrication method that is most suitable to realize a demonstrator of the design is 3D-printing. It is an inexpensive fabrication method and can be done in-house at the TU Delft. This allows for quick iterations between design and production because there is no assistance needed from outside the TU Delft.

Now that the fabrication method is known, the material can also be chosen. An ideal material for 3D-printing compliant mechanisms is PLA. This material is strong, flexible and it has sufficient stiffness for the mechanism design. It is one of the easiest materials to 3D-print successfully. However, it also has the downside of losing all stiffness and strength at temperatures above 50 degrees. ABS is more heat resistant but has a lower strength and stiffness than PLA. Therefore, it is decided to build a demonstrator out of PLA. For consistent performance, the temperature should remain at room temperature.

4.4. Optimization

The design of the demonstrator will be optimized to ensure that it meets all the requirements and overcomes all of the design challenges. This optimization is done by adjusting size parameters of the flexure mechanism such that an ideal performance will be achieved. This optimization includes the following: parametric design optimization and investigation into the influence of symmetric design.

4.4.1. Parametric design

The design was modelled in SolidWorks using defined key structural parameters such as flexure length, in-plane width and out-of-plane material thickness. In literature, it was found that the printing direction has only little effect on the overall fatigue behaviour of additive manufactured PLA [3]. Therefore, the finite element analysis can be performed effectively by treating this polymer as a homogenous, isotropic and linear-elastic material. The design is optimized using parametric design in order to achieve the desired characteristics in terms of stress levels, motion range, yaw rotation, stiffness, out-of-plane deflection, and resonant frequency. Parametric design means that the geometric parameters can be varied in the design process and output performance can be evaluated with respect to this parametric variation.

All four of the double parallelogram flexure modules are identical and therefore the modifications made will be the same for each module. The first optimization step is to find the best flexure shape variation in order to reach the desired range of motion with stresses below the yield stress of the material. An axial translation of the end-effector of $5mm$ in both positive and negative direction along both the X and Y axes is required to obtain a workspace of a squared centimeter. To maintain low stresses within the material it is desired to maximize the length of the flexures which is restricted by the compactness requirement of the entire stage. The flexure width in in-plane direction is set to be $0.7mm$, which is known from experience to result in 3D-printed flexures of the highest quality.

A. Stress levels

To rule out plastic deformations of the material, the actual workspace should locate inside the reachable workspace of the design. This means that the maximum stress in the material should stay far below the yield stress. The maximum yield strength of PLA is 26 MPa [21]. Double parallelogram flexure modules have been extensively modelled before and relations between the maximum force, translation and stiffness of the module have been established. The stiffness (K) of a double parallelogram flexure module is given by [25]:

$$K = \frac{F_x}{x_{max}} = \frac{Ebh^3}{l^3} \tag{4.7}$$

Where *b*, *h* and *l* represent the thickness of the material in out-of-plane direction, in-plane flexure width and length respectively. E denotes as the Young's modulus of PLA. The maximum translation in X-direction (x_{max}) is constrained by the maximum yield stress (σ_y) of PLA which is induced by the maximum force (F_x). The previous equation can be rewritten as:

$$x_{max} = \frac{F_x}{K} = \frac{\sigma_y l^2}{3Eh} \tag{4.8}$$

This relation indicates that the maximum translation in X-direction is limited by the length (*l*) and width (*h*) of the flexures for a given material. To obtain a larger translation the flexure length can be increased or the flexure width can be decreased. As previously mentioned it was decided to stick to a value of $0.7mm$ for the flexure width because this results in the highest quality of 3D-printed flexures. This equation can be used to determine the minimum flexure length that can obtain a displacement of $5mm$ while staying below the maximum yield stress (σ_y) of PLA which is found to be 26 MPa [21].

$$l = \sqrt{\frac{3Ehx_{max}}{\sigma_y}} \tag{4.9}$$

This equation shows that the minimum required flexure length has to be at least $37.6mm$. At this length and according to the previously mentioned values, the stress in the material should reach a value of exactly 26 MPa at a maximum deformation of $5mm$. However, in reality the maximum allowable yield stress can be very different and will depend on factors such as manufacturing methods and temperature.

Literature suggests very different values for the maximum yield stress of PLA and this is therefore not a perfect indicator. Especially because additive manufactured PLA will have different material properties than standard PLA. For this reason, the dimensions will be designed against fatigue life which can be done using the normalized design fatigue curve by Ezeh and Susmel (2018) [3] as shown in Figure 4.10. This curve was generated by post-processing the data that Letcher and Waytashek (2014) [9] obtained from experimental results of fatigue testing additive manufactured PLA. This curve is of great relevance for this project because it can be used to estimate the amount of cycles to failure under maximum pressure conditions in the material.

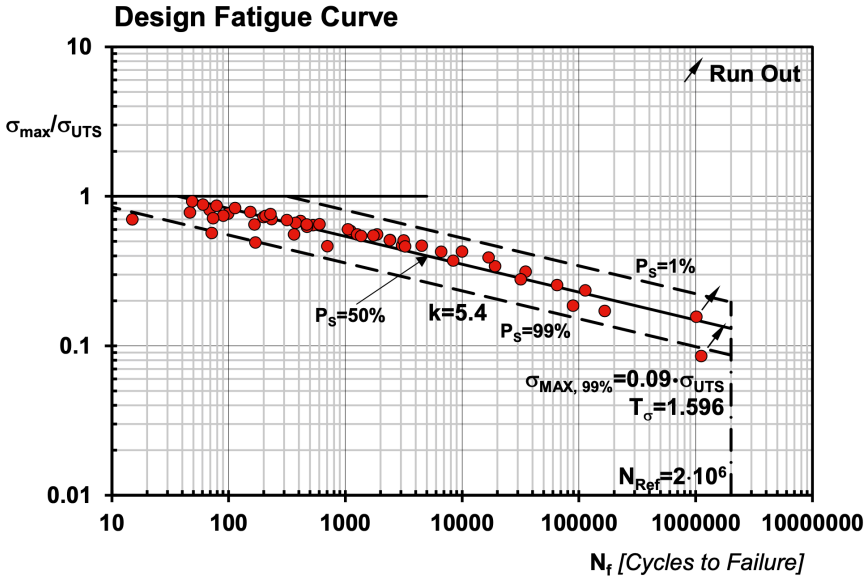

Figure 4.10: Design fatigure curve of additive manufactured PLA [3].

In order to make an estimate of the amount of cycles to failure it is necessary to know both the maximum stress within the material at the desired deformation, and the ultimate tensile strength of additive manufactured PLA. As shown in Figure 4.10 the ratio between these two corresponds to a number of cycles with a certain probability of survival *Ps*. A COMSOL model is used to determine the maximum von Mises stress in the flexure mechanism while achieving the desired deformation. The maximum stress was found to be 8.67 MPa.

The ultimate tensile strength is determined experimentally by Afrose et al. (2016) [3] for multiple filament orientations ($\theta_f = 0°, \theta_f = 45°, \theta_f = 90°$). The results were $\sigma_{UTS} = 38.7MPa$, $\sigma_{UTS} = 31.1MPa$, and $\sigma_{UTS} = 33.6MPa$ respectively. The lowest ultimate tensile strength is used for determining the amount of cycles to failure to make a conservative estimate.

The ratio is found to be: $\frac{\sigma_{max}}{\sigma_{UTS}} = \frac{8.67MPa}{31.1MPa} = 0.279$. This corresponds to $N_f = 30.000$ cycles to failure at 50% probability. Note that the amount of cycles to failure is an estimate for the amount of cycles where the flexure reaches a displacement of $5mm$. When the desired displacement is decreased to $2.5mm$ the amount of cycles will be $N_f = 1.000.000$ at 50% probability.

The length of the flexures could be decreased while staying far below the yield stress. But it is decided to adhere to the advice given by Howell for precision flexure modules. Namely, that devices with intermediate deflections, which are in the range of 10 % of the flexure beam length, are considered ideal for precision devices and common in positioning and measurement systems. The decision to adhere to flexure lengths of $50mm$ can be justified using the design fatigue curve as explained above in order to guarantee a minimum amount of cycles to failure. Therefore, it is decided to preserve a flexure length of $50mm$ within the flexure modules. When this parameter is decreased, it will result in a more compact design but it comes at the cost of a lower precision and shorter lifetime.

B. Motion range

The objective of the design is to allow guided linear motion throughout the entire workspace. For this to be possible, the flexure module should be designed such that it does not collide with itself while reaching the outer boundaries of the workspace. This introduces a parameter (*f*) as shown in Figure 4.11a for the minimum required gap between the outer flexure pairs of the modules. A translation of $5mm$ in both directions is required and therefore the gap should at least be $5mm$ on both sides. To compensate for some expected parasitic errors a safety margin is introduced. This safety margin is chosen to be 20% which results in a required gap of $6mm$ on both sides. Figure 4.11b shows that the module is capable of achieving a $5mm$ translation without colliding with itself.

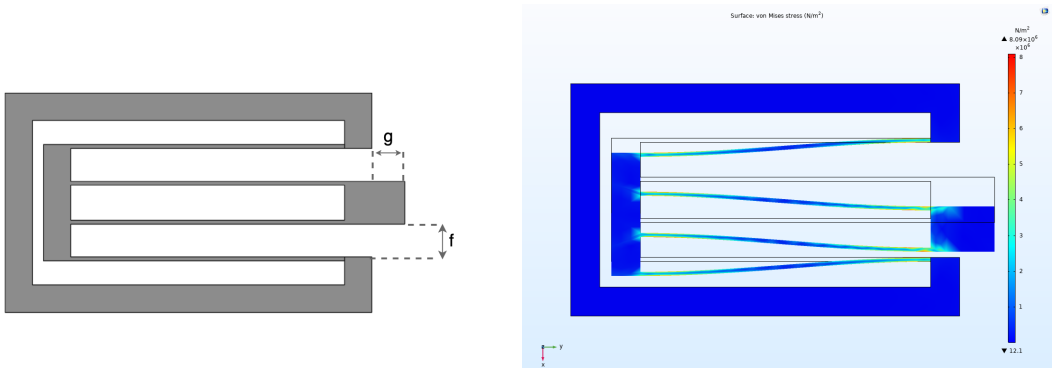

(a) (b)

Figure 4.11: **(a)** Double parallelogram flexure module with parameter (*f*) which is the gap required between flexures to allow $\pm 5mm$ motion without collision within the flexure module. Parameter (*g*) shows the required length of connection blocks to avoid collision with the other flexure modules. **(b)** COMSOL simulation showing the flexure module with a deformation of $5mm$ in the drive direction.

While reaching the outer boundaries of the workspace, the flexure module should also avoid collisions with the other flexure modules. This introduces a parameter (g) as shown in Figure 4.11a for the required minimum length of the connection block between two modules. To compensate for some expected parasitic rotation and motion, this length is increased with the same safety margin as mentioned earlier, such that the stage will not collide with itself even though parasitic errors are present. The minimum gap between two adjacent flexure modules should be 6mm. Figure 4.12 shows the new structure which is formed by assembling the modified building blocks. A frame is added around the mechanism to ensure robustness of the design. COMSOL simulations were performed to ensure that the motion stage is able to move throughout the entire workspace without colliding with itself.

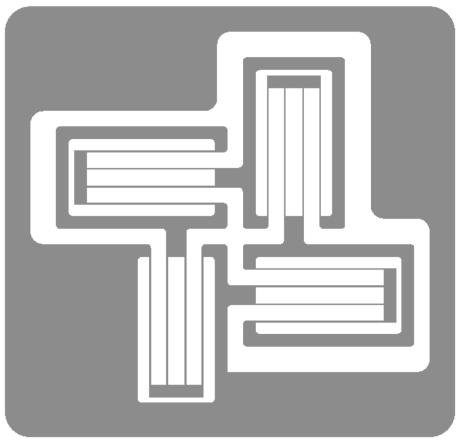

Figure 4.12: The updated structure of the mechanism design.

C. Yaw rotation

In the current design, parasitic errors such as yaw rotation can be expected. This yaw rotation reaches a maximum at the outer corners of the workspace as shown in Figure 4.13. The maximum is measured in the upper left and lower right corner where the rotation of the motion stage reaches an angle of $0.73°$. Reaching the upper right and lower left corners of the workspace results in a parasitic rotation of $0.16°$ in both cases. This parasitic rotation is not desired because it affects the performance of the motion stage negatively.

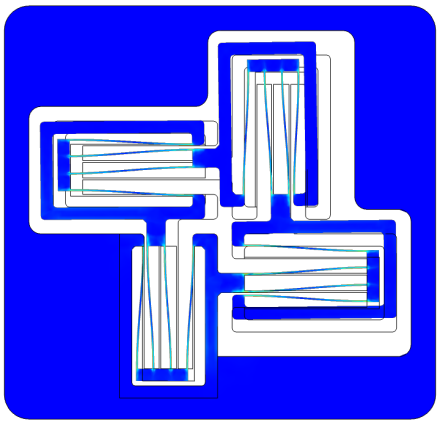

Figure 4.13: This simulation depicts the maximum yaw rotation ($0.73°$) of the motion stage with the X-direction actuated to $-5mm$ and the Y-direction actuated to $+5mm$.

Exploitation of the center of stiffness is used to minimize yaw rotation. This can be done by shifting the connection between two adjacent flexure modules in such a way that the centers of stiffness align as shown in Figure 4.14. It also helps when the actuators are placed in line with the center of stiffness of the modules that they are attached to. When the center of stiffness is subjected to lateral loading, only a translational displacement can be expected. Hence, parasitic rotation can be avoided. However, some parasitic rotation may be allowed because removing parasitic rotation entirely is a trade-off between having no parasitic rotation and the compact design requirement.

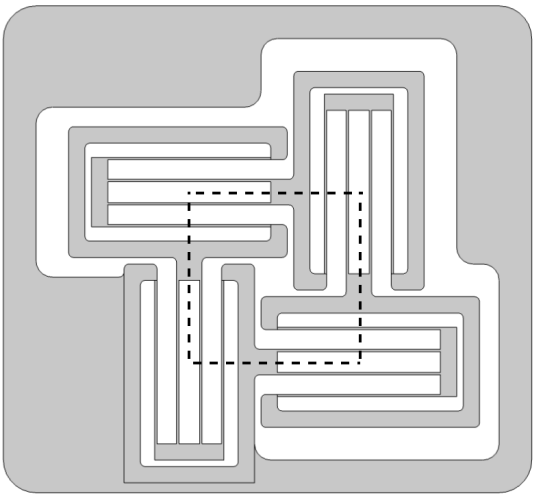

Figure 4.14: The mechanism design after shifting the modules such that the centers of stiffness of adjacent modules are on the same line.

After shifting the center of stiffness, a slight decrease is seen in the parasitic rotation angle and the design has transformed into a more compact design. The maximum yaw rotation when the stage reaches the upper left and lower right corner stays the same at $0.73°$. The maximum yaw rotation when the stage reaches the lower left and upper right corner has decreased from $0.16°$ to $0.11°$. The amount of parasitic rotation that was found is allowable and will not affect the performance of the stage because of the stitching procedure.

D. Stiffness and actuation force

To satisfy the specification of $\pm 5mm$ stroke in both X- and Y-direction, the voice coil actuators must have sufficient actuating force. Therefore, it is important to make an estimate of the required force such that a suitable actuator can be chosen for the stage. Since deformations will only be within the elastic domain, the force displacement curve will be of linear form. The following force displacement curves as shown in Figure 4.15 were established from data that was derived from finite element analysis using COMSOL and from analytical calculations. The curves are the same for X- and Y-actuation and assuming that only one axis is actuated at a time. It is important to realize that the stiffness of the flexure mechanism can vary as the motion stage moves through the workspace due to effects of cross-axis coupling.

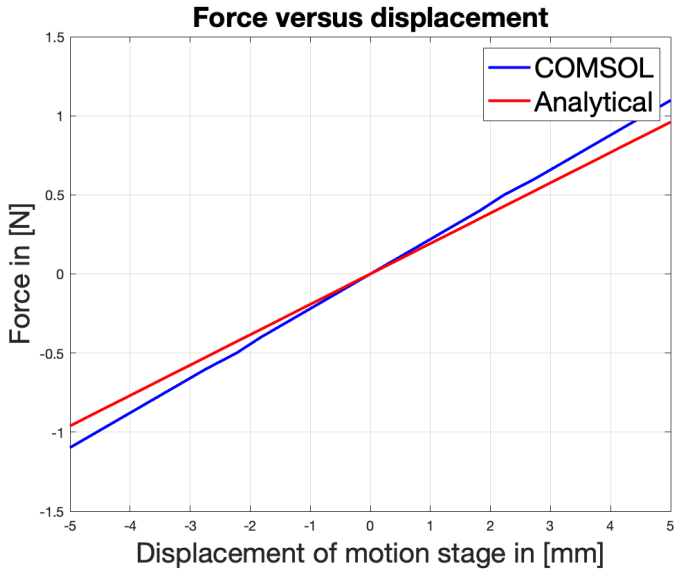

Figure 4.15: Force displacement curve

The results show that the maximum force the actuator must have is around 1.1 Newton. Slight differences are found between the COMSOL and analytical results. This difference is so small that it is negligible. It should be noted that these estimates are based on measurements at room temperature. If the temperature increases, the stiffness of the mechanism will decrease. At 40 degrees the material will start showing a decrease in strength and stiffness and at 50 degrees the material will have lost all of its strength and stiffness. Therefore, the operating temperature should not exceed 40 degrees. Ideally, it should remain at room temperature to provide consistent performance.

E. Out-of-plane deflection

The out-of-plane stiffness of the flexure mechanism as a whole is low due to a combination of two factors. First of all, the individual flexure modules have low stiffness in out-of-plane direction. This stiffness could be increased by choosing a larger out-of-plane thickness. This would however result in a higher force required for actuation. It will also increase the size of the stage which is not desired. Another factor for low out-of-plane stiffness is caused by the fact that the motion stage overhangs with support only from one side. This could be solved by mirroring the current design such that the motion stage is supported from two sides. However, this will increase the size of the precision stage with almost a factor two. In this case, the compactness requirement is prioritized over the out-of-plane deflection requirement. Staying within autofocus range of the microscope is sufficient for this project.

A COMSOL simulation was done to determine the deflection in the out-of-plane direction as the motion stage moves through the workspace. This simulation does not take the initial deviation into account caused by gravity of the overhang mechanism. It is assumed that this intitial deviation is eliminated from the system by calibration of the autofocus. Therefore, it is sufficient to ensure that the maximum deviation in out-of-plane direction while moving the motion stage through the workspace, is within the boundaries of the autofocus working range. Calibration is done while the motion stage is unactuated. The simulations performed in this evaluation are relative to the initial position. A maximum deflection of $1\mu m$ was found. In real life applications this may or may not be realistic depending on the alignment of the actuators. This deflection is well within the $\pm 100\mu m$ autofocus scanning range of the microscope and therefore an allowable value.

F. Resonant frequency

The COMSOL model is used to predict the mode shapes of the mechanism design. To enable fast XY positioning with high stability and a wide working bandwidth, a high first resonant frequency of the stage is desired. Using FEA the first five natural frequencies were found and are shown below in Table 4.2.

Mode shape	Frequency [Hz]
X-translation	13
Y-translation	14
Out-of-plane of motion stage	20
Out-of-plane of intermediate stage 1	40
Yaw rotation of motion stage	59

Table 4.2: Natural frequencies that were found using FEA.

The existing compliant positioning stages as found in literature have a high first natural frequency because their motion range is relatively small. This compliant stage has a higher motion range and that comes at the cost of a lower primary stiffness, which results in a lower first natural frequency. The first and second mode shapes are translations along the X- and Y-axes and occur at $13Hz$ and $14Hz$ respectively. The third mode shape presents an out-of-plane deflection of the motion stage and it occurs at $20Hz$. The fourth mode shape is an out-of-plane deflection of intermediate stage 1 and it occurs at $40Hz$. This indicates that the intermediate stage is under-constrained because it has an uncontrolled degree of freedom. The final mode shape that is shown here is a yaw rotation of the motion stage itself, which occurs at $59Hz$.

4.4.2. Symmetric design

The design performance could be enhanced by implementing symmetry into the design. Several designs were generated that resulted in better performance. Meanwhile, they also drastically increased the size of the design which goes against the compactness requirement. Therefore, it is decided to not implement symmetry into the mechanism but it is shown here because it can be used for future applications. An advantage of implementing symmetry into the design is that the overhang support in the current design is improved to a design where the mechanism is supported from two sides as shown in Figure 4.16a and in Figure 4.16b. This offers increased out-of-plane stiffness and makes the motion stage less prone to yaw rotation.

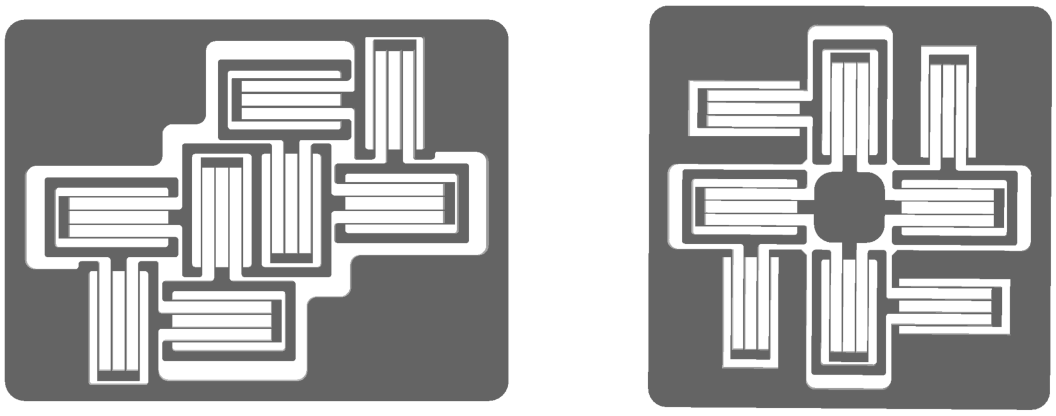

(a) (b)

Figure 4.16: Both mechanism designs are based on symmetry and show increased stiffness in out-of-plane direction and they minimize yaw rotation of the motion stage. **(a)** The resulting mechanism design after mirroring of the current design. **(b)** A mechanism design that makes use of symmetric modular design [1].

4.5. Actuator

This chapter describes the actuator selection and integration into the system while taking into account the challenges as listed in Chapter 3.5.

4.5.1. Selection

The actuator has to be capable of large range and micrometer motion quality to meet the desired objective. A voice coil actuator is used for actuation of the precision stage. This was decided due to the fact that it is direct-drive and provides linear motion with high resolution and accelerations while it can achieve the required travel range for blood smear analysis. Other reasons are because of its negligible hysteresis, lack of cogging or commutation and small size. Applying a voltage across the terminals of the motor causes the motor to move in one direction. The direction of actuation can be changed by reversing the polarity of the applied voltage such that the actuator will actuate in opposite direction. The generated force of a voice coil motor is proportional to the current that flows through the motor coil. This force is almost constant in the specified stroke range of the motor. Another advantage of voice coil motors is that they are free of friction and backlash. The combination of the above makes a voice coil motor the most suitable actuator for the precision stage. One disadvantage of the voice coil actuator is that when the coil moves rapidly, the magnet induces a current in itself opposing the current of the driving voltage. This is referred to as a 'back EMF'. However, this effect can be neglected at slow operating speeds.

There are two types of voice coil motors that could be selected for the demonstrator. One has an internal bearing which simplifies aligning the motors but is way more expensive. The alternative is a voice coil motor without internal bearing. This motor is cheaper but on the other hand it is harder to integrate in the system. Both actuators are shown below in Figure 4.17. From a cost point of view, the motor without internal bearing as shown in Figure 5.2b was chosen. Buying in bulk reduces the cost per unit to $150\$$.

(a) (b)

Figure 4.17: **(a)** Linear voice coil motor with internal bearing [14]. **(b)** Linear voice coil motor without internal bearing [15]

For the precision stage, an actuator with a stroke of $10mm$ is required. COMSOL simulations showed that a force of 1.1 Newtons is required to actuate the motion stage to the desired displacements ($\pm 5mm$) in both X- and Y-direction. Therefore, the voice coil actuator should also be capable of delivering this force. It is important to choose an actuator with a low moving mass. The higher the moving mass, the bigger the impact will be on the dynamics of the system. An actuator was chosen of which the specifications are displayed in Figure 4.18. An extended specification sheet of this actuator is shown in Appendix B.

INTERMITTENT FORCE @10% DUTY CYCLE	5.4 N	19.3 OZ
CONTINUOUS FORCE	1.7 N	6.1 OZ
FORCE CONSTANT	1.7 N/A	6.3 OZ/A
BACK EMF CONSTANT	1.7 V/M/S	0.04 V/IN/S
STROKE	12.7 mm	0.50 IN
COIL CLEARANCE PER SIDE	0.32 mm	0.013 IN
COIL ASSY MASS	9 GR	0.32 OZ
BODY MASS	17 GR	0.60 OZ
COIL RESISTANCE	4.6 Ohms	
COIL INDUCTANCE @ 1000 Hz	0.8 mH	
MAX CONTINUOUS POWER	4.4 W	

ALL VALUES AT 25°C

Figure 4.18: Specification sheet of the selected linear voice coil motor without internal bearing [15].

4.5.2. Integration

Integration of the actuators into the precision stage is done according the actuator isolation principle as described in Chapter 3.5. Which means that the actuator should be attached to the flexure mechanism in such a way that the actuator tip will only move along the line of actuation and no transverse loads are applied. The ideal location to attach the X- and Y-actuators are on intermediate stages 1 and 2 respectively. Voice coil actuator 1 can be attached to intermediate stage 1 which is constrained to move only along the X-axis. Voice coil actuator 2 can be attached to intermediate stage 2 which is constrained to move only along the Y-axis. This method will result in less parasitic rotation and thus yield a higher precision of the motion stage.

The permanent magnet of the voice coil actuator is connected to the ground frame as the stator while the coil is connected to the flexure mechanism as the mover as shown in Figure 4.19.

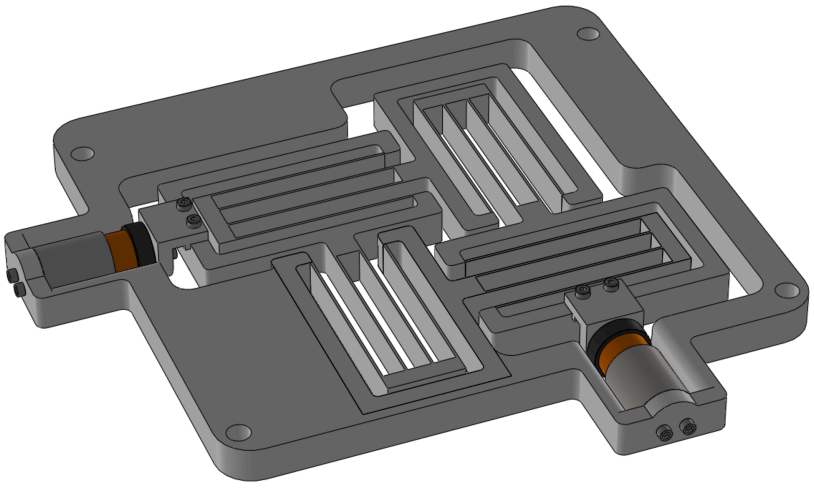

Figure 4.19: Integration of the voice coil actuators into the mechanism design.

This offers the advantage of lower moving mass which is preferable for high-frequency actuation. The moving coil of the actuator can be attached directly to the flexure mechanism. There is no need for an additional bearing to support the linear motion of the actuator because the flexure mechanism itself will function as a linear bearing. The actuator could also be positioned the other way around where the magnetic housing acts as the mover that is attached to the flexure mechanism and the coil attached to the ground frame as the stator. This would have the advantage of no moving coil and thus no moving wires which could be a source of disturbance. Another advantage would be that the ground

frame is better able to dissipate the heat that is generated in the coil due to the actuation current than the flexure mechanism itself. This is because the frame has a greater thermal mass and surface area. This problem could be solved by introducing a decoupler between the moving coil and the flexure mechanism. The decoupler is better able to channel and dissipate the heat than the flexure mechanism and it also simplifies assembly. It is decided to go for the option where the dynamics of the system will be affected the least. Therefore, a decoupler is introduced between the moving coil and the flexure mechanism as shown in Figure 4.20. This will also simplify assembly.

(a) (b)

Figure 4.20: **(a)** Linear voice coil motor with the decoupler attached. **(b)** Exploded view of how the decoupler is attached and aligned.

As previously stated, the wires that are attached to the coil can be a source of disturbance. Every stroke of the actuator will cause the wires to move. It is expected that this rapid movement of the wires will not damage the wires itself since the maximum stroke is only $10mm$. To prevent heat dissipation from the permanent magnet into the ground frame it is recommended to install the motor on a metallic body for proper heat sinking. This could be done by adding an aluminum washer between the ground frame and the permanent magnet.

4.6. Final design

The current design should meet the requirements but this still has to be confirmed. This can be done by experimental validation in which the performance will be measured. To be able to carry out the experiments, a reference point is put on top of the motion stage. The position of this reference point was chosen to be in the lower left corner of the fourth flexure module because this is the location where its weight will have the lowest effect on the out-of-plane deflection. The reference point can be used for experimental performance evaluation where a triangulation sensor can be used to measure the distance to this reference point.

Also, the mechanism is supported by four legs that are installed in each corner to make the mechanism design floating. This is to ensure that no friction between the mechanism and the ground will occur. These modifications are shown in Figure 4.21a. This figure shows that the demonstrator is designed for plug-and-play. The user only has to install the voice coil actuators into the mechanism design using 2-56 socket head cap screws. The mechanism is designed in such a way that the actuators should be perfectly aligned when installed since they can only be installed in one manner. Figure 4.21b shows an exploded view of the assembly such that the components can easily be identified and insight is created in how to assemble the parts.

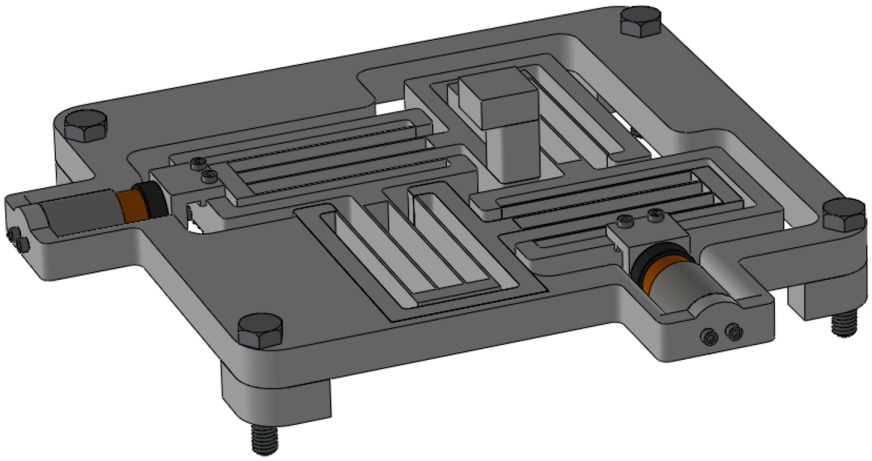

(a)

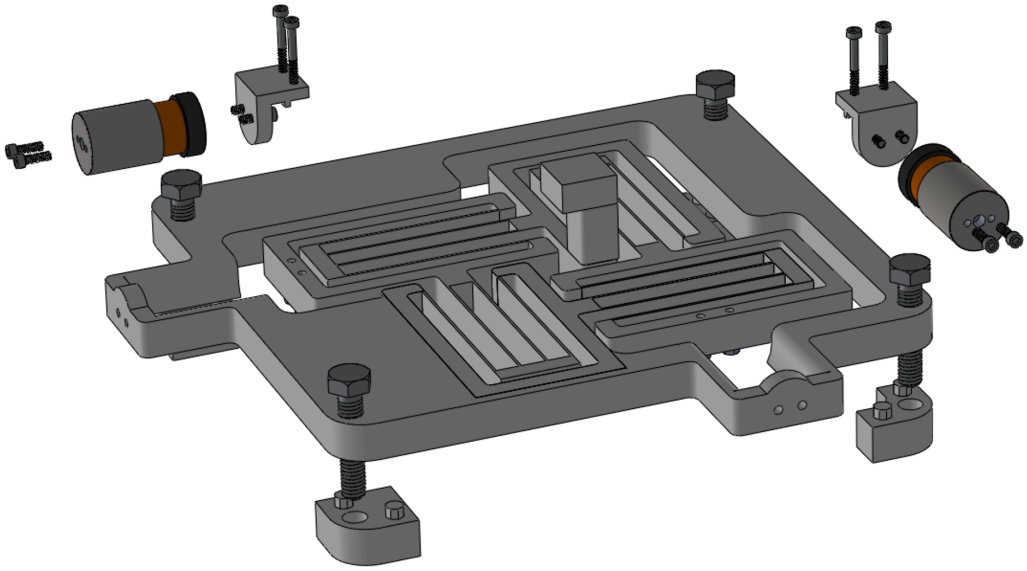

(b)

Figure 4.21: **(a)** The demonstrator when proper assembled. **(b)** An exploded view of the design showing the order of assembly of various parts.

4.7. Bulk cost estimation

The cost per unit in bulk production is estimated while only including costs of materials and components. The following individual components and their price for bulk purchase from large suppliers are shown in Table 4.3.

Component	**Quantity**	**Bulk cost per unit** [$]
Compliant motion stage	1	3.00
Voice coil motor	2	150
M2-56 - 8mm bolt	8	$0.03 - 0.05$
M3 - 16mm bolt	4	$0.04 - 0.07$
M3 nut	4	$0.04 - 0.07$
M4 - 25mm bolt	4	$0.05 - 0.09$
Total estimated costs		≈ 300

Table 4.3: Estimation of bulk production costs per stage.

The total estimated costs per stage are found to be approximately $300\$$. It costs only $\approx 3.00\$$ to 3D-print the design of the compliant motion stage. A large percentage (99%) of the costs are due to the expensive voice coil motors that are used for actuation. Even though there is still a lot of room for improvement by finding a cheaper alternative for actuation this is still a good result.

To use this stage for automated malaria diagnosis in developing countries, certain control hardware is required to complete the system. In order to make an estimate of the complete system costs, the following costs as shown in Table 4.4 will be included for a cost comparison with the standard hematology analyzer. It is assumed that the microscope and laptop are already available in the local doctor's practice and therefore these costs will not be included.

Component	**Quantity**	**Bulk cost per unit** [$]
Arduino Uno	1	3.00
L298N Driver (dual H-Bridge)	1	0.70
12V Power supply	1	1.20
Total estimated costs		≈ 5.00

Table 4.4: Bulk cost estimation for control hardware required for automated malaria diagnosis.

A standard hematology analyzer costs around $10.000\$$, while this system has a total cost of $\approx 300\$$. This total does not include the costs of the microscope and laptop since it is assumed that those are already available. The total system cost is almost thirty times cheaper than the hematology analyzer which makes it affordable for local doctor's practices. The compliant motion stage that was designed in this research costs only $\approx 3.00\$$. This is a promising result and if an alternative can be found for the expensive voice coil actuators, then the total system cost can even be reduced significantly.

4.8. Compactness ratio

The scientific contribution of this research is to design a long-stroke compliant precision stage with compact design. The performance with respect to compactness of the design is compared to existing stages by looking at an area ratio of workspace to planar dimension. Multiple compliant XY-stages were used for this comparison which are shown below in Table 4.5.

	Kinematics	**Workspace** [mm]	**Area** [mm]	**Ratio**
-	Parallel (XY)	$10x10$	$125x125$	$6.4 \cdot 10^{-3}$
[20]	Parallel (XY)	$2.0x2.0$	$100x100$	$4.0 \cdot 10^{-4}$
[22]	Parallel (XY)	$1.8x1.8$	$110x110$	$2.7 \cdot 10^{-4}$
[12]	Parallel (XY)	$1.5x1.5$	$300x300$	$2.5 \cdot 10^{-5}$
[7]	Parallel (XY)	$2.0x2.0$	$100x100$	$4.0 \cdot 10^{-4}$
[11]	Parallel (XY)	$20x20$	$430x430$	$2.2 \cdot 10^{-3}$
[10]	Parallel (XY)	$0.12x0.12$	$230x230$	$2.7 \cdot 10^{-7}$

Table 4.5: Compactness ratio comparison with stages as found in literature. The upper row shows the results for the designed stage.

The mechanism designed in this research has planar dimensions of $12.5cm$ by $12.5cm$ and it can operate within a workspace of $10mm$ by $10mm$. Therefore, it has an area ratio of workspace to planar dimensions of $100/15625 = 6.4 \cdot 10^{-3}$. The planar area of the mechanism design can be reduced if smaller flexure lengths are used which would result in a shorter lifetime of the system due to higher stresses in the flexures. Also, the mechanism frame is redundant and only present to ensure rigidity. Therefore, planar dimensions can be reduced resulting in the following area ratio: $100/10000 = 1.0 \cdot 10^{-2}$. This introduces a trade-off between the life of cycles and a compact design. Since the mechanism is compact enough for integration into a microscope and all the requirements for blood smear analysis are being met, we can conclude that the scientific research gap has been investigated successfully. That the research gap is investigated successfully is also confirmed through comparison of the compactness ratio to existing stages from literature. Therefore, the methodology that was used to design a long-stroke compliant precision stage with compact design was very effective.

To show that the design is more compact than a hematology analyzer, both are shown next to each other in Figure 4.22.

(a) (b)

Figure 4.22: **(a)** A standard hematology analyzer that is used for blood smear analysis [8]. **(b)** The compact stage that was designed as alternative to a hematology analyzer. Note that it is shown without a power source, microcontroller, driver or computer.

The setup that was designed is a lot more compact than the hematology analyzer. It should be taken into account that the complete setup which can be used for malaria diagnosis will be larger than just

the microscope and the integrated precision stage that are shown in Figure 4.22b. This is because the voice coil actuators will also need a power source, Arduino, and driver for control. Also, a computer is required to be able to run the vision algorithm to detect the presence of malaria and its species.

5

Experimental setup

This chapter describes all the manufacturing steps that were done to come to the final design of the demonstrator. It also shows how the experimental setup was built and which hardware and/or software was used to conduct the performance evaluation measurements for validation of the demonstrator.

5.1. Manufacturing

The first manufacturing step occurred during the detailed design phase. This step was to print a prototype for proof-of-concept. The prototype shown in Figure 5.1 was used to evaluate the quality of the print and to see whether the motion range can be reached without excessive stress levels. The outcome of this evaluation was that the design worked exactly as expected and that no design alterations had to be done.

Figure 5.1: First prototype 3D-printed out of PLA for proof of concept.

After careful evaluation of the prototype, a final design as shown in figure 5.3 was realized that can be used as a demonstrator to evaluate the performance. This final design of the demonstrator includes a reference point on the end-effector of the motion stage which can be used for displacement measurements. For the experiment, two laser triangulation sensors were used. The laser mounts were 3D-printed and can be integrated into the system. After calibration they can be removed.

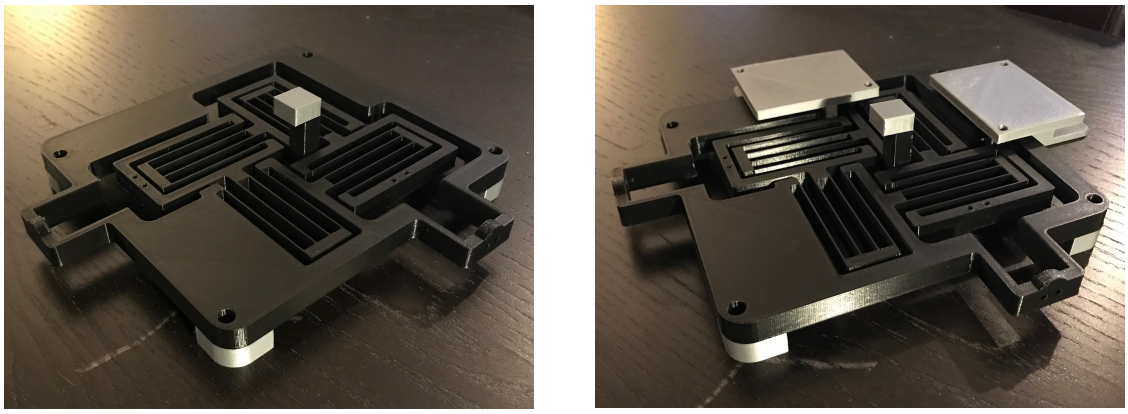

(a) (b)

Figure 5.2: **(a)** The final 3D-printed demonstrator with the reference point shown in grey. **(b)** This figure also shows the sensor mounts that can be removed after calibration.

5.2. Experiment

During the experiment, the demonstrator is installed on a Thorlabs aluminum breadboard which is a convenient platform to conduct experiments. It contains multiple M6 tapped holes which allow components to be mounted and aligned with high precision. This simplifies assembly of the experimental setup and ensures high reproducibility of the experimental measurements. The stage is mounted on the four legs which in turn are mounted on the breadboard. To evaluate the performance during the experiment, two laser triangulation sensors are used of which the specification sheet can be found in Appendix C. The sensors are mounted on a sensor mount that aligns the lasers such that the initial position of the reference point is in the mid-scanning range of the lasers. An overview of the experimental setup is shown in Figure 5.3b. This figure also shows the laser beams that are reflected by the reference point such that the relative displacements can be determined.

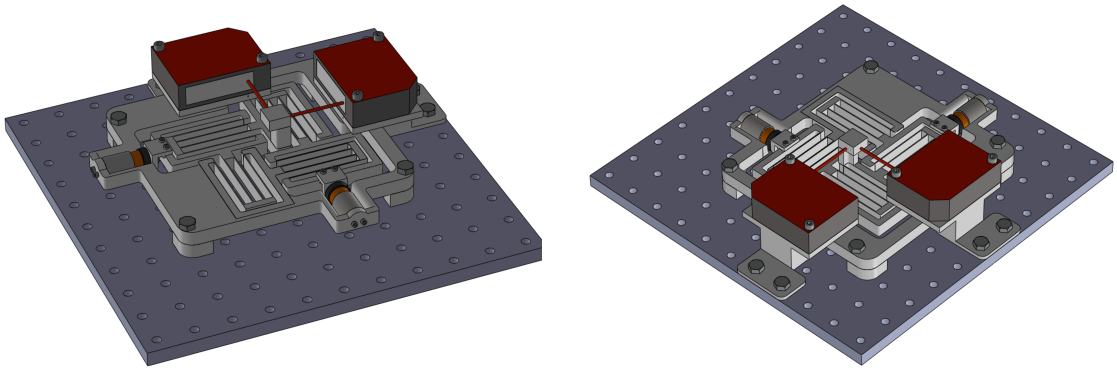

(a) (b)

Figure 5.3: **(a)** Front view of the experimental setup. **(b)** Back view of how the sensors are mounted.

The experimental setup as modeled above was assembled in the Mechatronics lab within the Department of Precision and Microsystems Engineering at TU Delft. This setup is shown below in Figure 5.4. This experimental setup is used for the following measurements: step response, repeatability, linearity and frequency response. The hardware that is used for control and data acquisition are two separate USB-6211 DAQ's from National Instruments which are controlled using LabVIEW. One power supply is used to actuate both voice coil motors.

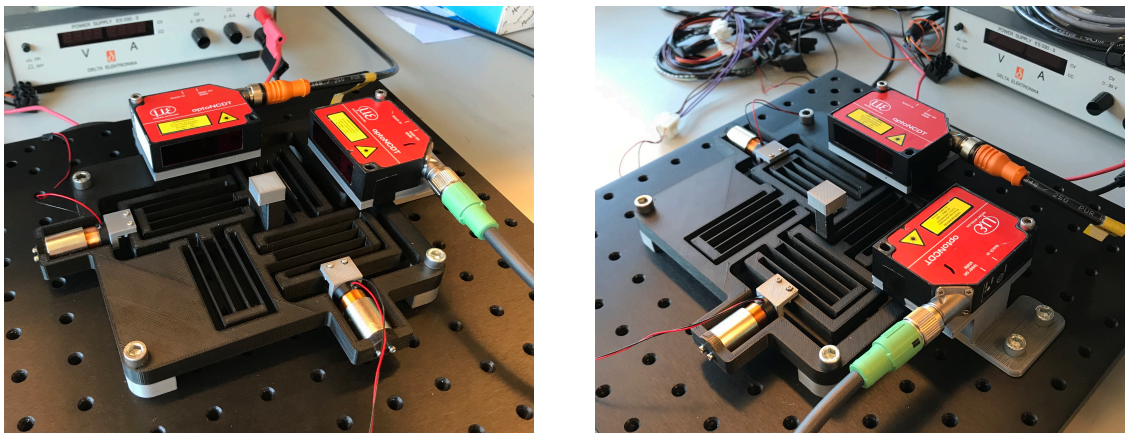

(a) (b)

Figure 5.4: **(a)** Front view of the experimental setup. **(b)** Back view of how the sensors are mounted.

To measure the out-of-plane deflection during actuation, another setup is required. A frame is built and mounted on the Thorlabs breadboard to be able to keep the sensor that measures out-of-plane deflection in place. The new experimental setup is shown in Figure 5.5. Figure 5.5b shows the laser beams that are incident on the reference point. One laser triangulation is used for measuring the traveled distance in X-direction while the other laser measures the corresponding deflections in out-of-plane direction.

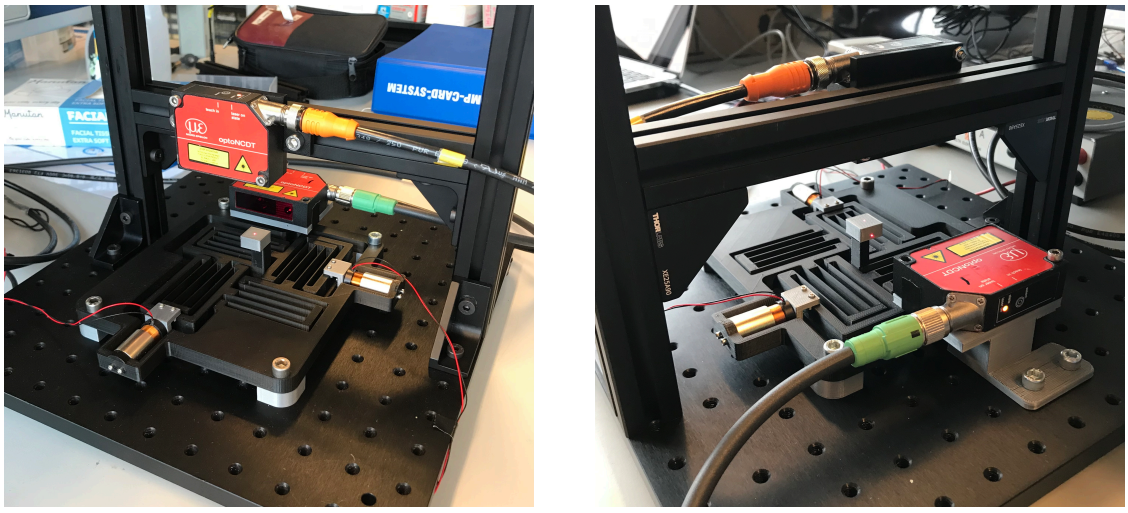

(a) (b)

Figure 5.5: **(a)** Front view of the new experimental setup. **(b)** Back view that shows how the laser beams are incident on the reference point.

6

Performance evaluation

The performance of the demonstrator is measured in terms of five criteria. First, a step response is performed in the X- and Y-direction separately to determine the settling times. An input shaper is designed which can be used to reduce settling times if desired. The step response measurement is then repeated multiple times to determine the repeatability of the system. The relation between input voltage and displacement of the motion stage is obtained through measurements and the stage is evaluated on its linearity while moving through the workspace. Then system identification will take place using measurements of the system's input and output signals at different frequencies. At last, the parasitic motion in out-of-plane direction is measured to ensure that deflections stay within the autofocus range of the microscope.

6.1. Settling time

A step response measurement is performed to determine the settling time. This gives a good indication of the system performance because a faster settling time will result in a shorter scanning time. The step response is also a good indicator of the overall stability of the stage. The step response is measured for a step size of 127 μm since this is the step that will be taken throughout the blood smear analysis procedure in order to obtain a new field of view. The settling time is defined as the time required for the response curve to reach and stay within a range of 5 % of the equilibrium value without subsequently deviating from it by that amount. The system was calibrated before the measurements were done to ensure that a 127 μm displacement of the motion stage gives a sensor output of 127 μm. The measurement was performed in both the X- and Y-direction and the results are shown in Figure 6.1a and Figure 6.1b respectively.

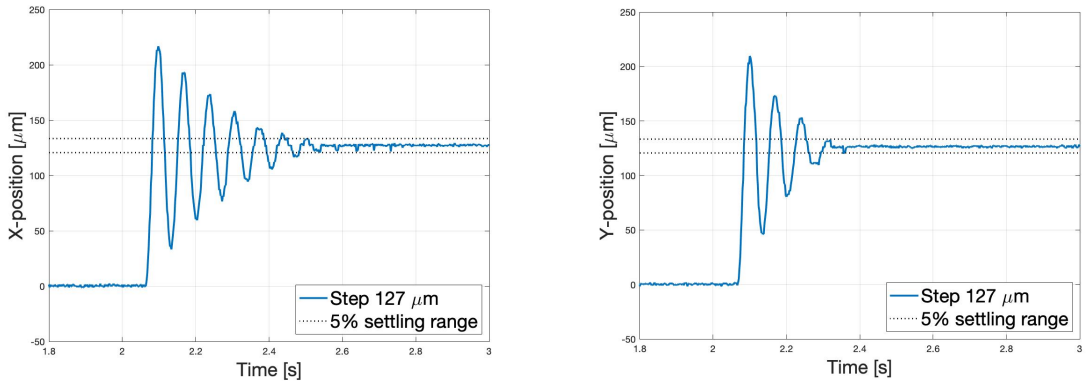

(a) (b)

Figure 6.1: Step responses with the required step size of $127 \mu m$ in: **(a)** X-direction which has a settling time of $0.4 s$. **(b)** Y-direction which has a settling time of $0.2 s$.

The step responses in X- and Y-direction have an overshoot of $90\mu m$ and $80\mu m$ respectively. The settling time of a $127\mu m$ step is $0.4s$ in X-direction and $0.2s$ in Y-direction. The differences in settling time are caused by a different damping ratio in the two working axes which in turn are caused by different modal masses. This difference in modal masses was previously observed during the natural frequency analyses using COMSOL which also showed a different natural frequency in X- and Y-direction. The step response in X-direction shows poor performance in terms of settling time which is caused by a low damping ratio that results in a long lasting vibration. The step response in Y-direction shows better performance in terms of settling time due to a higher damping ratio.

According to the requirements, the settling time should be below 0.1 seconds. Since this is not achieved, feedforward control can be used to reduce the settling time. This can be done by applying a pre-filter where the input is shaped in such a way that vibrations are cancelled. In order to design this pre-filter, a transfer function is derived that matches the measured step response in X-direction. This transfer function is plotted below in Figure 6.2. This pre-filter is only designed for actuation in X-direction since it will only be used to demonstrate the possibilities of feedforward control for this positioning stage and it will not be implemented in the stage for further measurements.

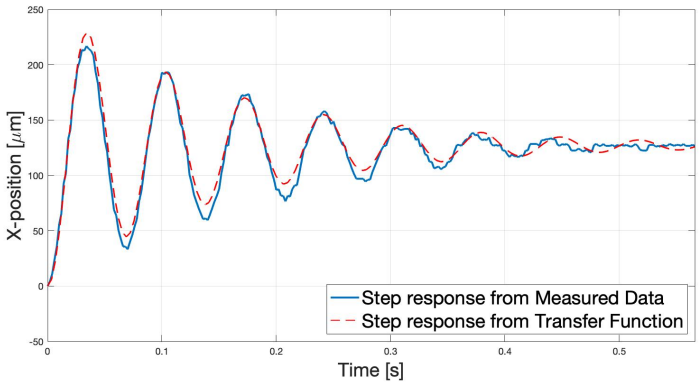

Figure 6.2: Step response from measured data in X-direction and the step response of the transfer function that was derived.

Now an input shaper can be designed that makes use of two different impulses to cancel out vibrations and thus reduce the settling time. The first impulse (with amplitude $A1$ and time $t1$) causes the system to vibrate, while a second properly timed $(t2)$ and sized impulse A2 will cancel the vibration induced by the first impulse. This is referred to as zero vibration input shaping and is shown in Figure 6.3.

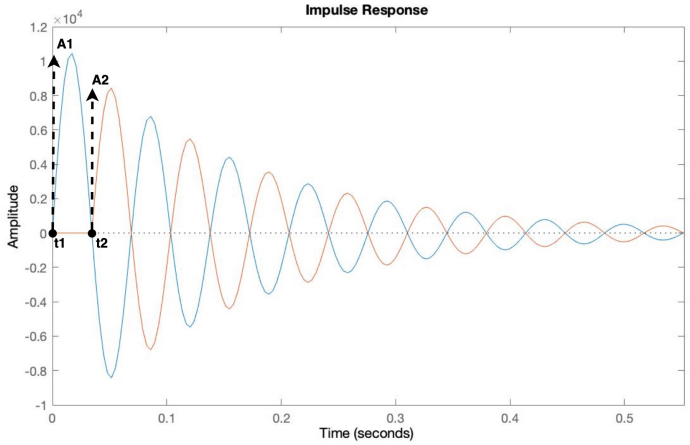

Figure 6.3: Impulse response of two properly timed impulses to cancel out vibrations.

If we have perfect knowledge of the system and the system is stable in time, then zero vibration shaping offers the best performance. However, if there are system uncertainties, then the zero vibration derivative can be used to create a more robust input shaper. Both are plotted in Figure 6.4. The derivative is similar to the normal zero vibration but it differentiates itself by adding a third properly timed and sized impulse to cancel the vibrations in an even more robust way.

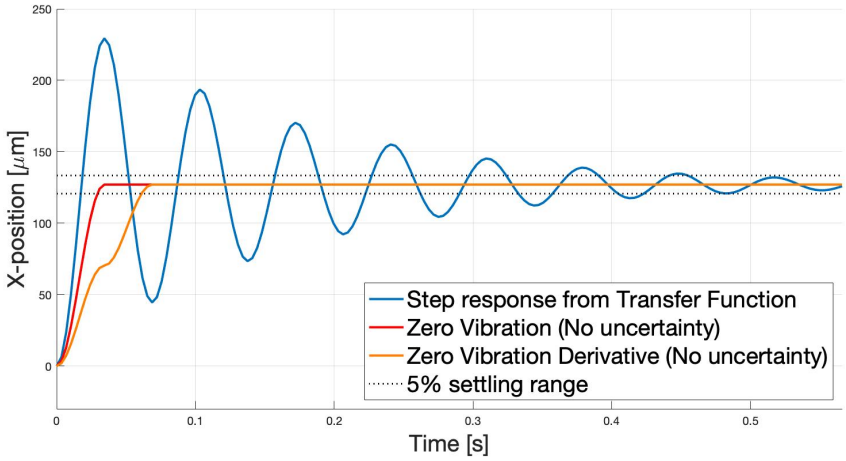

Figure 6.4: Zero vibration and zero vibration derivative input shapers without system uncertainties.

This figure shows that zero vibration input shaping results in a reduced settling time of $34ms$, which meets the requirements. This comes at the cost of a higher rise time but that is not relevant for this application. The figure also shows the result of a zero vibration derivative input shaper. The settling time will increase compared to the zero vibration shaper, but it results in a robuster system that offers better performance when the system shows different behaviour. This can be demonstrated by adding system uncertainties which results in the following behavior as shown in Figure 6.5.

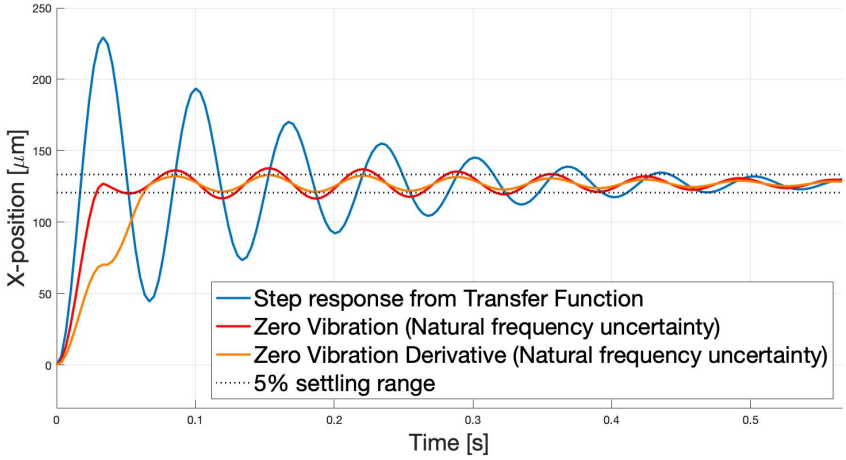

Figure 6.5: Zero vibration and zero vibration derivative input shapers with frequency uncertainty.

This figure shows that the zero vibration derivative offers better performance with system uncertainties. Even though in this case it is better than the zero vibration shaper, it should be noted that both shapers show a better performance than the original signal. The input shapers will not be used for further experiments but are only used to showcase the possibilities of feedforward control. The settling time obtained with a zero vibration input shaper, combined with the autofocus specifications, can be

used to derive the total scanning time for the malaria diagnosis procedure. The scanning procedure of the stage takes only 3.4 minutes, including time for the autofocus to stabilize and obtain sharp images this results in a total scanning time of approximately 17 minutes. This is faster than manual diagnosis $(60min)$ and comes close to the speed of a hematology analyzer $(2min)$ at a fraction of the cost.

6.2. Repeatability

The repeatability of the stage is of great relevance because it shows the range (variation) of measurements achieved for multiple test points under consistent experimental conditions. A unidirectional repeatability test is performed by analyzing thirty consecutive step responses. Unidirectional means that the target position was only approached from one direction. A control program is written that enables the stage to continuously perform the same step into the X- and Y-direction separately and return back to the starting point. During this sequence of measurements the experimental setup will remain intact throughout all measurements. The corresponding displacements in X- and Y-direction will be measured using the laser triangulation sensors and the output is plotted in MATLAB. Figure 6.6 shows the results from this repeatability test for both the X- and Y-direction.

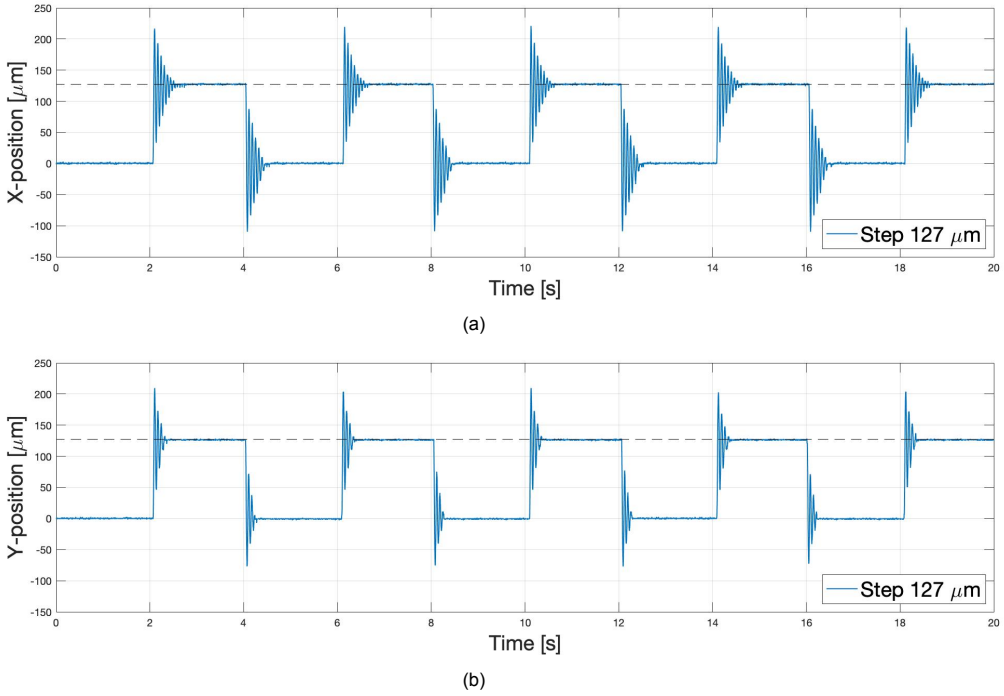

Figure 6.6: Multiple consecutive open loop step responses with the required step size of $127\mu m$ (dashed lines indicate desired position) were used for measuring the repeatability of the stage in: **(a)** X-direction ($3\sigma = \pm 2.5\mu m$). **(b)** Y-direction ($3\sigma = \pm 2.2\mu m$).

The error between the desired position and the measured position is used as input for the probability density functions as shown in Figure 6.7. The repeatability measurement in X-direction shows that the stage has a three-sigma repeatability of $\pm 2.5\mu m$, which means that 99.7% of all test data will fall within $\pm 3\sigma (= \pm 2.5\mu m)$ of the mean measured position in X-direction.

The results in Y-direction show that the stage has a three-sigma repeatability of $\pm 2.2\mu m$, which means that 99.7% of all test data will fall within $\pm 3\sigma (= \pm 2.2\mu m)$ of the mean measured position in Y-direction.

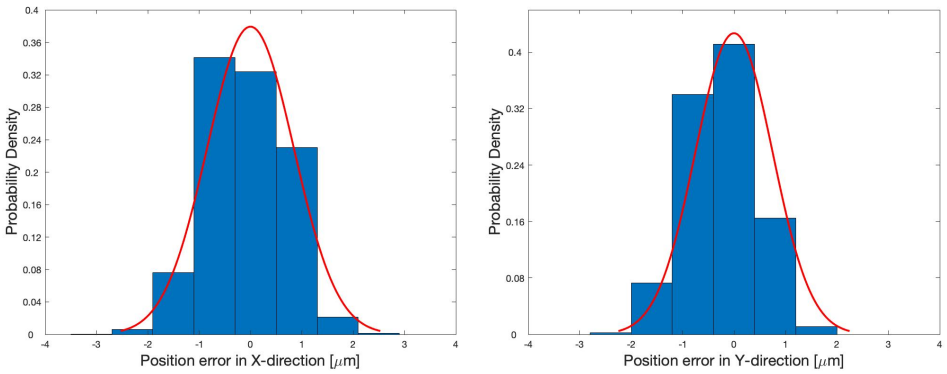

(a) (b)

Figure 6.7: **(a)** Probability density function of the positioning error in X-direction with a standard deviation of $\sigma = 0.83\mu m$ **(b)** Probability density function of the positioning error in Y-direction with a standard deviation of $\sigma = 0.73\mu m$

6.3. Linearity

The input voltage can be plotted against displacement of the motion stage to determine the linearity of the system. Only one axis is actuated at a time such that coupling errors are not present. This measurement is performed for a range of $\pm 5mm$ in both X- and Y-direction and the results are shown in Figure 6.8.

As expected, the displacement-voltage curve is of linear form. This is because the flexures are long enough such that only linear elastic deformation will take place. It is also observed that at the outer boundaries of the workspace, the relation starts to turn nonlinear but its effects are still negligible. This is a common phenomenon for large deflections and is caused by a decrease of the effective arm at which the input force acts which causes a smaller bending moment in the flexures. At the same time only part of the deflection caused by the moment contributes to the deflection in the drive direction. It can be expected that if the displacement goes beyond $\pm 5mm$, the relation will turn nonlinear due to an increased stiffness in the direction of actuation.

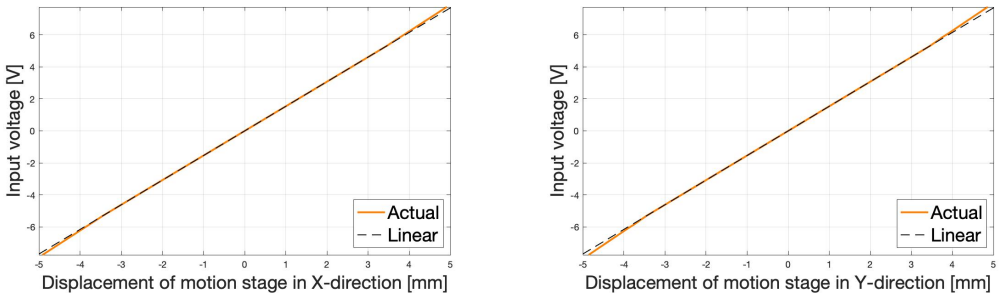

(a) (b)

Figure 6.8: The relation between input voltage and output (displacement) of the motion stage is shown for single actuation of the separate drive directions such that coupling errors are not present: **(a)** Actuation in X-direction with Y in neutral position. **(b)** Actuation in Y-direction with X in neutral position.

In order to assess the linearity of the step response, the test can be performed for different target locations throughout the workspace. This is done to compare the performance in the center of the workspace and the performance closer to the outer boundaries. Consecutive steps of $127\mu m$ are performed starting from the unactuated (neutral) position. The results for consecutive steps starting from neutral position until one millimeter are shown in Figure 6.9. This measurement was performed throughout the entire workspace and a consistent performance was observed.

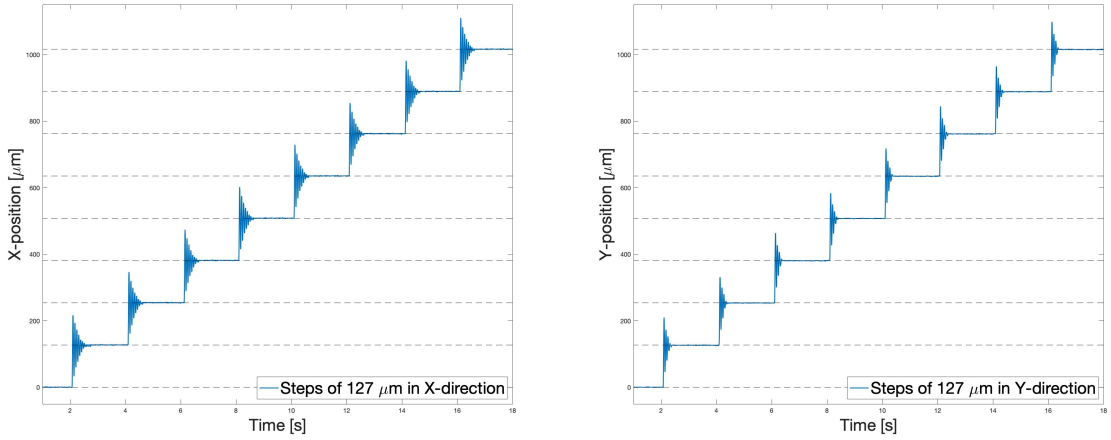

(a) (b)

Figure 6.9: Consecutive steps of the required $127\mu m$ step size, where the horizontal dashed lines indicate the desired position of each step. **(a)** X-direction **(b)** Y-direction

6.4. System identification

System identification is performed to learn more about the system's behavior using experimental data obtained from input and output relations. The input is a sine-wave chirp signal excitation along the X-direction between the frequency range of $1Hz - 20Hz$. One laser triangulation sensor is used to measure output which is the displacement in X-direction of the motion stage. This output is measured with a sampling frequency of $800Hz$ and the magnitude response, phase response and coherence plot are shown below in Figure 6.10. This frequency response measurement was performed with a neutral (unactuated) Y-position of the motion stage

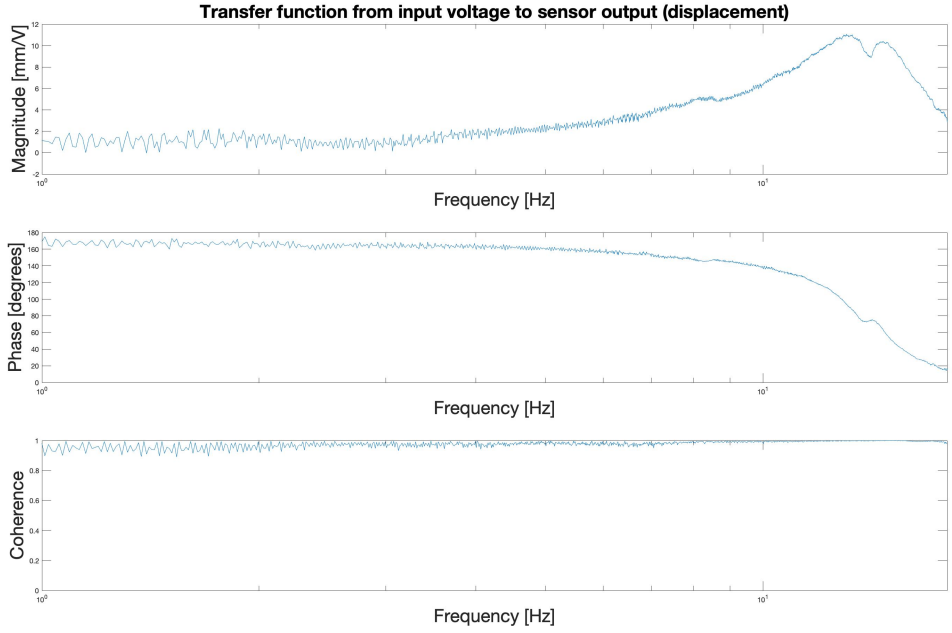

Figure 6.10: Frequency response function (FRF) and coherence of the system with identified data in X-direction with Y in neutral (unactuated) position.

The amplitude of the magnitude response is shown in mm/V. The frequency response shows that at low frequencies, the input and output are equal in magnitude, and in phase. This is shown by a magnitude of $1mm/V$ and a phase of approximately $180degrees$ on the plots of magnitude and phase respectively. As the frequency increases nearing the first resonance frequencies, the output becomes larger than the input. The natural frequencies of X-translation and Y-translation occur at $13Hz$ and $14Hz$ respectively. At $13Hz$, a pole is shown which results in a phase drop of $180degrees$. However, at $13.5Hz$ a zero is shown which prevents the phase from dropping $180degrees$ because it has to return up by another $180degrees$. Finally, after the Y-direction mode at $14Hz$, the phase goes down $180degrees$ and it should remain there until the next mode would appear. There is also looked at coherence, to see in which extent the measurements provide reliable data. The coherence almost equals one the entire frequency range meaning that the data is reliable.

The next mode shapes were previously predicted using simulations but are yet to be validated by the measurements. The frequency response in Figure 6.10 is only shown for frequencies until $20Hz$. However, to validate the predictions of mode shapes and behavior at higher bandwidths and to see the effects of cross-axis coupling, the measurement will also be performed for higher frequencies.

The measurement is also performed for two different Y-positions of the motion stage to evaluate the effect of stiffness parameter variation on the systems behavior. The Y-locations are $y = 0mm$ and $y = 5mm$ respectively. This time, the frequency range is increased to $80Hz$ to gain more insight into how sufficient the motion axes are decoupled and whether the coupling errors present are negligible. The results from the frequency response measurements until $80Hz$ are shown below in Figure 6.11. The blue plots show the frequency response in X-direction where the Y-position of the motion stage is in neutral (unactuated) position. The red plots show the frequency response in X-direction where the Y-position of the motion stage is constantly actuated at $Y = 5mm$.

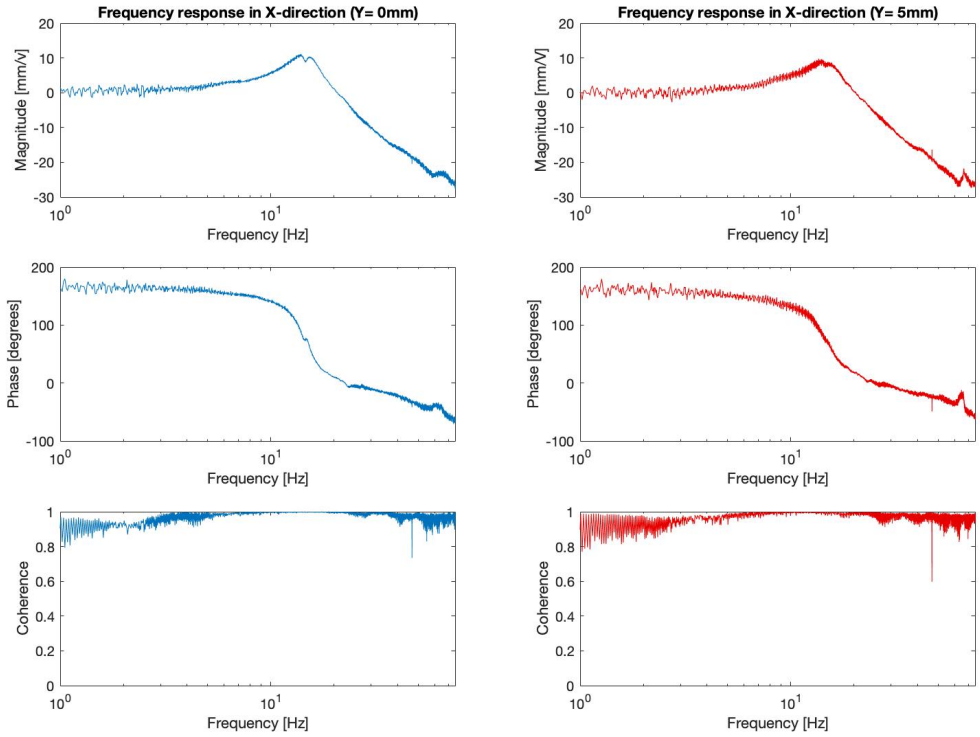

Figure 6.11: Frequency response function (FRF) and coherence of the system in X-direction with motion stage positioned at: neutral Y= $0mm$ (blue) and Y= $5mm$ (red).

Both frequency responses show similar behavior. Therefore, they are now plotted in one graph to see how large the coupling errors are and until which bandwidth they can be neglected. Figure 6.12 shows the frequency response function in X-direction with Y in neutral position (shown in blue) and with Y positioned at $Y = 5mm$ (shown in red).

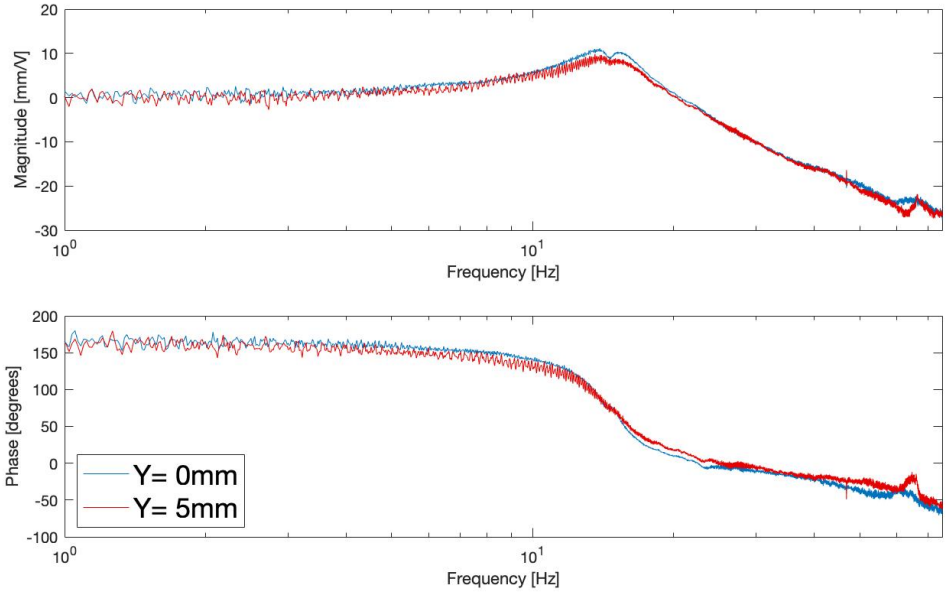

Figure 6.12: Comparison between frequency response in X-direction with $Y = 0mm$ (blue) and $Y = 5mm$ (red). This comparison confirms the decoupled design until a bandwidth of approximately $60Hz$.

The results from the comparison show how well the motion axes are decoupled and that the effects of coupling are negligible until a bandwidth of around $60Hz$. At higher frequencies, the coupling will result in different responses due to changes in support stiffness of the individual flexure modules of the mechanism. Also, at higher frequencies the output becomes very small and the phase has undergone a phase drop of $180degrees$ meaning that the input of the actuator and the displacement of the motion stage are out-of-phase. It should also be noted that at high frequencies ($\geq 40Hz$), the phase drops continuously due to low-pass filter behavior.

6.5. Out-of-plane deflection

The deflection in out-of-plane (Z) direction is measured using one laser triangulation sensor. This performance evaluation is crucial for a proper functioning auto-focus of the microscope. The Z-location of the unactuated motion stage is used as reference point and can therefore be used for relative displacement measurements. The motion stage is actuated to the outer boundaries of the workspace, along both the X- and Y-direction, where the out-of-plane deflection is expected to be the highest. For this measurement, only one axis is actuated at a time. The deflection is plotted against the linear translation in the drive direction such that the differences in out-of-plane deflections at different locations in the workspace can be observed. The measurements show that the error is not a systematic error. Instead, it appears to be a random error. Therefore, only the results from $0mm$ to $5mm$ in X-direction are shown in Figure 6.13.

The measured out-of-plane deflections turned out to be higher than evaluated during the COMSOL simulations. A reason for this is that in the simulations the weight of the reference point was not taken into account. The stage was not designed specifically to constrain deflections in out-of-plane direction since this would negatively affect the performance in X- and Y-directions.

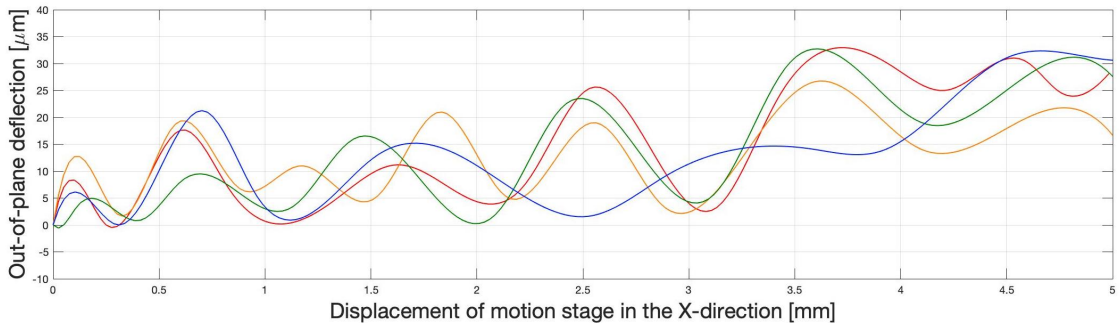

Figure 6.13: Out-of-plane deflection of the motion stage along the X-direction. Each color is a different measurement and all curves are obtained through interpolation between the measured data points.

Multiple measurements were performed and in all cases the out-of-plane deflection was observed to be within $\pm 20\mu m$ from the initial position. This means that after proper calibration of the autofocus, the scanning range to obtain a sharp image can be limited to $\pm 20\mu m$. The measurements show that the stage has a low out-of-plane stiffness since the weight of the overhang structure results in large deflections ($\pm 20\mu m$). The increased error with respect to the simulations, is caused by both the increased weight of the reference point that is attached to the motion stage and by bad initial alignment of this reference point.

7

Discussion

The results of the research are discussed with the initial requirements and design goals in mind. A demonstrator was designed successfully that can be used for automated malaria diagnosis. The stage can also be used for other applications and is not limited to just the blood smear analysis application. The experimental setup provides reliable results with high reproducibility.

Evaluation of the requirements. First an evaluation of the requirements, as stated in the conceptual stage design phase, is done to see whether all requirements are met.

- **Degrees of freedom:** The design has two degrees of freedom in the desired travel directions X and Y. All other degrees of freedom are either constrained or minimized. Hence, the requirement regarding the degrees of freedom is met.
- **Workspace:** A workspace of $10mm$ by $10mm$ is achieved which is sufficient for the application of blood smear analysis.
- **Repeatability:** A 3σ repeatability of $\pm 2.5\mu m$ and $\pm 2.2\mu m$ is obtained in the X- and Y-direction respectively. Therefore, the requirement regarding high repeatability ($3\sigma \leq 10\ \mu m$) is being met.
- **Settling time:** The settling times of a $127\mu m$ step in X- and Y-direction are $0.4s$ and $0.2s$ respectively. Therefore, the settling time requirement of $0.1s$ is not met but when the pre-filter that was designed is implemented it will be met. In this case the settling time can be reduced to $34ms$ which is almost three times as fast as required.
- **Out-of-plane deflection:** The out-of-plane deflections proved to be within $\pm 20\mu m$ such that the sample will stay within the autofocus range of the microscope. This performance is better than required but still leaves a lot of room for improvement. When the out-of-plane stiffness is increased, a smaller scanning range of the autofocus is required and this results in a faster scanning procedure.

Evaluation of the desired specifications and design goals. In the conceptual stage design phase a few desired specifications and design goals were formulated. They are listed below to see if they were implemented sufficiently:

- **Compactness:** The compliant stage design can be considered compact since the area ratio of workspace to planar dimension is relatively high when compared to existing compliant stages. Also, the stage is compact enough to be integrated into a microscope which was desired. Of course size reductions are possible but this would result in a shorter lifetime of the system due to higher stresses in the flexures.
- **Low-cost design:** The compliant stage itself can be 3D-printed for only $\approx 3.00\$$. Bulk cost estimations show that the entire system (including control hardware and excluding the cost of a laptop and microscope) has a price of approximately $300\$$. Since 99% of the costs are due

to the voice coil actuators, there is still a lot of room for improvement by switching to a cheaper alternative for actuation. The entire system (excluding laptop and microscope) is of low cost making it affordable for local doctor's practices in developing countries.

- **Robustness:** The demonstrator has an overall robust design except for the flexures itself of course. This means that the demonstrator is suitable for use outside of cleanroom environments.
- **Manufacturability:** The first design goal was that the demonstrator is built in-house (TU Delft). This was realized using a simple but effective manufacturing method which is 3D-printing. This allowed for quick iterations between design modifications and production.
- **Design for assembly:** The second design goal was to design for assembly. This principle was taken into account during the entire design phase. Therefore, the final demonstrator consists of minimal parts that can easily be assembled which reduces assembly costs.

Comparison to current methods of malaria diagnosis. The demonstrator that was designed can be integrated into a microscope and combined with a computer vision algorithm it can be used to detect malaria and quantitate parasite-infected red blood cells. The performance of the demonstrator can be compared to existing methods of malaria diagnosis based on the following criteria:

- **Scanning time:** The scanning procedure of the stage takes only 3.4 minutes, including time for the autofocus to stabilize and obtain a sharp image this results in a total scanning time of approximately 17 minutes. This is faster than manual diagnosis $(60min)$ and comes close to the speed of a hematology analyzer $(2min)$ at a fraction of the costs.
- **System costs:** A standard hematology analyzer costs around $10.000\$$, while this system has a total cost of approximately $300\$$ including control hardware and excluding the cost of a laptop and microscope since it is assumed that those are already available in the local doctor's practice. This makes the system almost thirty times cheaper than the hematology analyzer which makes it more affordable for a local doctor's practice in developing countries. These costs can even be reduced by finding an alternative actuator since almost all costs (99%) are due to the expensive voice coil motors.
- **Size of system:** The setup is much smaller than a hematology analyzer. This makes it more suitable for a local doctor's practice since it can be integrated into a normal microscope stage. Therefore, the space required for the setup corresponds with the space that is required for a microscope.

Comparison to previous compliant stage design research. The performance of the demonstrator was compared to previous research and the following improvements were observed:

- **Compactness ratio:** The compliant stage design can be considered compact since the area ratio of workspace to planar dimension is relatively high when compared to existing compliant stages.
- **Low-cost design:** Almost all stages found in literature were fabricated using wire EDM which is an expensive fabrication method compared to 3D-printing. To put things in perspective: if this compliant stage was fabricated using wire EDM then the costs would be around $600\$$ while 3D-printing of this stage can be done for $\approx 3.00\$$.
- **Decoupled motion:** Negligible cross-axis coupling was achieved until at least $60Hz$. This means that an actuation in X-direction has negligible effects on the Y-position of the motion stage. This enables fast and precise XY positioning.

Limitations of the design. The design itself and the experimental setup have some limitations which are listed below:

- **Temperature dependence:** All measurements were performed at room temperature. It is expected that the stage will behave different at higher or lower temperatures. The temperature should not exceed 40° since from this temperature the effects on performance are indelible and the design can not be used for further precision applications.
- **Effects of creep:** Materials that have a long-term exposure to high levels of stress that are still below the yield strength of the material can slowly deform permanently. This is referred to as creep and it is an undesired phenomenon since it will change the behaviour of the mechanism. The design was designed using a fatigue design curve which should prevent creep from occurring for at least 30.000 cycles while being actuated until maximum deformation.
- **Hysteresis:** A lag between input and output of the system upon a change in direction could take place which is referred to as hysteresis. The system is actuated using two voice coil motors which have the advantage of negligible hysteresis which makes them ideal for applications where bi-directional movement is required such as in the scanning procedure.

8

Conclusion

This research achieved to identify an effective strategy to design a compact planar compliant XY precision positioning stage that can be used for automated malaria diagnosis using a microscope. Compliant mechanisms show great potential for precision applications by offering vibration-free precision positioning. The frictionless and backlash-free characteristics of flexure joints guarantee high reproducibility and enable low-cost feedforward positioning control. However, achieving large motion range ($\gg 1mm$) along with high motion quality ($< 10\mu m$) has been a key challenge in designing compliant positioning stages. Therefore, the objective of this research was to design a long-stroke compliant XY stage capable of positioning precisely ($3\sigma < 10\mu m$) within a workspace of $10mm$ by $10mm$. The challenge imposed with this objective is that obtaining large deflections in flexure mechanisms can be hard to achieve due to the inherent imperfection of flexures and therefore the stage dimensions tend to become very large. Obtaining larger deflections in flexure mechanisms results in increased stresses that should not exceed the yield stress of the material to prevent permanent deformations. Larger deflections will also result in parasitic motion errors that are undesired since they decrease the positioning precision.

A strategy was implemented that makes use of a modular design topology consisting of flexural building blocks to overcome the above-mentioned challenges. First, three different flexural building blocks have been evaluated based on their performance while reaching a deflection of $\pm 5mm$ in the drive direction. An evaluation was done in terms of motion stress levels, parasitic rotation, and parasitic motion errors. Based on this evaluation, the double parallelogram flexure module was selected as the most suitable flexural building block for this application. The desired mechanism design had to be of planar structure which means that one mechanism is used for actuation in both X- and Y-direction. This introduced another challenge of achieving minimal cross-axis coupling. This challenge was overcome by implementing a constraint-based method to obtain a mechanism design with modular structure, devised out of several building blocks, that has a high degree of geometric decoupling between the two motion axes. Parametric design optimization was then performed in order to achieve the desired characteristics in terms of stress levels, motion range, yaw rotation, stiffness, out-of-plane deflection and resonant frequency.

A demonstrator of the proposed stage has been fabricated out of PLA using 3D-printing and shown to be simultaneously capable of large travel range and high quality motion. The stage was actuated using two voice coil actuators and can position precisely within a workspace of $10mm$ by $10mm$. The performance is very consistent throughout the workspace and shows translational motion with high repeatability ($3\sigma \leq 2.5\mu m$) due to the highly reproducible behavior of flexures and due to a lack of friction and backlash. The out-of-plane deflection of the motion stage proved to be within $\pm 20\mu m$ which is well within the range of the autofocus. System identification confirms that the demonstrator provides a reliable decoupled motion between the X- and Y-axes until a bandwidth of $60Hz$ meaning that the effects of cross-axis coupling are negligible, thus enabling fast and precise XY positioning.

The scientific contribution of this research lies in the design choices that were made which resulted in the compact design of a long-stroke compliant XY precision positioning stage with decoupled and modular structure. The design process can function as a guideline for others to design a compliant positioning stage. The performance evaluation with regard to this long-stroke compact design is compared to existing works by looking at an area ratio of workspace to planar dimension. It shows a higher ratio than almost all stages in literature. The area of the mechanism design can even be reduced if smaller flexure lengths are used which would result in a shorter lifetime of the stage due to higher stresses in the flexures. Also, the mechanism frame is redundant and only present to ensure robustness. Therefore, planar dimensions can be reduced which introduces a trade-off between the life of cycles and compact design. Implementations of the strategy used in this design process were proven effective since it resulted in the compact design of a long-stroke planar compliant XY precision positioning stage. A demonstrator of the stage was built and performance evaluation measurements validated that the stage can position precisely $(3\sigma \leq 2.5\mu m)$ within a workspace of $10mm$ by $10mm$. Therefore, we can conclude that the scientific research gap has been investigated successfully.

The societal contribution of this research is to speed up the diagnosis of malaria in developing countries. The scanning procedure of the stage takes only 3.4 minutes, including time for the autofocus to stabilize and obtain sharp images this results in a total scanning time of approximately 17 minutes. This is faster than manual diagnosis $(60min)$ and comes close to the speed of a hematology analyzer $(2min)$ at a fraction of the cost. This means that one blood smear analysis can be performed within 17 minutes, without the need of an experienced microscopist. Another advantage is that the sample does not have to be sent all over the country to be evaluated in a laboratory. This leads to earlier test results from the analysis and thus faster treatment of the patients. The compliant stage itself can be 3D-printed for only $\approx 3.00\$$. Bulk cost estimations show that the entire system has a price of approximately $300\$$. This includes the cost of control hardware and excludes the cost of a laptop and microscope since it is assumed that those are already available in the local doctor's practice. Almost all costs (99%) are due to the expensive voice coil motors which leaves room for future improvements. Since a standard hematology analyzer costs around $10.000\$$, this makes the system almost thirty times cheaper than the hematology analyzer which makes it more affordable for local doctor's practices in developing countries.

In conclusion, the results obtained from FEA and experimental measurements are shown to be in good agreement with the analytical predictions for this stage. The demonstrator managed to achieve the set requirements for blood smear analysis. Therefore, it can be concluded that the stage was designed successfully and it can be implemented for automated malaria diagnosis to help Africa control the disease.

9

Recommendations

Comparing the planar compliant XY precision positioning stage to existing stages from literature, improvements could be made to increase its performance. Therefore, some recommendations for future research or modifications are given on how to improve this positioning stage.

Recommendations considering the compliant stage design:

- A different material should be used to increase the performance of the motion stage. For example, aluminum can be used which offers better performance in a wider range of temperatures. Aluminum is less sensitive to heat changes compared to PLA. Another advantage is that the design can be made more compact due to the material properties. However, this change in material is most likely associated with increased costs. The current fabrication method is inexpensive compared to wire EDM which is commonly used for the processing of aluminum.
- To minimize deflections of the motion stage in out-of-plane direction, we must use parametric design optimisation to increase stiffness in the out-of-plane direction. With an increased stiffness in out-of-plane direction, the axial scanning range of the autofocus can be reduced resulting in a faster scanning procedure. Next to that, the stage would be suitable for more applications if the payload capacity is increased. This can be achieved by either increasing the thickness of the stage or by using symmetry to create extra support for the motion stage.
- The expensive voice coil actuators must be replaced by a cheaper alternative. Even though the actuators used in this project demonstrate high quality performance, they drive up the price of the entire stage. A recommendation would be to find an alternative linear actuator.

Recommendations considering control of the stage:

- To enable standalone use of this compact positioning stage for automated malaria diagnosis in developing countries, an Arduino Uno in combination with a dual H-Bridge should be used as control hardware. This is an inexpensive control unit which is very accessible for local doctor's practices.
- Position feedback must be integrated into the stage to enhance the performance. This does increase the total cost which is not desired for this application. However, if there are certain applications where a higher budget is available, this is a good way to increase the performance of the stage.
- The input shapers that were designed should be implemented if faster performance is desired. This form of feedforward control can improve the performance by decreasing the overshoot and reducing the settling time of a single step.

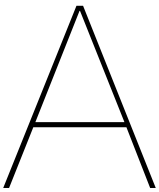

Literature study

Research into state-of-the-art precision positioning stages for light microscopy

Tim Feddes - 4450930

HTE student of Delft University of Technology - Delft

February 10, 2020

Contents

1 Introduction

Malaria remains a major burden on global health, with roughly 200 million cases worldwide and more than 400,000 deaths per year [1]. Fortunately, the disease is well curable if diagnosed early so treatment can start right away. There are three steps required for detecting malaria and its severity to guide the initial treatment decision [2]. To carry out these three steps it is necessary to have a proper functioning microscope and a highly experienced and skilled microscopist to carry out the procedure. Currently, these steps are performed manually. The downside to this is that each analysis takes up a lot of time which is unfavorable since the medication is most effective if treatment starts as early as possible. One manual analysis of a blood smear takes up to 30 minutes. There are simply not enough microscopes and trained microscopists to be able to diagnose all the patients. This results in long working days of up to twelve hours.

This shows the need for an automated microscopist to examine blood smears. The microscopic analysis can be automated by designing a precision positioning stage that scans the entire surface of the blood smear with high precision and high speed. Combined with a computer vision algorithm malaria can easily be detected without any manual work except for preparing the blood smear on a glass slide. When automated, more blood smears can be analyzed each day resulting in earlier started treatment and thus more effective treatment [3]. Currently, there are precision positioning stages available for microscopes that achieve the requirements but they are too expensive for use in third world countries.

The scope of this literature study is to do extensive research into state-of-the-art precision positioning systems in order to identify a challenging knowledge gap to be studied in the subsequent MSc-project. This report will be concluded with a proposal of the design of a compact precision positioning stage based on this knowledge gap, that can be used for microscopy in third world countries to detect malaria.

The following sections of the report are organized as follows: Section 2.1 gives a brief introduction about the different stage structures. Section 2.2 presents the most common bearings used for high precision positioning stages. Section 2.3 classifies four of the most-used actuators, including their working principles, advantages, and disadvantages. Section 2.4 gives an overview of the sensors that could be used for position feedback. Section 2.5 shows two microcontrollers for data processing and control. Section 3 discusses the results and proposes a challenging research topic. Section 4 concludes the report and shows how the project proposal will have a sufficient impact on society.

2 State-of-the-art

This section describes the state-of-the-art precision positioning systems. In literature it can be found that precision positioning stages can be divided into the following essential components: the stage structure, type of bearing, actuator, position sensor for feedback, and a controller. All of these components offer multiple variants that will be evaluated throughout this section. The evaluation of all variants includes an explanation of the working principle, current use as found in literature, current limits and applicability to the goal. The latter has different performance requirements for all individual essential components and its requirements are therefore described in the introduction paragraphs of the corresponding components.

2.1 Stage structure

When faced with multi-axis motion applications, there are two variations of stage structures. There is a stacked stage configuration, which is especially used when long travel and high precision are required both. The second type of stage structure is a planar motion stage. This structure is often used when nano-scale precision is required with a short travel range. Both structures will be evaluated further in this subsection to determine their applicability to the goal that will be based on their achievable travel range, size, and precision.

2.1.1 Stacked motion stage

In this case, there will be a coarse motion stage that can achieve long travel, and stacked on top there is a fine motion stage to obtain the required precision. An example of such a stacked stage is designed in [4], this structure enables the stage to reach an operating range of 200 mm x 200 mm. However, this stacked configuration will limit the performance of the system. First of all, the system will be increased in size due to the stacking of two stages which will also result in an unbalanced structure that lacks stability and introduces assembly errors. This leads to unwanted vibrations that were generated during a long-range scan resulting in lower accuracy of the system. Such a structure would perform well in an application where a long travel range is required and a not so high accuracy. Figure 1 shows a different type of stacked motion stage which uses one stage for motion in X-direction and on top a stage that controls motion in Y-direction.

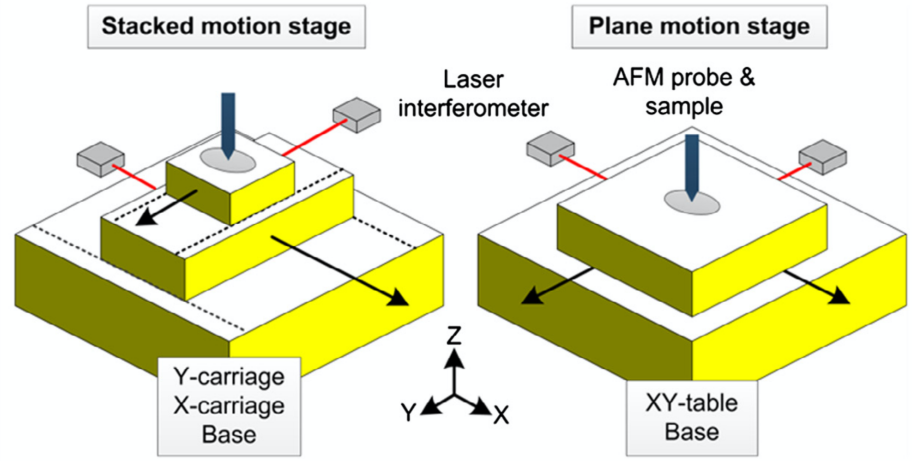

Figure 1: Difference between a stacked and planar motion stage [5].

A stacked motion stage structure can achieve a long travel range that is sufficient for the application of blood smear analysis using microscopy. Integrating the stage into the microscope will however introduce several size-related problems. The stacking of stages results in a larger setup with less rigidity that is associated with lower precision. If all of the above is taken into account it is decided to rule out the stacked motion stage structure for the proposed design.

2.1.2 Planar motion stage

A planar motion stage yields a more compact layout since its actuators are all mounted to the ground. The fixation of actuators results in higher bandwidth and greater precision since distur-

bances are minimized. This structure overcomes the drawbacks of the stacked stage previously mentioned. It will not be able to obtain the same travel range but due to its greater rigidity, it allows for more accurate motion and faster response [6]. These attributes are very beneficial for high-precision positioning systems and they are therefore widely used in the industry. Despite these benefits, planar motion stages often have over-constraint which arise from a geometric layout that exhibits coupling between two motion axes which restricts motion range. A solution for this is given in the form of systematic constraint-based methods that avoid geometric over-constraint [7][8]. Figure 1 shows an example of what a planar motion stage could look like.

A planar motion stage structure can also achieve the travel range that is required for blood smear analysis. However, this may result in restricted motion due to over-constraint. If the constraint-based methods [7][8] are used this problem can be avoided. This planar structure yields a more compact layout and can therefore easily be integrated into a microscope. Due to its high rigidity disturbances are minimized. Thus, it can offer a higher precision than the stacked motion stage. It is decided that the planar motion stage structure is very applicable to the proposed design.

2.2 Bearing types

Friction is bound to occur between the motion stage and the structural frame. To reduce this friction some kind of bearing is required between these two components. There is a variety of bearing types available and each comes with its pros and cons. The most common bearings used in positioning systems will be described in this subsection. To ensure their operational reliability, desired life, and applicability to the goal, the bearings will be evaluated based on their: ability to achieve long travel range, repeatability, friction, and the need for lubrication.

2.2.1 Linear ball bearing

A linear ball bearing is designed to allow motion in one direction. There are a lot of precision positioning stages that use linear ball bearings such as [9]. This stage has a resolution of 1 micron and can achieve a very long stroke. However, the presence of friction results in wear, lower accuracy and lower repeatability. There are a lot of other linear bearings but they were not taken into consideration because they have relative high friction compared to the other bearing types mentioned in this section.

Figure 2: Linear bearing on a rails that has a travel range of several meters [10].

This type of bearing can achieve the required travel range for blood smear analysis but the presence of friction results in lower repeatability and the need for lubrication. This type of bearing as shown in figure 2 is often used in applications where a travel range of several meters is required and it does not have significant potential for high precision applications such as microscopy.

2.2.2 Hydrostatic bearing

Hydrostatic bearings are especially used in high-precision applications due to their extreme precision. They have low stick-slip behaviour which results in almost wear-free usage. The principle behind them is that an external pressure supply is used to inject a lubricant into the space between the bearing surfaces. This means that there is a thin lubricant film present between the two surfaces which prevents friction and thus allows very precise position control in the sub-micrometre range. Different principles can be used such as:

- *Air bearing levitation:* Air bearings use a thin film of pressurized air to support a load. This thin film of air allows for relative motion between the structural frame and the motion stage. Air bearings have the advantage of lacking backlash and no static friction. Since air bearings are wear-free, they will not release any particles into the environment which makes them ideal for cleanroom applications. H.P. Vuong [11] used air bearing levitation to design a contactless wafer stage shown in figure 3. This design can achieve a bandwidth of 60 Hz with a positioning error of 50 nm. Performance limitations include the mass of the actuators, external vibrations, pressure noise, and sensor noise. Air bearing levitation will not function properly in unclean environments as dust or dirt will affect the performance drastically.

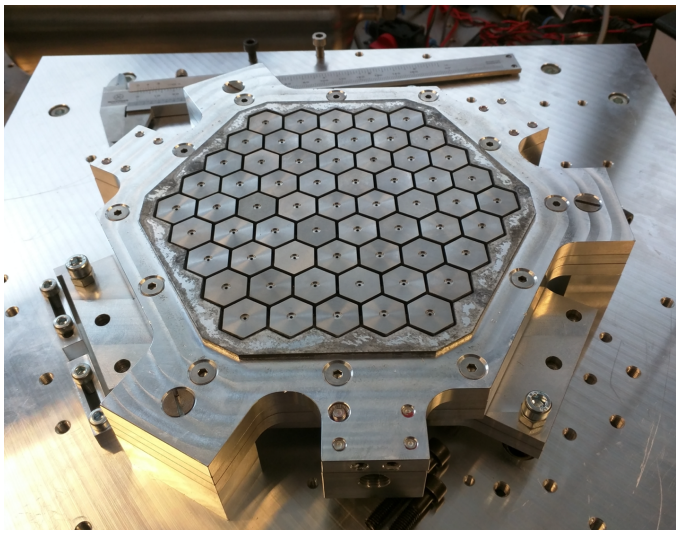

Figure 3: Contactless wafer stage that was designed by H.P.Vuong [11].

- *Ferrofluid bearings:* A ferrofluid is a type of fluid with magnetic properties. Its most important property is that it is attracted by a magnet which is due to the nanometer-sized ferromagnetic particles that are suspended in the fluid [12]. Ferrofluids can be used as a bearing that is able to carry a load by using an air pocket enclosed by a ferrofluid seal. The advantage of this type of bearing is that it has low friction and no stick-slip behavior. M. Café used ferrofluid bearings

in his design for a nanometer precision 6-DOF planar motion stage [13]. The precision of this stage was not limited by the ferrofluid bearings, instead it was limited by the resolution of the interferometers. Even though ferrofluid bearings have a lot of potential for high precision positioning stages, they also have drawbacks such as side leakage during a translational motion [14]. This leakage occurs due to the ferrofluid sticking to the surface on which the bearing moves. The bearing decreases in height since some ferrofluid is left behind.

- *Magnetic bearing:* A magnetic bearing is a type of bearing that supports a load using magnetic levitation. The magnetic force is used to counteract the effect of gravity to maintain a relative position between the motion stage and the structural frame. In literature, several examples were found that use Halbach linear active magnetic bearings. Figure 4 shows the cross-section of a symmetric Halbach array and its magnetic flux lines that result from finite element analysis. From this analysis, it can be derived that leakage from the top and side surfaces is very small since the flux is concentrated under the magnet array on the bottom surface.

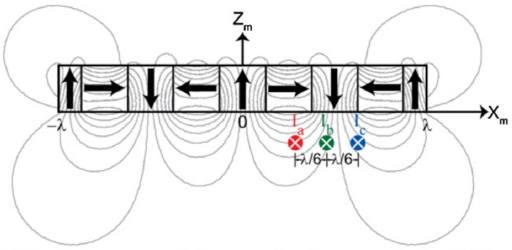

Figure 4: A symmetric Halbach array with its magnetic flux lines [15].

Magnetic levitation was used to actuate a fine stage that is carried by a coarse stage that uses linear guides and linear motors [16]. This stage is suitable for ultra-high precision stages since it has a resolution of 10 nm with a position error of only 4 nm. Another stage design uses magnetic levitation to achieve a travel range of 25 mm x 25 mm with a positioning accuracy of 10 nm [17]. The positioning noise is dominated by system disturbances and its accuracy could be improved by increasing the system bandwidth which should result in improved disturbance rejection.

All of the hydrostatic bearings mentioned above can achieve the required travel range for blood smear analysis. They have high repeatability and no friction due to the thin lubricant film that is present between the two surfaces. They are all very applicable to the goal but since a lot of research has been done into them recently there is no knowledge gap considering they already have a compact layout and can achieve long travel range.

2.2.3 Flexure bearing

Frictionless bearing technology is essential for vibration-free precision positioning with a nano-scale resolution, repeatability, and accuracy. In order to achieve frictionless motion, one can use a flexure bearing. A flexure bearing is a bearing that allows motion by bending a load element as shown in figure 5. The mechanism transforms motion and force with the elastic deformation of the compliant component and has the advantages of no mechanical friction, no clearance, no backlash, and higher sensitivity, etc [18]. Hence it is suitable to use such a bearing in precision positioning fields. The downside to this type of bearing is that it has a short operating range. This problem can be reduced by designing a platform with motion magnification as done in [19]. Even after magnification, the

operating range is only 283 µm x 285 µm which is not sufficient for long travel applications.

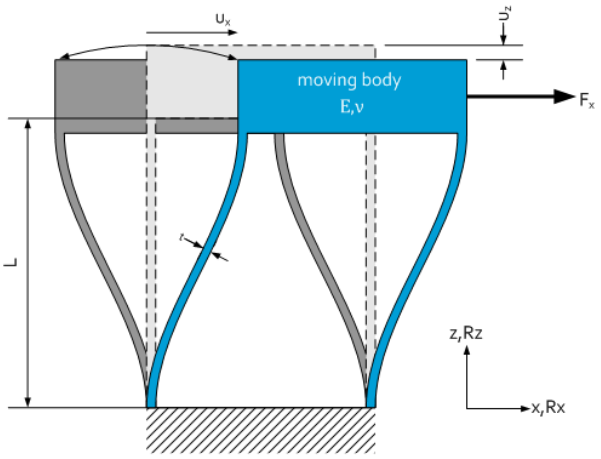

Figure 5: Bending of a flexure bearing that allows motion of the moving body [20].

A flexure bearing has high repeatability, frictionless motion, and it does not need any lubrication. It would be very applicable to the goal if it were able to achieve a long travel range. Designing a compliant motion stage with a long travel range remains a challenge that is yet to be solved.

2.3 Actuation

To move and control the motion stage to its desired position, an actuator is needed. This actuator will convert a control signal into mechanical action. Actuators can provide linear or rotational movement depending on what is needed for the application. There are multiple types of actuators available, each having their advantages and disadvantages. The following actuators are commonly used in precision positioning stages and their applicability to the goal will be evaluated based on resolution, accuracy, travel range, speed, and the presence of hysteresis.

2.3.1 Electromagnetic actuator

A voice coil motor is commonly used in precision positioning systems. This type of motor consists of two separate parts, a magnetic housing and a coil as shown in figure 6a. When a voltage is applied across the terminals of the motor, it will cause the motor to move in a direction that can be reversed by changing the polarity of the applied voltage. The generated force is proportional to the current that flows through the coil. The structural stability of voice coil motors is suitable for high precision positioning systems. The advantages of voice-coil motors include simple design and construction, high resolution and accelerations, and small in size [21][22]. Current limits of performance are caused by hysteresis nonlinearities that result in poor performance if neglected during long travel ranges.

The voice coil motor provides high resolution and accelerations while it can achieve the required travel range for blood smear analysis. However, it is important to characterize the output/input properties of the voice coil motor to account for hysteresis nonlinearities that will otherwise result in poor performance. This actuator is found to be very applicable to the goal and will be considered in the proposed design.

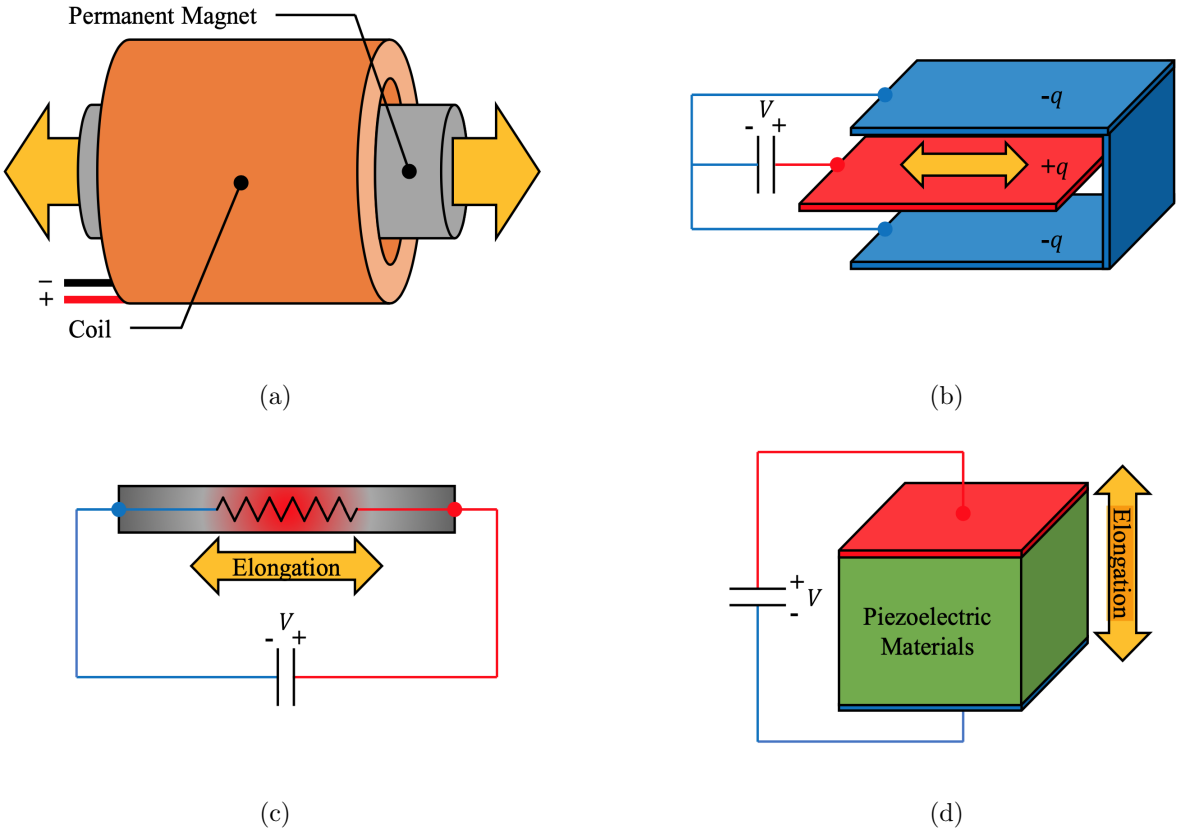

Figure 6: Working principles of: (**a**) electromagnetic actuator; (**b**) electrostatic actuator; (**c**) electrothermal actuator; (**d**) piezoelectric actuator.[23]

2.3.2 Electrostatic actuator

An electrostatic actuator operates on the principle of electric charge. It consists of a capacitor with two electrodes of which one is fixed. When a voltage is applied, the free electrode will move to change its capacitance in order to counteract the voltage change. The direction of actuation is dependent on how the free electrode is constrained by the guiding mechanism. It can be used as a linear drive but is also frequently used as a rotary drive by curving the plate. Its advantages include high dynamic performance and hysteresis-free behavior [23]. One of the main disadvantages of electrostatic actuators is that there are large voltages necessary and that the generated force is only in the nano/micro-newton scale [24]. Figure 6b shows a simplified comb-drive actuator that can be used for linear actuation.

This actuator may have hysteresis-free behavior and high dynamic performance, but it will not be able to provide enough force to actuate the motion stage to reach the desired travel range for blood smear analysis and it is therefore not applicable for the goal.

2.3.3 Electrothermal actuator

The electrothermal actuator is a micromanipulator that generates motion by thermal expansion amplification. The working principle is shown in figure 6c. A voltage is applied to the electrical terminals of the device. The potential difference induces currents to flow throughout the device

which results in Joule heating. This Joule heating causes the actuator to deform and this deformation can be used for actuation. Electrothermal actuators are easily fabricated with a monolithic structure. They can also generate a larger force while being more compact than an electrostatic actuator. Other advantages include high accuracy and good repeatability [25]. However, it also has some drawbacks such as low frequency, high power consumption, and nonlinear movement which is hard to control [26].

This actuator has high accuracy and good repeatability but will be increasingly difficult to control since it has nonlinear movement. It will also not be able to provide a fast actuation of the stage which is preferable for the goal. Next to that, it has an extravagant high power consumption. It is therefore not taken into consideration for the proposed design.

2.3.4 Piezoelectric actuator

A piezoelectric material can convert electrical energy into a mechanical displacement or vice versa, this is called the reverse piezoelectric effect. An illustration of how this process works is shown in figure 6d. They are widely used in high precision positioning applications due to their major advantages of large blocking force, high stiffness, compact size, and because it can control a nanometer-scale displacement with fast response [27]. The main drawback of a piezoelectric actuator is that the stroke is very limited since it will only obtain a displacement which is 0.01 percent of the actuator length [28]. This displacement can be amplified by adopting a lever mechanism connected to the decoupler. However, this amplification may result in relatively low transverse stiffness at its end-effector and therefore cannot guarantee a linear output motion. Another way to increase the operating range of the system is by stacking the actuator on a coarse platform that is driven by another actuator, this method most likely results in a bulky system with lower performance.

The piezoelectric actuator is widely used in the industry for high precision applications with nano- or micro-motion range. This is because of its high resolution, accuracy, and speed. However, it will be a very tough challenge to increase the travel range to the required range for blood smear analysis while maintaining a compact design. This actuator is therefore not a good fit for the goal and will not be considered in the proposed design.

2.4 Sensor

Position sensors are used to determine the linear or angular position of the stage. In order to choose a suitable sensor for a specific application, one must determine whether linear or rotary position feedback is required. The required measuring range, resolution and repeatability are very important when selecting the sensor. Sensors are often very expensive, therefore the cost will also be considered while deciding if a sensor is applicable to the goal.

2.4.1 Laser interferometer

Laser interferometer position measurement systems provide very precise position or distance information for dimensional measurements or motion control. The measurement method uses the interference of waves. One laser beam is split in two as shown in figure 7, which gives an interference pattern when the waves coincide. Small differences in traveled distance of the optical paths can be measured from this interference pattern [29]. Wang and Zhang [19] used one laser interferometer to accurately measure the variation in preload displacement of a moving plate. This resulted in an accuracy of less than 5 nm. Max Café [13] used three laser interferometers to provide position

information about the planar DOF: x, y and θ_z with a precision of 5nm. Laser interferometers are widely used in industry because they can achieve an extremely high resolution of nanometer-scale [29]. They are very expensive and therefore not accessible to startups or third world countries.

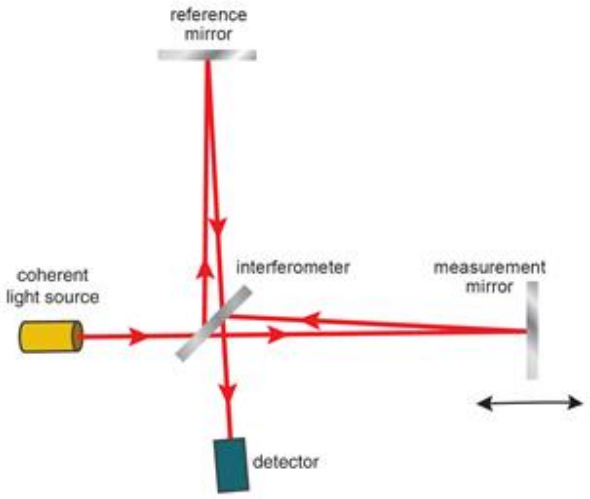

Figure 7: Working principle of a laser interferometer [29].

The laser interferometer can reach the required measuring range, resolution, and repeatability to perform a very accurate blood smear analysis. However, it is very expensive and therefore not taken into consideration for the proposed design since it would not be accessible to the target audience.

2.4.2 Linear encoder

A linear encoder is a sensor, transducer or reading-head linked to a scale that encodes position. The sensor reads the scale and converts position into an analog or digital signal which can be decoded into a digital output showing the position. Many different physical properties are exploited in order to encode the position. There are magnetic, optical, capacitive, inductive and eddy current linear encoders. Optical linear encoders have the highest resolution and are therefore widely used feedback sensors for precision stages [30][31], but they are sensitive to contamination from dust or vibration. This type of encoder is used in the design of a large range XY nanopositioning system to measure the distance between the ground and a moving stage in one degree of freedom [32]. The resolution of the linear encoder is limited by its line grating period and electronic interpolation. Its digital output makes it immune to electronic noise [32].

An optical linear encoder is not very expensive and is suitable as a position feedback sensor in the proposed design. It should be noted that this type of sensor is sensitive to dust or dirt and is preferably used in clean environments only, but this goes for almost every sensor concept.

2.4.3 Optical image recognition

Optical image recognition sensors can be used for multiple degrees of freedom measurements. They compare consecutive images taken by a camera to determine a difference in position. In literature, multiple examples can be found where optical image recognition is used for position feedback. For example, an optical mouse sensor that measures the displacement between two consecutive images from which the position can be obtained by integrating the displacement over the time interval between the images [33]. This design was able to achieve a precision of 10 microns. Another example found in literature uses a smart camera as a position sensor [34]. Combined with an image processing algorithm this setup achieved a precision of 0.5 mm which is not precise enough for most precision positioning stages.

The optical mouse sensor design of G. Mok [33] is a cheap and yet high performing sensor for position feedback. Therefore, it could be integrated into the proposed design and will be taken into consideration.

2.4.4 Position-sensitive device

A position-sensitive device is a photodetector that detects the position of a light spot that is incident on a surface. The light spot is created by a laser beam that hits the photodetector. There are uniaxial photodetectors that can measure position along a single axis and duo-lateral or tetra-lateral which can measure position along two axes. Position sensitive devices are commonly used in high precision positioning systems because of their high accuracy and speed [35]. One position sensitive device was used to obtain a 3-DOF measurement: x, y, and θ_z [36]. Instead of measuring the position of one light beam as described above, this design projects three light beams on the position sensitive device in successive order, so that only one light beam is incident at a time. A sensing algorithm was developed to convert the three sensor signals into a 3-DOF position measurement.

A position-sensitive device has very high accuracy and speed. It is widely available but more expensive than the other sensors mentioned here except for the laser interferometer. Even though it is more expensive it will still be considered for the proposed design.

2.4.5 Capacitive displacement sensor

A capacitive displacement sensor operates by measuring changes in electrical capacitance. The variation in distance between the sensor and the measurement object leads to a change in capacity. If an alternating current of constant frequency and constant amplitude flows through the sensor capacitor, the amplitude of the alternating voltage on the sensor is proportional to the distance to the measurement object [37]. The displacement is detected and converted into an output showing the measured position. Capacitive displacement sensors are often used in vacuum and clean room applications where they achieve sub-nanometer resolutions [38]. They can also be used in dusty environments because some dust or dirt between the sensor and the measurement object is acceptable as the sensors operate at such high resolutions that the effects of dust particles are negligible. A drawback of the capacitive displacement sensor is that its performance is heavily influenced by changes in environmental conditions such as temperature or humidity.

A capacitive-displacement sensor is commonly used for position feedback in high precision positioning stages. It is a reliable sensor that can be used in dusty environments. It is not very expensive and still accessible to the target audience. However, due to it being sensitive to environmental

conditions such as temperature or humidity it was decided to not use this sensor in the proposed design.

2.4.6 Sensorless concept

A sensorless concept would determine the position of the stage based on the field of view of the microscope. The microscope can scan the entire surface of a blood smear by following a trajectory that is generated based on the field of view and therefore does not need position feedback. Based on the field of view the stage can be shifted sideways till a new image is established. Another traditional approach to sensorless position control can be done by compensating the actuators for expected hysteresis errors [39]. This method offers limited performance since compensation is not always accurate.

This method of sensorless position control would be very applicable to the goal. It will reduce the price significantly and if applied correctly will show no limited performance for blood smear analysis.

2.5 Controller

A microcontroller is a compact integrated circuit designed for data processing and control. A typical controller includes a processor, memory, and input/output ports integrated into a single chip. There are a lot of different microcontrollers available which will not all be discussed in this section. The ones that are discussed in this section are chosen because of their popularity. Both are open source projects, with very accessible software and hardware that is flexible to be customized. Another advantage is that they are less expensive than other microcontrollers. Their appicability to the goal will be determined based on their simplicity and price.

2.5.1 Arduino

An Arduino is a microcontroller motherboard without an operating system that can be programmed to accept electrical inputs and control electrical outputs. One of its main advantages is that programs can be loaded directly into the device without the need for a hardware programmer to burn the program. It can only run one program at a time and is therefore mostly used for simple repetitive tasks that have to be repeated over and over again. It is considered to be easy to use and has an enormous community for troubleshooting. Another advantage of the Arduino is that it has a large amount of input/output pins which are required to control all the individual components of a stage. Overall, its simplicity makes it a good option for pure hardware projects.

Arduino is an inexpensive tool for developing interactive objects. Its simplicity is unmatched since it can easily be programmed to take inputs from sensors and control actuators without years of programming experience. Therefore, it is very applicable to the goal and will be taken into consideration for the proposed design.

2.5.2 Raspberry Pi

A Raspberry Pi differentiates itself from an Arduino by having an operating system. It has the ability to run multiple programs and can perform more complicated tasks than Arduino. The Raspberry Pi is 40 times faster than an Arduino when it comes to clock speed [40]. This might sound like it is superior to the Arduino, but that is only the case when it comes to complicated software applications. A disadvantage of the Raspberry Pi is that it only has a few input/output

pins and is not built specifically for controlling outputs and inputs. Next to that, it is more expensive than the Arduino. Thus it should only be considered in cases where the Arduino does not have enough power and memory to run a specific program.

Raspberry Pi is slightly more expensive than Arduino. It was not specifically built for controlling outputs and inputs which will be harder to do. Its applicability to the goal is lower than Arduino, thus it will not be used in the proposed design.

3 Discussion

From the literature review, we can find that the performance of a precision positioning stage is commonly evaluated by its accuracy, resolution, repeatability, and travel range. A stage can be subdivided into the following essential components: stage structure, bearing mechanism, actuator, position sensor, and controller. All of these components offer multiple variants that have been evaluated in this literature review. A concise summary of the results will be given in this section.

The most applicable stage structure for blood smear analysis was found to be a planar motion stage which is evaluated in section 2.1. This was decided because of its compact design and high rigidity. The stacked motion stage would also be applicable but it will result in a bigger setup. This structure would have been better if for the application an alternative degree of freedom was needed such as vertical motion.

When looking at the different types of bearings that are available (section 2.2), it was found that the bearing mechanism with the most potential for automated blood smear analysis using light microscopy in third world countries is a flexure bearing due to its promising features such as no mechanical friction, no clearance, no backlash, and higher sensitivity. It is also a low-cost option, can be made monolithically and is not susceptible to unclean environments. Compliant stages are mainly used for nano-precision applications with short operating ranges. This method is not used yet for microscopy due to its short operating range (sub-micrometer). Other bearings such as hydrostatic bearings also have high applicability for the goal but were not chosen because a lot of research has been done into them recently and no knowledge gaps were established during the evaluation.

Four different actuators that are commonly used in high precision applications were evaluated in section 2.3. This evaluation did not result in any profound knowledge gaps but did reveal that a voice coil motor is the most applicable actuator. It provides high resolution and fast accelerations. It should be taken into account that hysteresis nonlinearities cannot be neglected since this negatively affects performance during long travel ranges. The electrostatic, electrothermal, and piezoelectric actuators were considered to have lower applicability because of restricted motion range, slow actuation, and not maintaining a compact design while increasing the travel range respectively.

Multiple sensor concepts were described in section 2.4. Their applicability to the goal was mainly determined by sensor costs. The evaluation indicated that the most applicable sensor to the goal is the position-sensitive device due to its high accuracy and speed. Another option that will be considered is a sensorless design that determines position based on the field of view of the microscope. If this option shows to be viable it would significantly reduce the cost of the entire system.

Only two controllers were evaluated in section 2.5 which are both applicable to the research objective. Arduino appeared to be the better option out of the two because of its control simplicity. Even though Raspberry Pi is only slightly more expensive than Arduino and can complete more

complicated tasks, it turned out to be less applicable for the research objective due to its few input/output pins and because it is not specifically built to control those outputs and inputs.

When all the components mentioned above are combined into a low-cost precision positioning stage that can be used for automatic scanning in blood smear analysis, the stage can be used in third world countries to help thousands of patients. The current method of manual blood smear analysis is not time effective and therefore the solution mentioned in this report would be a significant improvement. More blood smear analyses can be done every day which results in an earlier start of treatment. Early treatment results in the healing of more patients. For the scientific community, this solution would also be of great relevance since there is a research gap in compliant stages with long travel. Current compliant stages can only achieve travel ranges of up to several hundred microns.

4 Conclusion

The results show that there is a knowledge gap in the area of compact long travel compliant precision positioning stages. If a flexure based compliant precision positioning stage could be designed that includes both compact size and the ability to reach long travel range, this would be a thorough improvement for not only the automation of blood smear analysis but also for the scientific community in general. Compliant stages are mainly used for nano-precision applications with small operating ranges. This method is not used yet for microscopy due to its short operating range (submicrometer). Therefore, a proposal is made to design a compact long travel compliant precision positioning stage that can obtain an operating range of a square centimeter which is sufficient for blood smear analysis. This emerges as a promising yet challenging research topic.

References

[1] M. Poostchi, K. Silamut, and G. Thoma. Image analysis and machine learning for detecting malaria. *Translational Research*, 194:36–55, 2018.

[2] Division of Parasitic Diseases Global Health and Malaria. Malaria diagnostic tests, 2018.

[3] E. Pillay, S. Khodaiji, B. Bezuidenhout, M. Litshie, and T. Coetzer. Evaluation of automated malaria diagnosis using the sysmex xn-30 analyser in a clinical setting. *Malaria Journal*, 18(1), 2019.

[4] J. Kim, C. Kang, and T. Eom. Metrological atomic force microscope using a large range scanning dual stage. *International Journal of Precision Engineering and Manufacturing volume*, 10:11–17, 2009.

[5] M. Torralba, M. Valenzuela, J. Albajez, and J. Aguilar. Large range nanopositioning stage design: A three-layer and two-stage platform. *Measurement*, 89:55–71, 2016.

[6] Daniel C. Handley, Tien-Fu Lu, Yuen Kuan Yong, and Chris W. J. Zhang. A simple and efficient dynamic modelling method for compliant micropositioning mechanisms using flexure hinges. *The International Society for Optical Engineering*, 2004.

[7] S. Awtar. Synthesis and analysis of parallel kinematic xy flexure mechanisms. Master's thesis, Massachusetts Institute of Technology, 2004.

[8] S. Awtar and A. Slocum. Topology evolution of high performance xy flexure stages. pages 1–4, 2005.

[9] IntelliDrives. Xy positioning table, Accessed: October 2019.

[10] TecnoTools. Sc20uu 20mm linear ball bearing linear motion bearing slide bushing for cnc, Accessed: November 2020.

[11] P. Vuong. *Contactless Handling of Thin Substrates using Air Bearing Technology*. PhD thesis, Technical University of Delft, 2016.

[12] Stefan G.E. Lampaert, Ron A.J. van Ostayen, and Jo W. Spronck. Precision applications of ferrofluid bearings. *Mikroniek*, (2):15, 2018.

[13] M. Café. Nanometer precision six degrees of freedom planar motion stage with ferrofluid bearings. Master's thesis, Technical University of Delft, 2014.

[14] T. Osman, G. Nada, and Z. Safar. Static and dynamic characteristics of magnetized journal bearings lubricated with ferrofluid. *Tribology Letters*, 15(2):97–105, 2001.

[15] X. Lu and I. Usman. 6d direct-drive technology for planar motion stages. *CIRP Annals*, 61(1):359–362, 2012.

[16] Y. Choi and D. Gweon. A high-precision dual-servo stage using halbach linear active magnetic bearings. *ASME Transactions on Mechatronics*, 16(5):925–931, 2011.

[17] M. Holmes, R. Hocken, and D. Trumper. The long-range scanning stage: a novel platform for scanned-probe microscopy. *Precision Engineering*, 24(3):191–209, 1999.

[18] Y. Huang, H. Wu, H. Liu, and Z. Yin. Intelligent robotics and applications. *10th International Conference*, Part III, 2017.

[19] R. Wang and X. Zhang. A planar 3-dof nanopositioning platform with large magnification. *Precision Engineering*, pages 1–11, 2016.

[20] JPE. Flexure guiding – 2 leaf springs in parallel, 2019.

[21] Mark Wilson. What is a voice coil actuator?, 2018.

[22] G. Shan, Y. Li, Y. Zhang, Z. Wang, and J. Qian. Experimental characterization, modeling and compensation of rate-independent hysteresis of voice coil motors. *Sensors and Actuators*, 251:10–19, 2016.

[23] Z. Wu and Q. Xu. Survey on recent designs of compliant micro-/nano-positioning stages. *Actuators*, 7(1):5, 2018.

[24] M. Verotti, A. Dochshanov, and N. Belfiore. A comprehensive survey on microgrippers design: Mechanical structure. *J. Mech. Des.*, 139(6), 2017.

[25] C. Nakic, J. Bieker, D. Lammle, T. Winterstein, H. Schlaak, G. Schaumann, and T. Abel. Development of an electrothermal micro positioning platform for laser targets with two degrees of freedom. *2016 International Conference on Manipulation, Automation and Robotics at Small Scales (MARSS)*, 2016.

[26] Y. Fu, J. Luo, A. Flewitt, and W. Milne. Smart microgrippers for biomems applications. *Biomaterials*, pages 291–336, 2012.

[27] L. Yangmin and X. Qingsong. Design and analysis of a totally decoupled flexure-based xy parallel micromanipulator. *IEEE Transactions on Robotics*, 25(3):645–657, 2009.

[28] Kee-Bong Choi, Jaejong Lee, and Seiichi Hata. A piezo-driven compliant stage with double mechanical amplification mechanisms arranged in parallel. page 67, 2010.

[29] Renishaw. Interferometry explained, Accessed: October 2019.

[30] H. Kunzmann, T. Pfeifer, and J. Flugge. Scales vs laser interferometers, performance and comparison of two measuring systems. *CIRP Annals*, 42(2):753–767, 1993.

[31] A. Teimel. Technology and applications of grating interferometers in high-precision measurement. *Precision Engineering*, 14(3):147–154, 1992.

[32] Shorya Awtar and Gaurav Parmar. Design of a large range xy nanopositioning system. *Journal of Mechanisms and Robotics*, 5(2).

[33] G. Mok. The design of a cost effective planar precision stage using optical mouse sensors. Master's thesis, Technical University of Delft, 2015.

[34] O. Pribula, M. Janosek, and J. Fischer. Optical position sensor based on digital image processing: Magnetic field mapping improvement. *Radioengineering*, 20(1):56–58, 2011.

[35] H. Andersson. *Position Sensitive Detectors - Device Technology and Applications in Spectroscopy.* PhD thesis, Mid Sweden University, 2008.

[36] S.H. Habib. Design of a three degrees of freedom planar precision stage using a single position sensitive detector. Master's thesis, Technical University of Delft, 2015.

[37] Chris Jones. Factors to consider when selecting capacitive displacement sensors, 2018.

[38] Micro-Epsilon Messtechnik. Capacitive sensors for displacement, distance and position, Accessed: November 2019.

[39] Mohammed Nouroz Islam and Rudolf Seethaler. Sensorless position control for piezoelectric actuators using a hybrid position observer. *ASME Transactions on Mechatronics PP*, 99:1–9, 2014.

[40] Lauren Orsini. Arduino vs. raspberry pi: Which is the right diy platform for you?, 2014.

B

Voice coil specifications

REVISIONS					
ZONE	LETTER	DESCRIPTION	DATE	CHECKED	APPROVED

SHOWN AT MID-STROKE

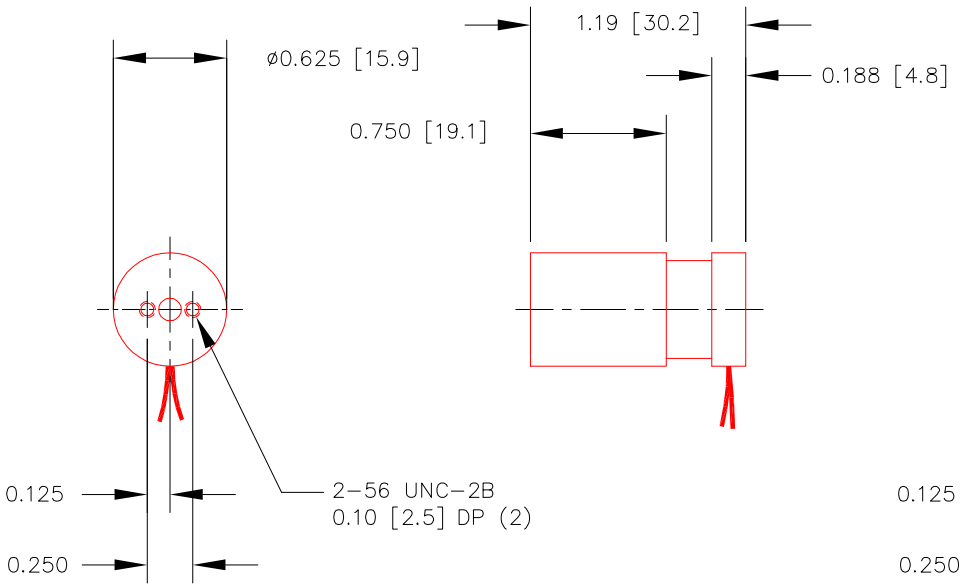

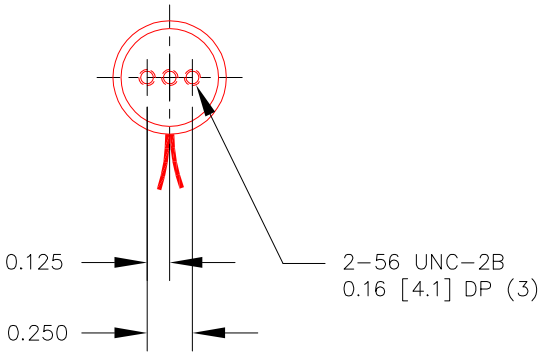

INTERMITTENT FORCE @10% DUTY CYCLE	5.4 N	19.3 OZ
CONTINUOUS FORCE	1.7 N	6.1 OZ
FORCE CONSTANT	1.7 N/A	6.3 OZ/A
BACK EMF CONSTANT	1.7 V/M/S	0.04 V/IN/S
STROKE	12.7 mm	0.50 IN
COIL CLEARANCE PER SIDE	0.32 mm	0.013 IN
COIL ASSY MASS	9 GR	0.32 OZ
BODY MASS	17 GR	0.60 OZ
COIL RESISTANCE	4.6 Ohms	
COIL INDUCTANCE @ 1000 Hz	0.8 mH	
MAX CONTINUOUS POWER	4.4 W	

ALL VALUES AT 25°C

NOTES :

UNLESS OTHERWISE SPECIFIED

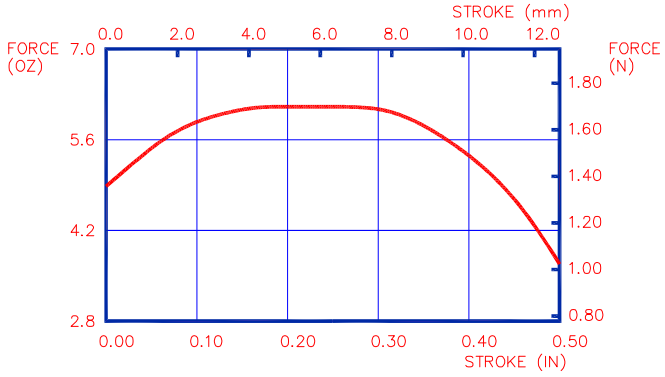

CONTINUOUS FORCE

DIMENSIONS ARE IN INCHES (mm)
TOLERANCES ON :
DECIMALS .XXX ± .005 .XX ± .01
FRACTIONS ± 1/125
ANGLES ± 1/2°
UNLESS OTHERWISE SPECIFIED

USED ON | NEXT ASSY

APPLICATION

MATERIAL

FINISH

CONTRACT

DRN		
CHKD		
APPVD		
APPVD		

MOTICONT

LINEAR VOICE COIL MOTOR

SIZE	CODE	DWG. NO.	REV.
A		LVCM-016-019-01	1

SCALE : 1 / 1 SHEET 1 OF 1

C

Sensor specifications

SENSORS & SYSTEMS

MICRO-EPSILON

INSTRUCTION MANUAL

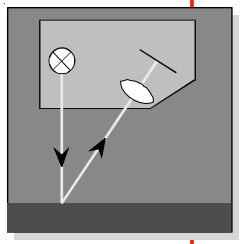

Betriebsanleitung
Instruction Manual

optoNCDT1300

3. Functional Principle, Technical Data

3.1 Short Description

The sensor uses the principle of optical triangulation, i.e. a visible, modulated point of light is projected onto the target surface.

Depending on the distance the diffuse fraction of the reflection of this point of light is then focussed onto a position sensitive element (CCD-array) by the receiving lens, which is arranged at a certain angle with respect to the optical axis of the laser beam.

The controller calculates the measured value from the CCD-array. A internal closed-loop control enables the sensor to measure against different surfaces.

A LED on the sensor indicates:
- In range
- Out of Range (upper and lower range values), poor target (unfit or no object)
- Mid range

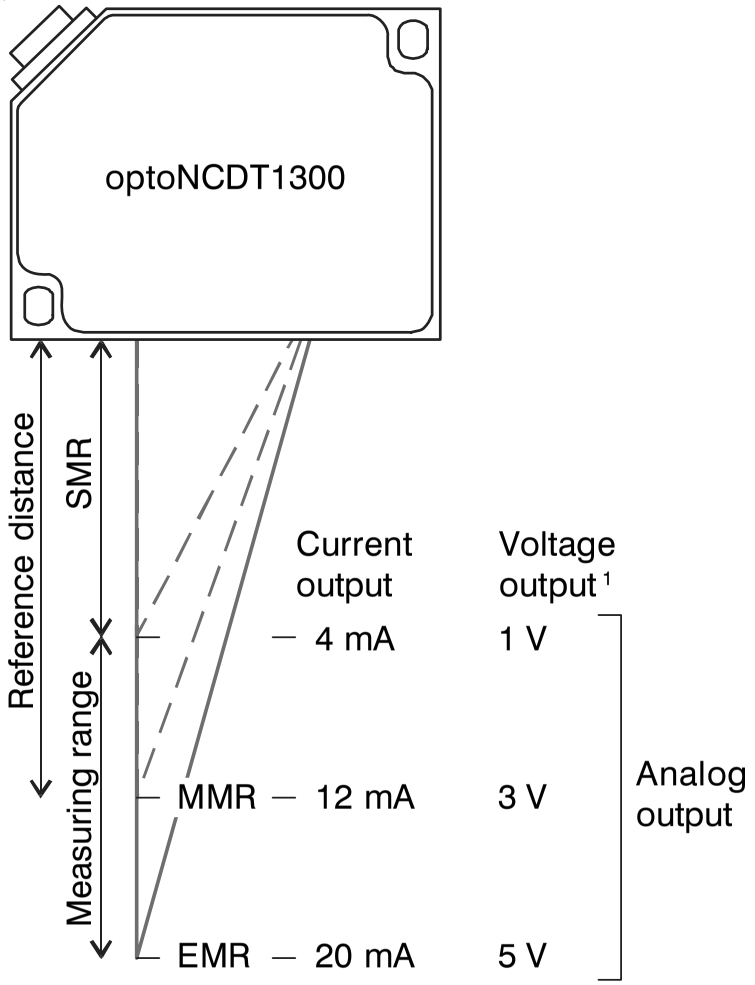

SMR = Start of measuring range
MMR = Mid range
EMR = End of measuring range

1) With PC1401-x/U output cable only

Fig. 3.1: Triangulation principle

English

3.2 Technical Data

Type	ILD1300-	20	50	100	200
Measuring principle		laser optical, triangulation			
Measuring range	mm (")	20 (.79)	50 (2.0)	100 (3.9)	200 (7.9)
Start of measuring range	mm (")	30 (1.2)	45 (1.8)	50 (2.0)	60 (2.4)
Reference distance MMR	mm (")	40 (1.6)	70 (2.8)	100 (3.9)	160 (6.3)
End of measuring range	mm (")	50 (2.0)	95 (3.7)	150 (5.9)	260 (10)
Linearity	µm (mils)	40 (1.57)	100 (3.94)	200 (7.87)	400 (15.7)
	% FSO	≤±0.2			
Resolution	static, µm (mils)	4 (.16)	10 (.39)	50 (2.0)	100 (3.9)
	dynamic, µm (mils)	10 (.39)	25 (.98)	100 (3.9)	200 (7.9)
Spot diameter	midrange, µm (mils)	335 (13)	110 (4)	130 (5)	2200 (87)
Sampling rate		500 Hz			
Light source		Semiconductor laser 1 mW, 670 nm (red)			
Laser class		2 (DIN EN 60825-1 03.97 / IEC 825-1 11.2001)			
Protection class		IP 67			

FSO = Full Scale Output
SMR = Start of measuring range
MMR = Midrange
EMR = End of measuring range

5. Installation

The ILD1300 is an optical sensor for measurements with micrometer accuracy. Make sure it is handled carefully when installing and operating.

5.1 Mounting of the Sensor

The sensor is mounted by means of 2 screws type M4.

The laser beam must be directed perpendicularly onto the surface of the target. Misalignment will create measuring errors (indication of bigger distances).

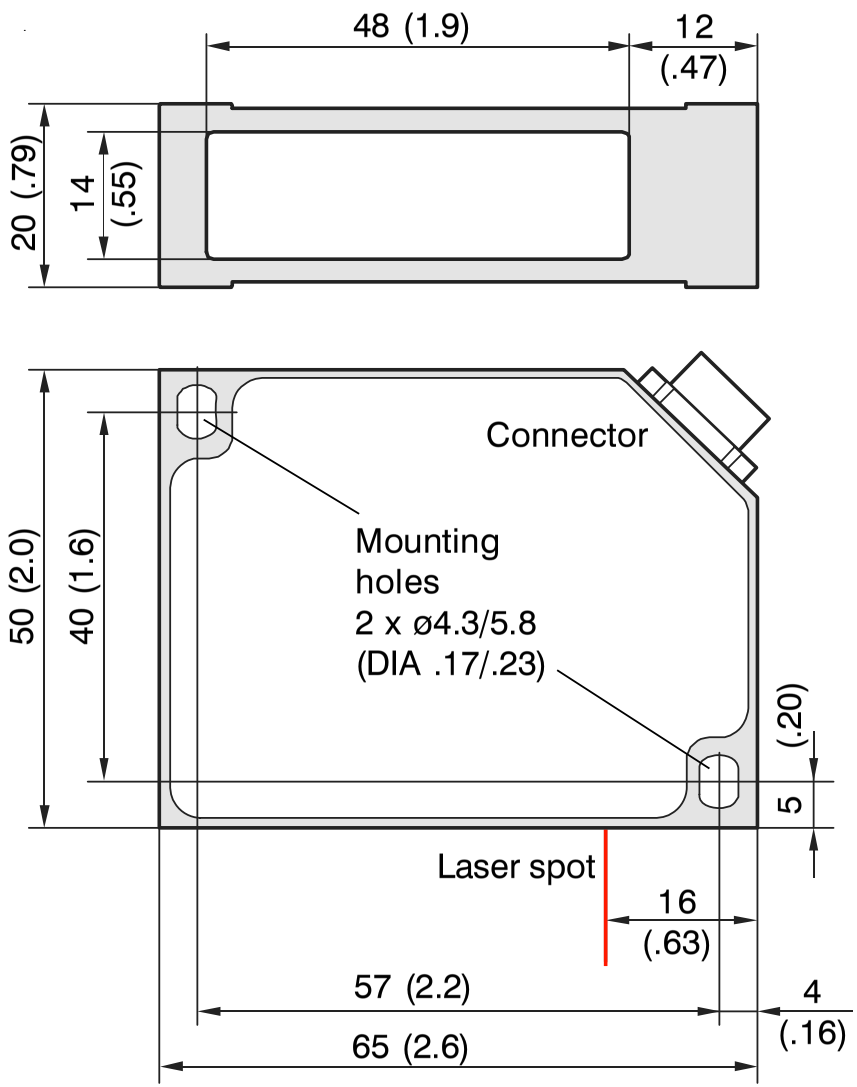

Fig. 5.1: Drawings ILD1300, not to scale

IMPORTANT!
Handle optical sensors with care.

Legend:
mm
(inches)

English

Bibliography

[1] Shorya Awtar and Gaurav Parmar. Design of a large range xy nanopositioning system. *Journal of Mechanisms and Robotics*, 5(2), 2013.

[2] Gadhave N. Bankar, S. Modeling and design analysis of xy flexure stage mechanism. 6(04): 899–900, April-2017.

[3] O. H. Ezeh and L. Susmel. On the fatigue strength of 3d-printed polylactide (pla). page 29, 2018.

[4] Centers for Disease Control and Prevention. Where malaria occurs, 2020. URL `https://www.cdc.gov/malaria/about/distribution.html`.

[5] L. Howell, S. Magleby, and B. Olsen. Handbook of compliant mechanisms. page 20, 2013.

[6] Applied Scientific Instrumentation. Auto-focus, 2019. URL `http://www.asiimaging.com/downloads/manuals/Auto-Focus-2-Subdocument.pdf`.

[7] Kim K. Shim J. Gweon D. Jeong J. Kang, D. Optimal design of high precisionxy-scanner with nanometer-level resolutionand millimeter-level working range. *Mechatronics 19 (2009) 562–570*.

[8] LabPulse. Beckman coulter debuts new tabletop hematology analyzer, 2020. URL `https://www.labpulse.com/index.aspx?sec=sup&sub=laba&pag=dis&ItemID=801235`.

[9] Waytashek M. Letcher, T. Material property testing of 3d-printed specimen in pla on an entry-level 3d-printer. *ASME International Mechanical Engineering Congress and Exposition (IMECE2014)*, 2014.

[10] Yangmin Li and Qingsong Xu. Design and analysis of a totally decoupled flexure-based xy parallel micromanipulator. *IEEE transactions on robotics*, 25(3):645–657, 2009.

[11] Yu J. Li, Z. A novel large-range xy compliant parallel micromanipulator. 25(4):Pages 14–19, 2003.

[12] Zhiqing Liu, Zhen Zhang, and Yan Peng. A self-adjusting stiffness center design for large stroke compliant xy nanomanipulators. *Mechanical Sciences*, 9(1):41, 2018.

[13] A. Mital. Design for assembly. *Manufacturing Process Selection Handbook*, 2013.

[14] Moticont. Linear voice coil motors with internal bearing, 2020. URL `http://moticont.com/linear-motor-with-bearing.htm`.

[15] Moticont. Linear voice coil motors, 2020. URL `http://moticont.com/voice-coil-motor.htm`.

[16] World Health Organization. Microscopy for the detection, identification and quantification of malaria parasites on stained thick and thin blood films in research settings. page 13.

[17] Deshmukh S. Reddy Y. Mate K. Patil, R. Fea analysis and experimental investigation of building blocks for flexural mechanism. 2015.

[18] Teledyne Photometrics. Maximizing microscope field of view, 2020. URL `https://www.photometrics.com/learn/white-papers/maximizing-microscope-field-of-view`.

[19] Silamut K. Thoma G. Poostchi, M. Image analysis and machine learning for detecting malaria. *Translational Research*, 194:36–55, 2018.

[20] Ke-qi Qi, Ya-lin Ding, Yang Xiang, Chao Fang, and Yang Zhang. A novel 2-dof compound compliant parallel guiding mechanism. *Mechanism and Machine Theory*, 117:21–34, 2017.

[21] S. Saunders. Researchers investigate tensile properties of 3d printed pla specimens, 2019. URL https://3dprint.com/233916/tensile-properties-of-3d-printed-pla/.

[22] Jiangkun Shang, Yanling Tian, Zheng Li, Fujun Wang, and Kunhai Cai. A novel voice coil motor-driven compliant micropositioning stage based on flexure mechanism. *Review of Scientific Instruments*, 86(9):095001, 2015.

[23] E. Uthman. Infectious mononucleosis. peripheral blood, wright stain, 2018. URL https://www.flickr.com/photos/euthman/25116997017/in/photostream/.

[24] Microscope World. Wright's stain for microscopy, 2015. URL http://blog.microscopeworld.com/2015/12/.

[25] Q. Xu. Design and development of a compact flexure-based xy precision positioning system with centimeter range. *IEEE TRANSACTIONS ON INDUSTRIAL ELECTRONICS,*, 61(2):894, 2014.